РОССИЙСКИЙ ГОСУДАРСТВЕННЫЙ ПЕДАГОГИЧЕСКИЙ УНИВЕРСИТЕТ им. А. И. ГЕРЦЕНА
HERZEN STATE PEDAGOGICAL UNIVERSITY of RUSSIA

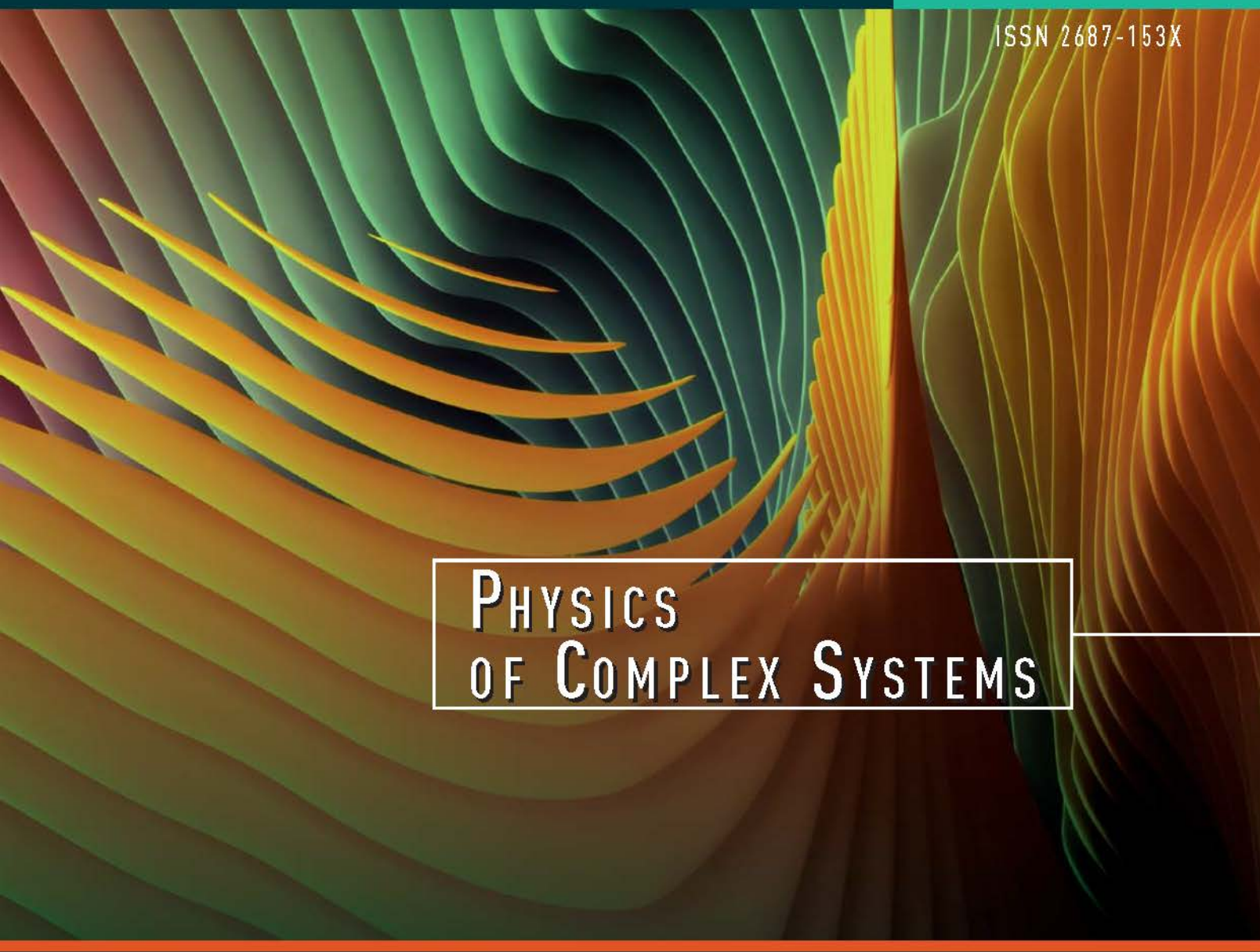

ISSN 2687-153X

Physics of Complex Systems

Т. 5 № 2 2024

Vol. 5 No. 2 2024

Herzen State Pedagogical University of Russia

ISSN 2687-153X (online)
physcomsys.ru
https://www.doi.org/10.33910/2687-153X-2024-5-2
2024. Vol. 5, no. 2

PHYSICS OF COMPLEX SYSTEMS

Mass Media Registration Certificate El No. FS77-77889, issued by Roskomnadzor on 10 February 2020
Peer-reviewed journal
Open Access
Published since 2020
4 issues per year

Publishing house of Herzen State Pedagogical University of Russia
48 Moika Emb., Saint Petersburg 191186, Russia
E-mail: izdat@herzen.spb.ru
Phone: +7 (812) 312-17-41

Data size 5,90 Mbyte
Published at 24.06.2024

Editor of the English text *K. Yu. Rybachuk*
Corrector *N. A. Sinenikolskaya*
Cover design by *O. V. Rudneva*
Layout by *D. V. Romanova*

Saint Petersburg, 2024

CONTENTS

Condensed Matter Physics.
Physics of thin films.
Surfaces and interfaces

UDC 54.057

EDN AEKJUI
https://www.doi.org/10.33910/2687-153X-2024-5-2-49-59

Molecular structure and dynamics of a water–ethanol solution of sodium dodecyl sulfate

I. V. Lunev ✉[1], A. A. Galiullin [1], Yu. F. Zuev [2]

[1] Kazan Federal University, 18 Kremlyovskaya Str, Kazan 420008, Russia
[2] Kazan Institute of Biochemistry and Biophysics, FRC Kazan Scientific Center of RAS, 2/31 Lobachevsky Str., Kazan 420111, Russia

Authors

Ivan V. Lunev, ORCID: 0000-0001-6201-4393, e-mail: lounev75@mail.ru

Artur A. Galiullin, ORCID: 0000-0002-4872-1486, e-mail: www.ag95@mail.ru

Yuriy F. Zuev, ORCID: 0000-0002-6715-2530, e-mail: yufzuev@mail.ru

For citation: Lunev, I. V., Galiullin, A. A., Zuev, Yu. F. (2024) Molecular structure and dynamics of a water–ethanol solution of sodium dodecyl sulfate. *Physics of Complex Systems*, 5 (2), 49–59. https://www.doi.org/10.33910/2687-153X-2024-5-2-49-59 EDN AEKJUI

Received 12 April 2024; reviewed 26 April 2024; accepted 26 April 2024.

Funding: The work was partially carried out as part of the state assignment of the FRC Kazan Scientific Center of RAS (Yu. F. Zuev — general analysis of the results). Dielectric measurements were carried out with support from the Strategic Academic Leadership Program of the Kazan (Volga Region) Federal University (Priority 2030).

Abstract. The processes of dielectric relaxation of sodium dodecyl sulfate (SDS) solutions were studied in a range of concentrations in a binary water–ethanol solvent at various alcohol concentrations. It was shown that ethanol at concentrations below 40% does not interfere with the formation of SDS micelles, and at a higher ethanol content, surfactant micelles do not form. However, NMR data show the presence of small associates, most likely SDS dimers, the properties and mobility of which depend on the composition of the water–ethanol medium, in solutions with high alcohol concentrations. Transformations in the structure and size of the complexes observed upon changing the ethanol content in the solution are discussed.

Keywords: binary water–ethanol solutions, surfactant, SDS, structure formation, solvation, micelles

Introduction

Ethanol is present in biological systems as a product of various chemical and biochemical reactions in living systems. The same applies to a variety of amphiphilic compounds, for example, lipids and fatty acids, the spontaneous association of which is an integral step in various biochemical processes. From the point of view of fundamental and applied research, it is necessary to represent the dynamic behavior and self-association features of various chemical compounds not only in aqueous, but also in water–ethanol solutions, which can be considered as a local environment for the functioning of biomacromolecules with different polarities and microstructures. In addition, we should not forget about the use of ethanol in technological schemes, where it is used with various functional implications. Given the development of renewable energy and the increasingly widespread use of ethanol as a biofuel, interest in regulating the properties of ethanol mixtures through various structuring additives is growing. This, in particular, explains the continuous interest in water–ethanol compositions as a medium in which various organic compounds acquire new properties.

It is known that the molecular structure of binary water–ethanol mixtures does not correspond to ideal solutions. This is indicated by nonlinear variations in the physicochemical properties of water–alcohol mixtures depending on the ethanol ratio (Beddard et al. 1981; Brai, Kaatze 1992; Dutt, Doraiswamy 1992; Soper et al. 2006; Wakisaka et al. 2001). Based on data from various methods, it has been shown that microscopic phase layering of the solvent occurs in such systems (Asenbaum et al. 2012; Mashimo et al. 1991; Mijaković et al. 2011; Nishikawa, Iijima 1993; Sato, Buchner 2004). Binary water–ethanol mixtures are prone to microlayering, leading to different types of structural states of the solvent, depending on the water/ethanol ratio. For example, it was suggested (Halder, Jana 2018) that as the ethanol concentration increases, the structure of the binary solvent changes, which at low alcohol concentrations is cyclic and at high alcohol concentrations is a chain structure of hydrogen-bonded molecular associates. It was found (Hu et al. 2010a; 2010b) that the ethanol/water binary solvent consists of four components: water associates, ethanol associates, and two types of water–ethanol complexes of different composition and structure.

Due to a continuous thermodynamic process of formation and destruction of hydrogen bonds in the volume of such liquids, the properties of ethanol/water systems are determined by the relative average contribution of at least four components with different types of ordering, the predominant composition of which changes as the composition of the binary medium changes. Such microheterogeneity affects both the solvation (Faizullin et al. 2017; Konnova et al. 2013) of solute molecules and the association processes of dissolved molecules. Therefore, in the solutions of organic substances in binary media, competition between hydrophilic and hydrophobic groups of each of the three components (water, alcohol and solute) depends on the ratio between them and affects the formation of supramolecular structures in such a solution.

The study of the structural-dynamic behavior of relatively simple amphiphilic surfactant molecules in aqueous ethanol media allows us to deepen our understanding of the behavior of more complex systems, for example, macromolecules of biological nature in living systems (Gubaidullin et al. 2016). Using the example of one of the most common surfactants, sodium dodecyl sulfate (SDS), this work examines the features of structure formation in SDS/ethanol/water systems.

Sodium dodecyl sulfate is a convenient model sample that makes possible a thorough study of the surfactant micelle formation process (Zueva et al. 2022). It has been studied in detail by NMR and conductometry methods, with the CMC and Krafft point values known for it (Gnezdilov et al. 2011; Zuev et al. 2007; Zueva et al. 2020). Some works (Buchner et al. 2005; Zuev et al. 2024) have obtained the values of dielectric parameters for aqueous SDS solutions. The properties of SDS in binary water–ethanol solvents have also been studied by NMR (Zueva et al. 2021). An analysis of reference literature shows that SDS solutions in binary solvents have been mainly studied by NMR methods and much less frequently using dielectric spectroscopy.

Below the critical micelle concentration (CMC), SDS molecules are predominantly in the molecular form, which is characterized by the highest self-diffusion coefficient D. As the surfactant concentration increases to CMC, the solution begins to form SDS micelles with an aggregation number N and a shape close to spherical (Zuev et al. 2007; Zueva et al. 2021). Based on the CMC of SDS, we selected surfactant concentrations of 3, 8, 20, 50 and 100 mmol×L^{-1}, which enabled us to quickly assess structural and dynamic changes in the surfactant solution during transition from a molecular to a micellar solution.

It is known (Wakisaka, Ohki 2005; Wakisaka et al. 2001; Zueva et al. 2021) that water–ethanol mixtures have three characteristic concentration ranges of 0–10%, 25–40% and 60–92.3%, which share the existence of the binary water–ethanol solvent in different energetic and structural states. These states differ in the microheterogeneous structure of the solvent and in the geometry of the hydrogen bond network. This can affect the process of surfactant micelle formation and the structure of its associates. For this reason, corresponding ethanol concentrations in our samples were chosen as 0, 10, 40 and 80 vol.%.

The purpose of this work is to study the dynamic structure of water–ethanol SDS solutions using dielectric spectroscopy.

Materials and methods

Materials

We used sodium dodecyl sulfate (SDS, L-4509, Sigma-Aldrich) with the main component accounting for at least 98.5% without additional purification. To prepare water–ethanol solutions, we used distilled water, additionally purified using the Milli Q system, and ethyl alcohol (95%, Medkhimprom OJSC, Russian

 https://www.doi.org/10.33910/2687-153X-2024-5-2-49-59

Federation). Samples were prepared with an SDS content of 3, 8, 20, 50 and 100 mmol×L^{-1} at ethanol concentrations of 0, 10, 40 and 80 vol.%.

Dielectric spectroscopy

All measurements of the dielectric spectra of aqueous alcohol solutions containing surfactants were carried out using a PNA-X Network Analyzer N5247A (Agilent Technologies, USA) (Fig. 1). The experiment was carried out in the temperature range of +20 to +50 °C in increments of 3 °C. Temperature was regulated using a LOIP LT 900 thermostat, into which test tubes with the solution were immersed. The accuracy of maintained temperature was ±0.1 °C.

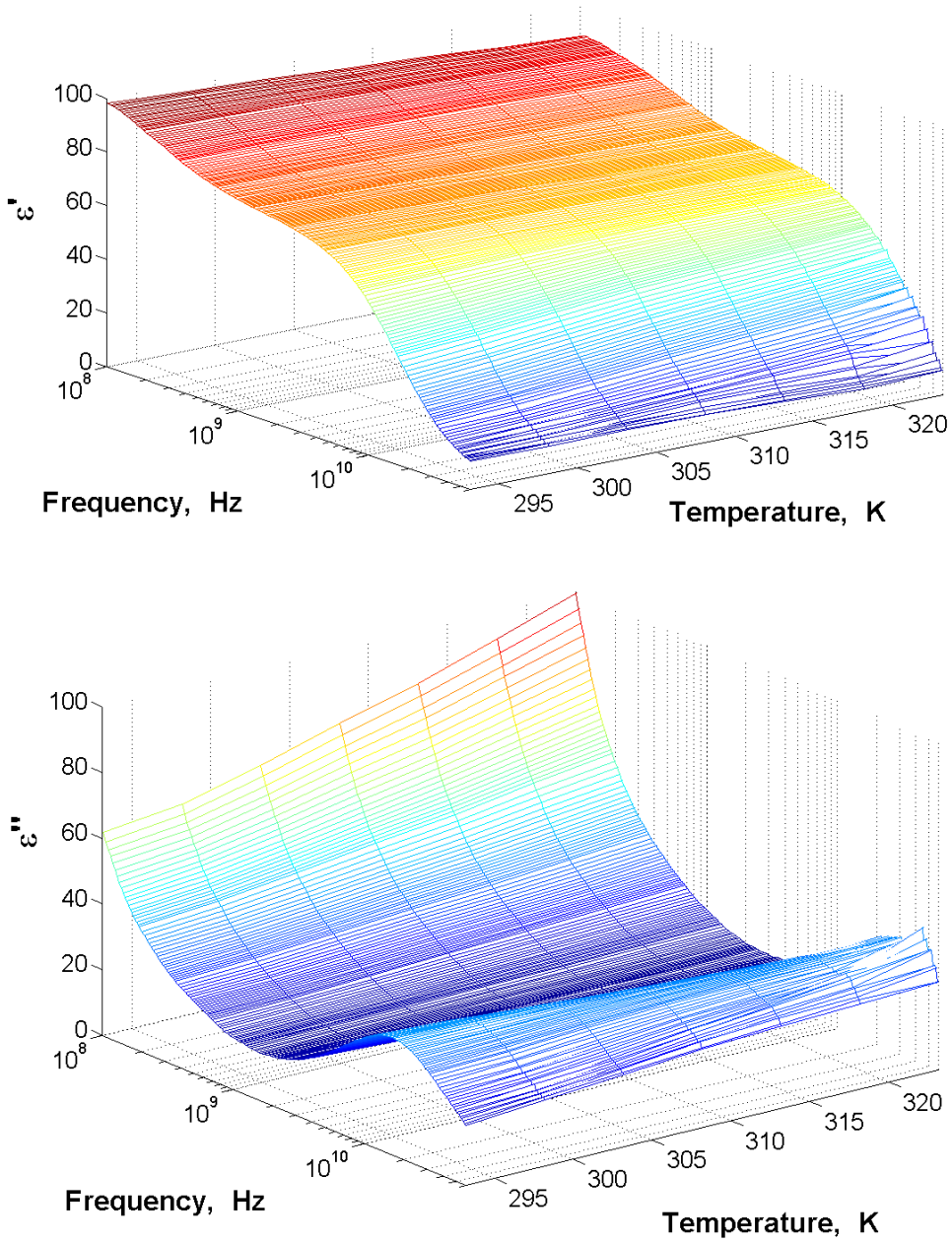

Fig. 1. Spectra of the real and imaginary part of the permittivity of an aqueous solution with an SDS concentration of 100 mmol×L^{-1} at different temperatures

Fig. 2 shows typical dielectric spectra of an aqueous solution with an SDS concentration of 100 mmol × L^{-1} at a temperature of 35 °C. Dielectric spectra were approximated by the superposition of two Cole–Cole functions and through conductivity in the Datama software package (Axelrod et al. 2004):

$$\varepsilon^*(\omega) = \varepsilon'(\omega) - i\varepsilon''(\omega) = \varepsilon_\infty + \frac{\Delta\varepsilon_{solvent}}{1+(i\omega\tau_{solvent})^{\alpha_{solvent}}} + \frac{\Delta\varepsilon_{SDS}}{1+(i\omega\tau_{SDS})^{\alpha_{SDS}}} + \frac{\sigma}{i\omega\varepsilon_0}, \quad (1)$$

where $\Delta\varepsilon$ is the increment of permittivity, τ is the relaxation time, α is the distribution coefficient of relaxation times, with $(0 < \alpha < 1)$, ε_∞ is the maximum high-frequency dielectric constant, σ is the conductivity of the sample, ε_0 is the dielectric constant of vacuum and ω is circular frequency.

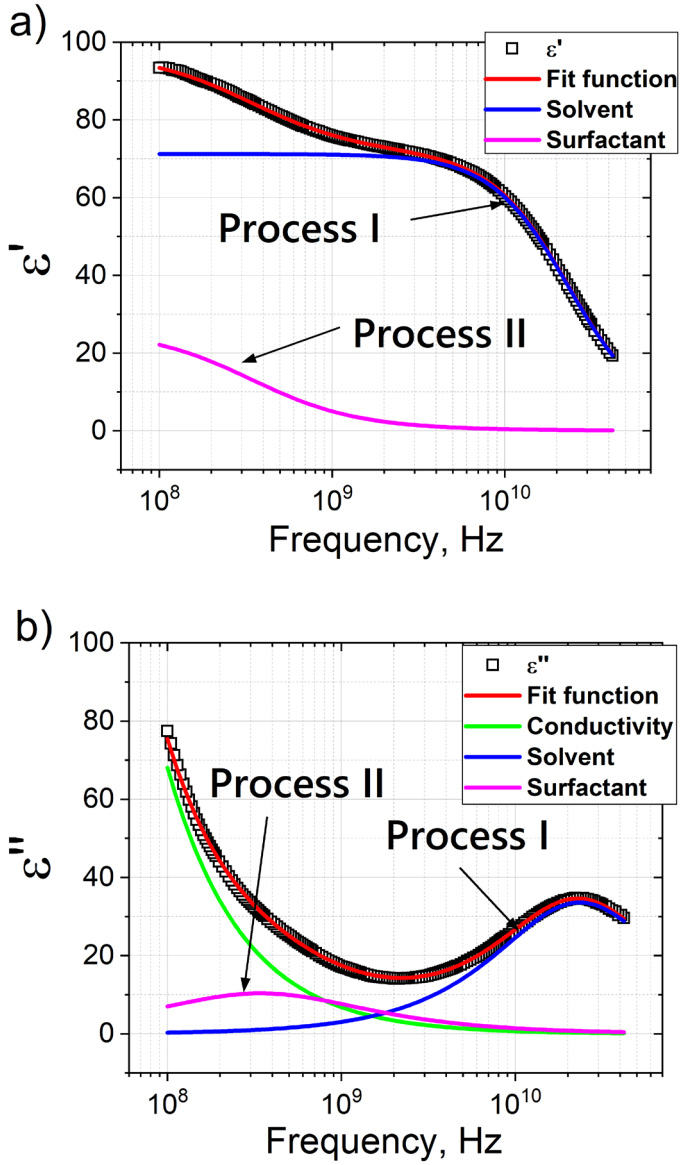

Fig. 2. Real (a) and imaginary (b) parts of the dielectric spectrum of an aqueous solution with an SDS concentration of 100 mmol × L-1 at a temperature of 35 ˚C. Hollow squares show experimental data; the red line denotes the fitting function (see equation (1)); the blue line — relaxation process 1, which corresponds to the solvent; the magenta line — relaxation process 2, which corresponds to SDS relaxation; and the green line — through conductivity

Discussion

Polarization

As a result of approximating the experimental data by equation (1), the dielectric increment $\Delta\varepsilon$ and relaxation time τ were determined. Fig. 3 shows the dependences of $\Delta\varepsilon(C_{SDS})$ at different ethanol proportions in the solvent. Let us analyze the obtained dependencies.

 https://www.doi.org/10.33910/2687-153X-2024-5-2-49-59

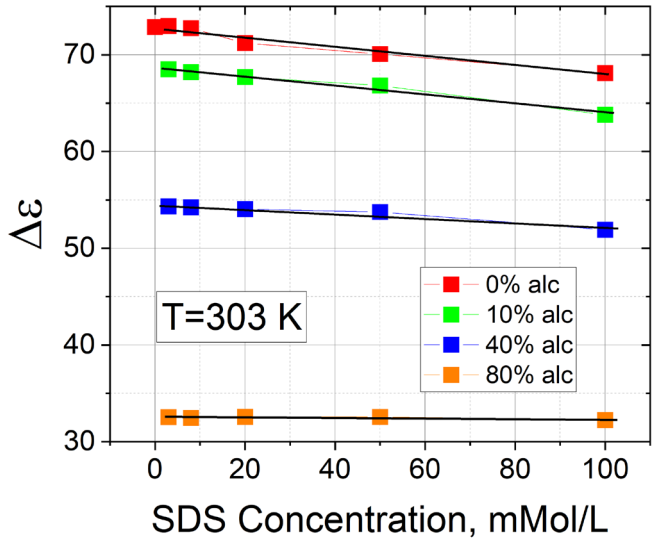

Fig. 3. Dependence of the parameter Δε (solvent) on SDS concentration in a solution with a different ethanol content; red squares — 0% ethanol; green squares — 10% ethanol; blue squares — 40% ethanol; orange squares — 80% ethanol. Data are given for a temperature of 303 K

Let us consider the dependence of Δε of the solvent on the SDS concentration in the absence of alcohol (Fig. 1a, red symbols). We can see that at a low SDS content (3 mmol × L^{-1}, 8 mmol × L^{-1}), the value of Δε practically does not change ($\Delta\varepsilon \approx 73$); with an increasing concentration, Δε decreases. Apparently, after passing the CMC point (~8.3 mmol × L^{-1}), micelles that bind part of the water (hydrate water) are formed, excluding it from the polarization process, which leads to a decrease in the Δε value.

Let us analyze the dependence of Δε of the solvent on the concentration of SDS with an alcohol content of 10% (Fig. 3a, green symbols). The presence of alcohol reduces permittivity of the solvent ($\Delta\varepsilon \approx 68$). It is known that surfactant micelles are formed due to a hydrophobic effect, when non-polar hydrocarbon radicals of a surfactant 'hide' from a polar solvent, forming spheroidal particles isolated from the solvent by a monolayer of polar head groups of the surfactant and a layer of hydration water (Romsted 2014; Rosen, Kunjappu 2012; Zueva et al. 2022). The presence of 10% ethanol in the water does not prevent the formation of micelles. The resulting micelles hydrate the solvent molecules, which leads to a decrease in $\Delta\varepsilon$ of the solvent. We cannot say which molecules, water or alcohol, are bound by micelles; however, it is known from literature that alcohol molecules can also be incorporated into the structure of micelles (Arkhipov, Idiyatullin 2012).

Now let us consider the dependence of Δε of the solvent on the concentration of SDS with an alcohol content of 40% (Fig. 3a, blue symbols). Alcohol concentration of 40 vol.% leads to a decrease in Δε of the solvent ($\Delta\varepsilon \approx 54$). The value of Δε practically does not change at SDS concentrations of 3 mmol × L^{-1}, 8 mmol × L^{-1} and 20 mmol × L^{-1}. Apparently, at this alcohol content, the formation of micelles is difficult. Therefore, a decrease in Δε of the solvent occurs only at SDS concentrations of 50 mmol × L^{-1} and 100 mmol × L^{-1}, i. e. at such an SDS content a number of micelles are still formed, which hydrate some of the solvent molecules.

Finally, let us analyze the dependence of Δε of the solvent on the concentration of SDS with an alcohol content of 80% (Fig. 3a, orange symbols). The dependence $\Delta\varepsilon(C_{SDS})$ shows that at this alcohol content, Δε of the solvent has a fairly low value ($\Delta\varepsilon \approx 32$). The $\Delta\varepsilon$ value remains practically unchanged over the entire range of SDS concentrations. This may indicate that micelles are not formed in this case, so the solvent molecules remain in a free state and all participate in the polarization process.

The effect of the solvent on micelle formation can be assessed by the slope of the $\Delta\varepsilon(C_{SDS})$ dependence in Fig. 3. The efficiency of interaction between a pair of ions depends on the permittivity of the solvent (Holmberg et al. 2002):

$$u_{eff}(r) = q_i q_j / (4\pi\varepsilon_0 \Delta\varepsilon_r r), \tag{2}$$

where $u_{eff}(r)$ is the interaction potential of two-point charges, q_i and q_j are the magnitudes of the charges, ε_0 is the dielectric constant of vacuum, $\Delta\varepsilon_r$ is the increment of permittivity, and r is the distance between the charges.

Therefore, a decrease in $\Delta\varepsilon$ leads to an increase in electrostatic repulsive forces and complicates the process of micelle formation. Accordingly, the greater the slope of the $\Delta\varepsilon(C_{SDS})$ dependence, the more efficient the micellization process. Fig. 4 shows the dependence of the slope of the $\Delta\varepsilon(C_{SDS})$ curves on the concentration of ethanol in the solvent.

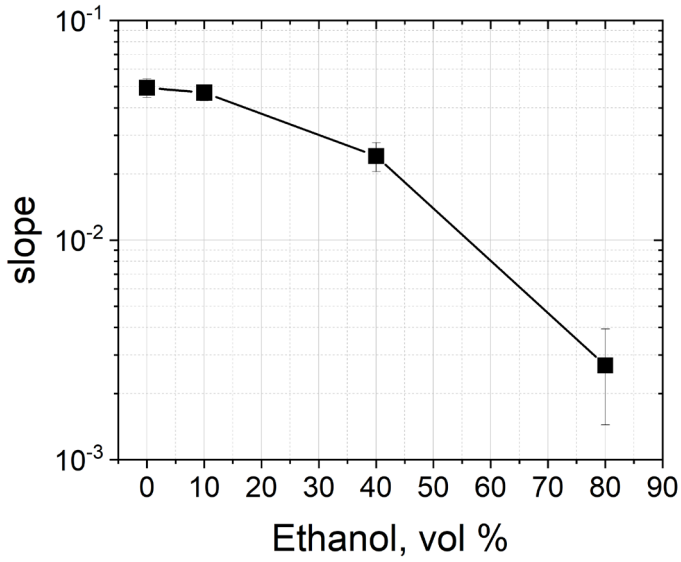

Fig. 4. Dependence of the slope of the $\Delta\varepsilon$ (C_{SDS}) curves on ethanol concentration in the solvent

Based on the dependence shown in Fig. 4, one can judge the efficiency of micellization.

Relaxation time

Let us consider the dependence of the relaxation time τ of the solvent on the SDS concentration in a solution with different ethanol content shown in Fig. 5. We can see that with increasing ethanol content the curves shift to the region of longer times. Depending on the SDS content, the τ values fluctuate around a certain average value. Apparently, the relaxation time of the solvent is practically independent of the SDS content, at least in the concentration range of 3–100 mmol × L^{-1}.

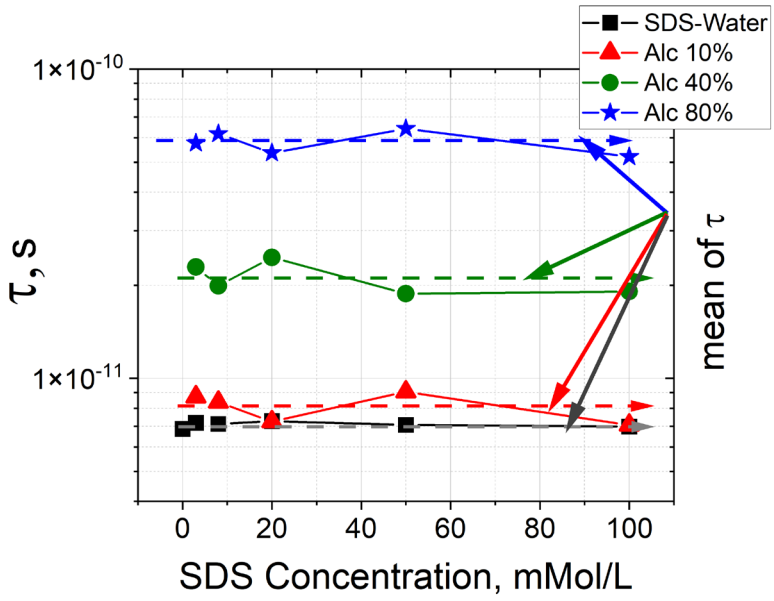

Fig. 5. Dependence of the relaxation time τ (solvent) on SDS concentration in a solution with different ethanol content; black squares — 0% ethanol; red triangles — 10% ethanol; green circles — 40% ethanol; blue stars — 80% ethanol. Data are given for a temperature of 303 K. The dotted line indicates the average values

 https://www.doi.org/10.33910/2687-153X-2024-5-2-49-59

To assess the effect of SDS content on the relaxation time of the solvent, the averaged values of τ over the SDS concentration were calculated. Fig. 6 shows a comparison of the dependences of the average relaxation time $<\tau>$ of a solvent with different SDS content on the ethanol content in the solution with the concentration dependence of the relaxation time τ for a water–ethanol mixture (T = 303 K). We can see that with an alcohol content of 80%, the $<\tau>$ and τ values are practically the same, within the error of determining $<\tau>$. With a further decrease in the proportion of alcohol, the $<\tau>$ values are slightly shorter than τ values. This can be explained by the fact that when the alcohol content decreases, a larger number of micelles are formed, and the number of counterions correspondingly increases, which, in its turn, increases the through conductivity of the system. For the hydrogen bond network of the solvent, ions are a kind of defects that break the bonds, which leads to the so-called 'blue shift' (Feldman, Ben Ishai 2021; Levy et al. 2012), i. e. shortening of the relaxation time, as observed in Fig. 6.

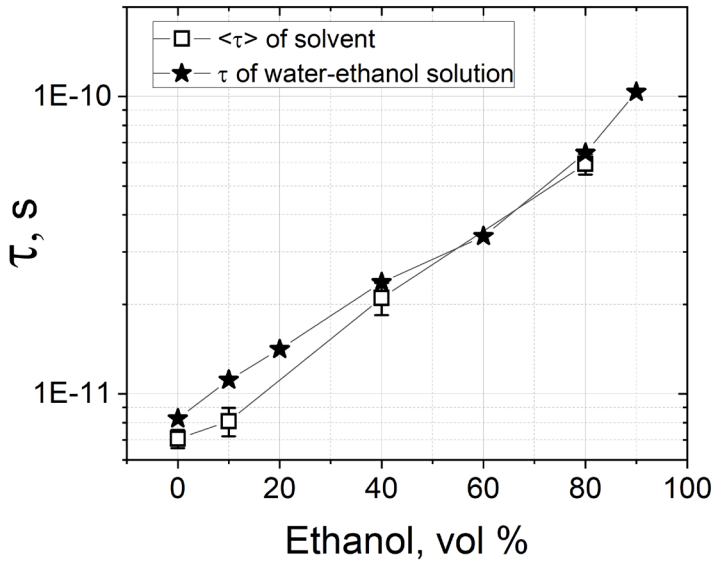

Fig. 6. Comparison of the dependences of the average relaxation time $<\tau>$ of a solvent with different SDS content on the ethanol content in the solution with the concentration dependence of the relaxation time τ for a water–ethanol mixture (Sato et al. 1999). Data are given for a temperature of 303 K

Let us consider the behavior of conductivity in aqueous solutions of SDS with different ethanol content, shown in Fig. 7. Indeed, with an increase in the proportion of ethanol in aqueous SDS solutions, the conductivity of the system decreases, which confirms the assumption that the proportion of ethanol influences the number of micelles in an aqueous SDS solution.

Some works (Wakisaka, Ohki 2005; Wakisaka et al. 2001; Zueva et al. 2021) show that water–ethanol mixtures have three characteristic concentration ranges of 0–10%, 25–40 and 60–92.3%, which share the existence of the binary water–ethanol solvent in different structural and energetic states. These states differ in the microheterogeneous structure of the solvent and in the geometry of the hydrogen bond network.

The values we obtained for the activation energy ΔE of the dielectric relaxation process of the solvent depending on the SDS concentration in a solution with different ethanol content are shown in Fig. 8. It is clearly seen that the ΔE values, depending on the ethanol proportion, fluctuate around a certain average value. There is no clear dependence on the content of SDS. Therefore, the average activation energies $<\Delta E>$ were calculated. Fig. 9 shows the dependence of the average value $<\Delta E>$ on the proportion of ethanol in the solvent.

With an increase in the ethanol proportion, the $<\Delta E>$ values increase, reaching a maximum at a volume fraction of ethanol of 40%, after which the $<\Delta E>$ value decreases. This behavior of the activation energy correlates well with the behavior of the dynamic viscosity of water–ethanol mixtures described in some works (Wakisaka, Ohki 2005; Zueva et al. 2021). Table 1 shows the averaged $<\Delta E>$ values we obtained and the already available dynamic viscosity values (Zueva et al. 2021).

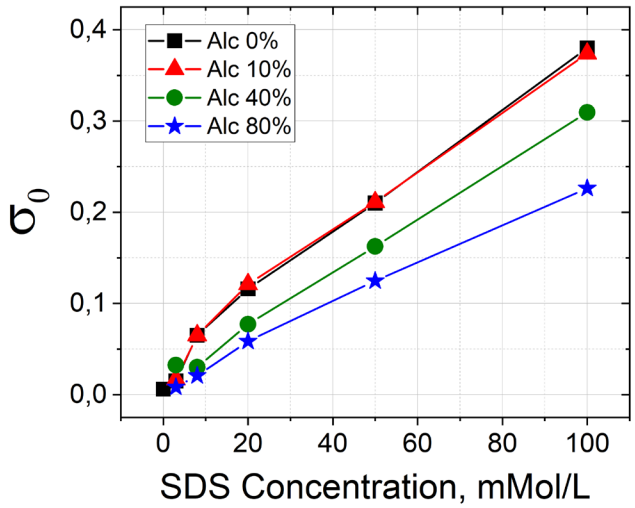

Fig. 7. Dependence of through conductivity on SDS concentration for different ethanol contents. Black squares — 0% ethanol; red triangles — 10% ethanol; green circles — 40% ethanol; blue stars — 80% ethanol. Data are given for a temperature of 303 K

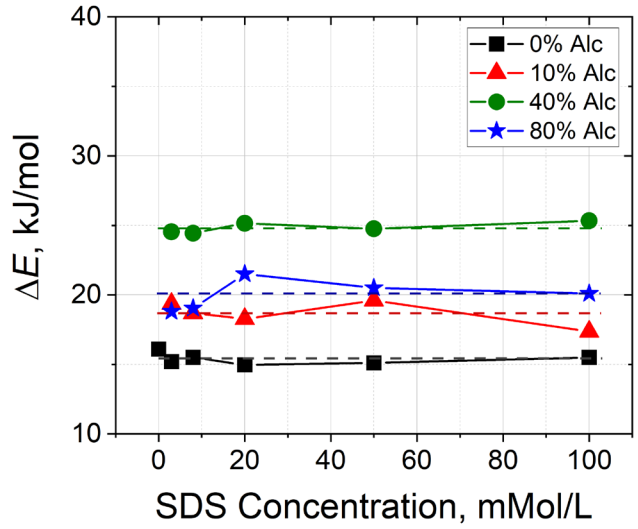

Fig. 8. Dependence of the values of activation energy Δ*E* of the dielectric relaxation process of the solvent on SDS concentration in a solution with different ethanol content; black squares — 0% ethanol; red triangles — 10% ethanol; green circles — 40% ethanol; blue stars — 80% ethanol. The dotted line indicates the average values

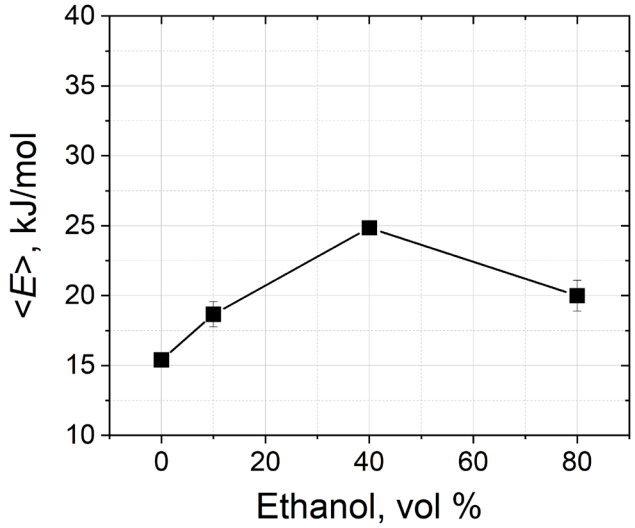

Fig. 9. Dependence of the average activation energy <Δ*E*> on ethanol proportion in the solvent

https://www.doi.org/10.33910/2687-153X-2024-5-2-49-59

Table 1. Comparison of <Δ*E*> values obtained in this work and the values of dynamic viscosity of water–ethanol mixtures taken from the work (Zueva et al. 2021)

Volume fraction of ethanol in solvent	<Δ*E*>, kJ/mol	Viscosity, mPa×s
0	15.4 ± 0.4	0.8 ± 0.016
10	18.7 ± 0.9	1.1 ± 0.02
40	24.8 ± 0.4	1.8 ± 0.02
80	19.9 ± 1.1	1.7 ± 0.02

Fig. 10 shows a comparison of the dependences of average <Δ*E*> values and dynamic viscosity values on the ethanol fraction in the solvent; good agreement is observed between the presented data. Both dependences have maximum values in the alcohol concentration range of 40–50%. One work (Wakisaka, Ohki 2005) has obtained a similar dependence of viscosity on the ethanol content in a water–ethanol mixture. Its authors explain the increase in viscosity by the formation of ethanol self-association clusters; ethanol clusters grow when mixed with water, and their formation reaches a maximum of about 40–50 wt.% ethanol.

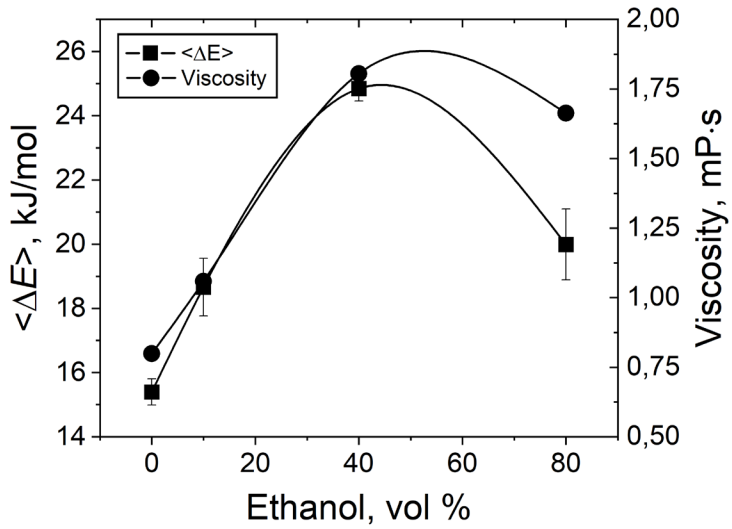

Fig. 10. Mutual correlation between averaged <Δ*E*> values and dynamic viscosity values

Viscosity is related to the molecular dielectric relaxation time by the Debye relation:

$$\tau_{\mu} = \frac{4\pi a^3 \eta}{kT}, \tag{3}$$

The relationship between molecular time τ_{μ} and macroscopic time is given by the Pauls expression (Powles 1953):

$$\tau = \frac{3\varepsilon_s}{2\varepsilon_s + \varepsilon_{\infty}} \tau_{\mu}, \tag{4}$$

The relaxation time τ is related to the change in the dipole relaxation activation energy ΔE by the following relationship (Greinacher 1948; Lewis, Smyth 1939):

$$\tau = \frac{hN}{RT} \exp\left[\frac{\Delta E}{RT}\right], \tag{5}$$

where h — Planck's constant; R — the gas constant; N — Avogadro's number.

Thus, the activation energy of the dielectric relaxation process is related to the structural features of the solution.

Conclusion

We have shown that in binary water–ethanol mixtures the process of SDS micelle formation changes significantly, which clearly follows from the characteristics of dielectric relaxation. In the region of high water concentrations, when the structure of water dominates, the process of SDS micellization in an aqueous ethanol medium does not differ significantly from an aqueous surfactant solution. In the region of average water concentrations, the micelle-forming properties of the surfactant are only partially preserved. In the region of high ethanol concentrations, the tendency of surfactant molecules to associate remains, but the sizes of associates are obviously small, which we have shown previously using other methods (Zueva et al. 2021). Based on the results obtained, the following conclusions can be drawn:

1. The formation of micelles leads to an increase in the through conductivity of the solution and a slight decrease in permittivity, proportional to the increase in the SDS concentration (the number of micelles);
2. An increase in the proportion of ethanol in the solvent complicates the process of SDS micellization since the presence of alcohol reduces the polarity of the solvent, which accordingly reduces the apparent value of the hydrophilic–lipophilic balance (HLB) of the surfactant. It has been established that with an increase in the ethanol fraction, the slope of the $\Delta\varepsilon(C_{SDS})$ dependence decreases; this parameter can be used to judge the efficiency of micellization;
3. Analysis of the dependences $<\Delta E>(C_{alc}, \%)$ and $\eta(C_{alc}, \%)$ presented in Figs. 8, 9 and 10 allows us to conclude that the structural state of the binary water–ethanol solvent is mainly determined by the composition of the solvent (ethanol content) and weakly depends on the SDS content.

Conflict of Interest

The authors declare no potential or apparent conflicts of interest.

Author Contributions

All the authors discussed the final work and took an equal part in writing the article.

References

Arkhipov, V. P., Idiyatullin, Z. Sh. (2012) Raspredelenie molekul etanola mezhdu mitsellyarnoj i vodnoj fazami v vodno-etanol'nykh rastvorakh dodetsilsul'fata natriya [Distribution of ethanol molecules between the micellar and aqueous phases in aqueous-ethanol solutions of sodium dodecilsulphate]. *Vestnik tekhnologicheskogo universiteta — Bulletin of the Technological University*, 15 (9), 11–14. (In Russian)

Asenbaum, A., Pruner, C., Wilhelm, E. et al. (2012) Structural changes in ethanol–water mixtures: Ultrasonics, Brillouin scattering and molecular dynamics studies. *Vibrational Spectroscopy*, 60, 102–106. https://doi.org/10.1016/j.vibspec.2011.10.015 (In English)

Axelrod, N., Axelrod, E., Gutina, A. et al. (2004) Dielectric spectroscopy data treatment: I. Frequency domain. *Measurement Science and Technology*, 15 (4), 755–764. https://doi.org/10.1088/0957-0233/15/4/020 (In English)

Beddard, G. S., Doust, T., Hudales, J. (1981) Structural features in ethanol–water mixtures revealed by picosecond fluorescence anisotropy. *Nature*, 294 (5837), 145–146. https://doi.org/10.1038/294145a0 (In English)

Brai, M., Kaatze, U. (1992) Ultrasonic and hypersonic relaxations of monohydric alcohol/water mixtures. *The Journal of Physical Chemistry*, 96 (22), 8946–8955. https://doi.org/10.1021/j100201a046 (In English)

Buchner, R., Baar, C., Fernandez, P. et al. (2005) Dielectric spectroscopy of micelle hydration and dynamics in aqueous ionic surfactant solutions. *Journal of Molecular Liquids*, 118 (1–3), 179–187. https://doi.org/10.1016/j.molliq.2004.07.035 (In English)

Dutt, G. B., Doraiswamy, S. (1992) Picosecond reorientational dynamics of polar dye probes in binary aqueous mixtures. *The Journal of Chemical Physics*, 96 (4), 2475–2491. https://doi.org/10.1063/1.462052 (In English)

Faizullin, D. A., Konnova, T. A., Haertlé, T., Zuev, Y. F. (2017) Secondary structure and colloidal stability of beta-casein in microheterogeneous water-ethanol solutions. *Food Hydrocolloids*, 63, 349–355. https://doi.org/10.1016/j.foodhyd.2016.09.011 (In English)

Feldman, Y., Ben Ishai, P. (2021) The Microwave response of water as the measure of interactions in a complex liquid. In: W. H. Hunter Woodward (ed.). *Broadband Dielectric Spectroscopy: A Modern Analytical Technique*. Washington: American Chemical Society Publ., pp. 283–300. https://doi.org/10.1021/bk-2021-1375.ch013 (In English)

Gnezdilov, O. I., Zuev, Y. F., Zueva, O. S. et al. (2011) Self-diffusion of ionic surfactants and counterions in premicellar and micellar solutions of sodium, lithium and cesium dodecyl sulfates as studied by NMR-diffusometry. *Applied Magnetic Resonance*, 40, 91–103. https://doi.org/10.1007/s00723-010-0185-1 (In English)

Greinacher, H. (1948) Uber eine methode zur bestimmung der dielektrizitatskonstanten von flussigkeiten [About a method for determining the dielectric constants of liquids]. *Helvetica Physica Acta*, 21 (3–4), 261–272. (In German)
Gubaidullin, A. T., Litvinov, I. A., Samigullina, A. I. et al. (2016) Structure and dynamics of concentrated micellar solutions of sodium dodecyl sulfate. *Russian Chemical Bulletin*, 65, 158–166. https://doi.org/10.1007/s11172-016-1278-2 (In English)
Halder, R., Jana, B. (2018) Unravelling the composition-dependent anomalies of pair hydrophobicity in water–ethanol binary mixtures. *The Journal of Physical Chemistry B*, 122 (26), 6801–6809. https://doi.org/10.1021/acs.jpcb.8b02528 (In English)
Holmberg, K., Jönsson, B., Kronberg, B., Lindman, B. (2002) Intermolecular interactions. In: *Surfactants and Polymers in Aqueous Solution*. 2nd ed. Chichester: John Wiley & Sons Publ., pp. 157–174. https://doi.org/10.1002/0470856424.ch7 (In English)
Hu, N., Wu, D., Cross, K. et al. (2010a) Structurability: A collective measure of the structural differences in vodkas. *Journal of Agricultural and Food Chemistry*, 58 (12), 7394–7401. https://doi.org/10.1021/jf100609c (In English)
Hu, N., Wu, D., Cross, K. J., Schaefer, D. W. (2010b) Structural basis of the 1 H-nuclear magnetic resonance spectra of ethanol–water solutions based on multivariate curve resolution analysis of mid-infrared spectra. *Applied Spectroscopy*, 64 (3), 337–342. https://doi.org/10.1366/000370210790918373 (In English)
Konnova, T. A., Faizullin, D. A., Haertlé, T., Zuev, Y. F. (2013) β-casein micelle formation in water-ethanol solutions. *Doklady Biochemistry and Biophysics*, 448 (1), 36–39. https://doi.org/10.1134/S1607672913010092 (In English)
Levy, E., Puzenko, A., Kaatze, U. et al. (2012) Dielectric spectra broadening as the signature of dipole-matrix interaction. II. Water in ionic solutions. *The Journal of Chemical Physics*, 136 (11), article 114503. https://doi.org/10.1063/1.3691183 (In English)
Lewis, G. L., Smyth, C. P. (1939) The dipole moments and structures of ozone, silicobromoform and dichlorogermane. *Journal of the American Chemical Society*, 61 (11), 3063–3066. https://doi.org/10.1021/ja01266a026 (In English)
Mashimo, S., Umehara, T., Redlin, H. (1991) Structures of water and primary alcohol studied by microwave dielectric analyses. *The Journal of Chemical Physics*, 95 (9), 6257–6260. https://doi.org/10.1063/1.461546 (In English)
Mijaković, M., Kežić, B., Zoranić, L. et al. (2011) Ethanol-water mixtures: Ultrasonics, Brillouin scattering and molecular dynamics. *Journal of Molecular Liquids*, 164 (1–2), 66–73. https://doi.org/10.1016/j.molliq.2011.06.009 (In English)
Nishikawa, K., Iijima, T. (1993) Small-angle x-ray scattering study of fluctuations in ethanol and water mixtures. *The Journal of Physical Chemistry*, 97 (41), 10824–10828. https://doi.org/10.1021/j100143a049 (In English)
Powles, J. G. (1953) Dielectric relaxation and the internal field. *The Journal of Chemical Physics*, 21 (4), 633–637. https://doi.org/10.1063/1.1698980 (In English)
Romsted, L. S. (ed.). (2014) *Surfactant science and technology: Retrospects and prospects*. Boca Raton: CRC Press, 593 p. https://doi.org/10.1201/b16802 (In English)
Rosen, M. J., Kunjappu, J. T. (2012) *Surfactants and interfacial phenomena*. New Jersey: John Wiley & Sons Publ., 616 p. http://dx.doi.org/10.1002/9781118228920 (In English)
Sato, T., Buchner, R. (2004) Dielectric relaxation processes in ethanol/water mixtures. *The Journal of Physical Chemistry A*, 108 (23), 5007–5015. https://doi.org/10.1021/jp035255o (In English)
Sato, T., Chiba, A., Nozaki, R. (1999) Dynamical aspects of mixing schemes in ethanol–water mixtures in terms of the excess partial molar activation free energy, enthalpy, and entropy of the dielectric relaxation process. *The Journal of Chemical Physics*, 110 (5), 2508–2521. https://doi.org/10.1063/1.477956 (In English)
Soper, A. K., Dougan, L., Crain, J., Finney, J. L. (2006) Excess entropy in alcohol–water solutions: A simple clustering explanation. *The Journal of Physical Chemistry B*, 110 (8), 3472–3476. https://doi.org/10.1021/jp054556q (In English)
Wakisaka, A., Komatsu, S., Usui, Y. (2001) Solute-solvent and solvent-solvent interactions evaluated through clusters isolated from solutions: Preferential solvation in water-alcohol mixtures. *Journal of Molecular Liquids*, 90 (1–3), 175–184. https://doi.org/10.1016/S0167-7322(01)00120-9 (In English)
Wakisaka, A., Ohki, T. (2005) Phase separation of water–alcohol binary mixtures induced by the microheterogeneity. *Faraday Discussions*, 129, 231–245. https://doi.org/10.1039/B405391E (In English)
Zuev, Yu. F., Kurbanov, R. Kh., Idiyatullin, B. Z., Us'yarov, O. G. (2007) Sodium dodecyl sulfate self-diffusion in premicellar and low-concentrated micellar solutions in the presence of a background electrolyte. *Colloid Journal*, 69, 444–449. https://doi.org/10.1134/S1061933X07040059 (In English)
Zuev, Yu. F., Lunev, I. V., Turanov, A. N., Zueva, O. S. (2024) Micellization of sodium dodecyl sulfate in the vicinity of Krafft point: An NMR and dielectric spectroscopy study. *Russian Chemical Bulletin*, 73 (3), 529–535. https://doi.org/10.1007/s11172-024-4162-5 (In English)
Zueva, O. S., Kusova, A. M., Makarova, A. O. et al. (2020) Reciprocal effects of multi-walled carbon nanotubes and oppositely charged surfactants in bulk water and at interfaces. *Colloids and Surfaces A: Physicochemical and Engineering Aspects*, 603, article 125296. https://doi.org/10.1016/j.colsurfa.2020.125296 (In English)
Zueva, O. S., Makarova, A. O., Khairutdinov, B. I. et al. (2021) Association of ionic surfactant in binary water—ethanol media as indicator of changes in structure and properties of solvent. *Russian Chemical Bulletin*, 70, 1185–1190. https://doi.org/10.1007/s11172-021-3203-6 (In English)
Zueva, O. S., Rukhlov, V. S., Zuev, Yu. F. (2022) Morphology of ionic micelles as studied by numerical solution of the Poisson equation. *ACS omega*, 7 (7), 6174–6183. https://doi.org/10.1021/acsomega.1c06665 (In English)

Condensed Matter Physics.
Physics of thin films.
Surfaces and interfaces

UDC 537.226.4

EDN GHTKLC
https://www.doi.org/10.33910/2687-153X-2024-5-2-60-66

Piezoelectric properties of spherulite thin films of lead zirconate titanate

S. V. Senkevich ✉[1], D. A. Kiselev [2], M. V. Staritsyn [3], E. Yu. Kaptelov [1], I. P. Pronin [1]

[1] Ioffe Institute, 26 Polytekhnicheskaya Str., Saint Petersburg 194021, Russia
[2] National University of Science and Technology "MISiS", 4/1 Leninsky Ave., Moscow 119049, Russia
[3] NRC "Kurchatov Institute" — CRISM "Prometey", 49 Shpalernaya Str., Saint Petersburg 191015, Russia

Authors

Stanislav V. Senkevich, ORCID: 0000-0002-4503-1412, e-mail: senkevichsv@mail.ioffe.ru

Dmitry A. Kiselev, ORCID: 0000-0003-1047-3007, e-mail: dm.kiselev@misis.ru

Mikhail V. Staritsyn, ORCID: 0000-0002-0088-4577, e-mail: ms_145@mail.ru

Evgeny Yu. Kaptelov, ORCID: 0000-0002-7423-6943, e-mail: kaptelov@mail.ioffe.ru

Igor P. Pronin, ORCID: 0000-0003-3749-8706, e-mail: petrovich@mail.ioffe.ru

For citation: Senkevich, S. V., Kiselev, D. A., Staritsyn, M. V., Kaptelov, E. Yu., Pronin, I. P. (2024) Piezoelectric properties of spherulite thin films of lead zirconate titanate. *Physics of Complex Systems*, 5 (2), 60–66. https://www.doi.org/10.33910/2687-153X-2024-5-2-60-66 EDN GHTKLC

Received 12 April 2024; reviewed 26 April 2024; accepted 26 April 2024.

Funding: The study did not receive any external funding.

Abstract. We studied thin films of lead zirconate titanate, characterized by a spherulitic radial-radiant microstructure, the composition of which corresponds to the region of the morphotropic phase boundary, using the piezoelectric response force microscopy method. Features of the vertical and lateral piezoresponses and the surface potential (Kelvin mode) were revealed. We also compared the piezoelectric response with the radial microstructure features and mechanical stresses formed in the films as a result of crystallization of the perovskite phase from the amorphous phase.

Keywords: piezoelectric force microscopy, lead zirconate titanate thin films, radial-radiant spherulitic microstructure, mechanical stresses, surface potential

Introduction

It is well known that the synthesis of various kinds of thin films, both organic and inorganic materials, can result in the formation of polycrystalline spherulitic structures. Crystallization of spherulites can occur both from solutions and from a solid amorphous phase or during recrystallization of one or another phase (Kooi et al. 2004; Shtukenberg et al. 2012; 2014).

The formation of thin-film spherulitic structures occurs through the nucleation and growth of islands close in shape to ideal disks. The growth of spherulites is accompanied by the formation (branching) of low-angle fibrils (Shtukenberg et al. 2012). The forms in which spherulite structures occur are very diverse, to the point that in one compound, the microstructure of the spherulites can change radically when the synthesis temperature changes.

Among the most common and still the least studied spherulitic forms is the radial microstructure. Such formations, in particular, have been discovered and studied in semiconductors and various

thin-film oxides — from metal oxides and quartzites to perovskite oxides (Alkoy et al. 2007; Kolosov, Thölén 2000; Kolosov et al. 2005; Pronin et al. 2018; 2023; Spierings et al. 1993; Staritsyn et al. 2023b; Zhigalina et al. 2018). Studies over the last two decades have shown that the growth of such spherulites is accompanied by a rotation of the growth axis. In quartz (SiO2, GeO2) and perovskite (Pb(Zr,Ti)O3) structures, the tilting gradient ranges from fractions to several degrees per micron (Lutjes et al. 2021; Musterman et al. 2022; Staritsyn et al. 2023b) while in some metal oxides, PLZT and semiconductors it is two orders of magnitude higher (Kolosov, Thölén 2000; Kolosov et al. 2005; Zhigalina et al. 2018). In the latter case, such structures are called transrotation crystals. According to (Lutjes et al. 2021; Musterman et al. 2022; Staritsyn et al. 2023b), the reason for the rotation of the growth axis during the solid-state crystallization of films lies in the mechanical stresses acting in the plane of the substrate caused by changes in the density of the initial and final phases.

Interest in studying the properties of spherulitic ferroelectric films of lead zirconate tatanate ($Pb(Zr,Ti)O_3$ or PZT) is due to the practical lack of data on this topic as well as the fact that PZT solid solutions of compositions corresponding to the region of the morphotropic phase boundary are currently the main materials for microelectromechanical devices (Izyumskaya et al. 2007; Song et al. 2021). The purpose of this work was to study the piezoelectric properties of spherulitic thin films of PZT formed on a platinized silicon substrate.

Sample preparation and research methods

Samples of PZT thin films were prepared by radio-frequency magnetron sputtering of a ceramic target onto a platinized silicon ($Pt/TiO_2/SiO_2/Si$) substrate. The composition of the stoichiometric target $PbZr_{0.54}Ti_{0.46}O_3$ corresponded to the region of the morphotropic phase boundary separating the tetragonal and rhombohedral (monoclinic) modifications of the ferroelectric phase (Cox et al. 2005; Staritsyn et al. 2023a). Deposition occurred at a low temperature and was determined by the heating temperature of the gas argon–oxygen plasma. The substrate temperature could be changed in the range of 90–160 °C by varying the target–substrate distance in the range from 70 to 30 mm (Pronin et al. 2023; Staritsyn et al. 2023a). This led to a change in the concentration of nucleation centers of the perovskite phase by approximately three times, and the average sizes of spherulite blocks, which are polygons, changed from approximately 10–15 to 40–50 μm. High-temperature annealing of the resulting amorphous films was carried out in the air in a SUOL 0.3.2/12 type tube furnace. The accuracy of temperature maintenance did not exceed 0.5 degrees. To obtain island perovskite films, the annealing temperature was 530–550 °C, at which the diameter of the spherulite islands reached 20–30 μm. To obtain continuous films, the temperature was increased to 580 °C. The thickness of the films under study was 500 nm.

Measurements of the piezoelectric response of PZT thin films were carried out using piezoresponse force microscopy (PFM) and Kelvin probe force microscopy (KPFM). To determine the vertical and lateral piezoresponses, an atomic force microscope (Ntegra Prima, NT-MDT SI, Russia) equipped with platinum-coated cantilevers (NSG01, NT-MDT SI, Russia) with a spring stiffness of ~5 N/m was used. The piezoresponse signal and its phase were measured in the contact mode by applying an alternating voltage of 5 V to the cantilever at a frequency of 50 kHz. The area of the scanned surface was 40×40 μm.

Experiments to determine the surface potential (Kelvin modes) were carried out using the same atomic force microscope. For KPFM measurements, the surface topography was first scanned in semi-contact mode, and then the probe was raised to a height of 50 nm, with a voltage of 1 V applied to it. All KPFM mappings were performed at room temperature, each mapping taking about 30 minutes.

Experimental results and their discussion

In island spherulitic films, the most significant results were obtained when studying the lateral piezoresponse and surface potential. Fig. 1 shows images of the lateral response (a–c) and the Kelvin mode signal (g–i) as well as the diametric distributions of the corresponding signals (d–f) and (j–l) respectively, for islands differing in size and the stage of crystallization of the perovskite phase. The diametral section of the lateral polarization indicates a radial distribution of polarization, from a signal close to zero to a maximum signal recorded near the interface of the spherulitic island with the nonpolar low-temperature pyrochlore phase surrounding the island. The polarization vector is directed from the center of the island towards the periphery. That is why, in the diametrical distribution, the signal of the lateral piezoresponse in the center of the island passes through the zero mark.

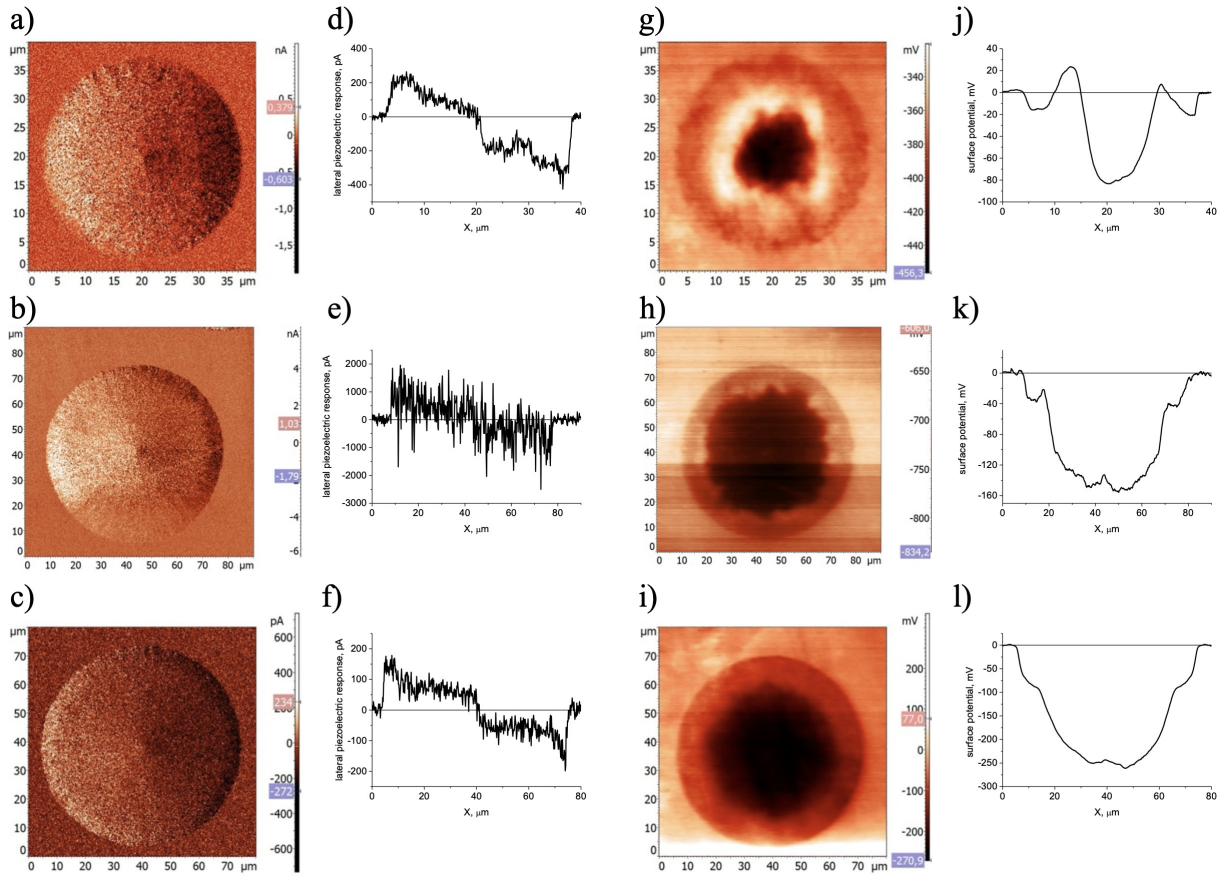

Fig. 1. Images of the lateral piezoelectric response (a, b, c) and surface potential (Kelvin mode) (g, h, i) of perovskite islands at different recrystallization stages of the perovskite phase with the corresponding diametrical horizontal signal distributions, (d, e, f) and (j, k, l)

We previously observed a similar behavior of the lateral piezoresponse (Kiselev et al. 2023), and to date it has been confirmed by the results of studying island spherulitic films of various sizes. However, it turned out that the nature of the polarization distribution can differ significantly in amplitude near the center of the island when reaching the shelf and near the edge, Fig. 1 (g–i). A clearer understanding of the crystallization processes of radial-radiant spherulite islands (and the continuous perovkite phase consisting of spherulitic blocks) is provided by data on the Kelvin mode of the studied islands, Fig. 1(d–e) and (j–l). The results indicate the presence of an intermediate (less dense) perovskite phase, characterized by a less ordered perovskite structure and the presence of numerous pores. The region of the spherulite island, where a change in the sign of the surface potential is observed, is a zone of recrystallization of the perovskite phase, which is most clearly visible in Fig. 1 (d–f) and (j–l). The completion of the recrystallization process of the perovskite phase is accompanied by a more uniform distribution of both the lateral piezoresponse signal and the surface potential, Fig. 1f and 1l.

Noteworthy is the negative potential both in the region of the intermediate perovskite phase and in its denser modification. The reasons for the formation of a negative surface potential are apparently related to the presence of traps at the interface between the thin film and the environment, as well as at the lower interface, occupied by electrons that are more mobile charges, Fig. 2. The reasons for the change in potential during recrystallization of the perovskite phase require additional study.

The mechanism of the appearance of radially oriented lateral polarization is in some respects similar to the mechanism of spontaneous polarization oriented normally to the film/substrate plane. In the case of self-polarization, the driving force is the localization of mobile charges (electrons) at deep traps of the morphologically developed thin film/bottom (platinum) electrode interface (Fig. 2) and the reorientation of ferroelectric dipoles under the influence of the electric field of the formed space charge (Balke et al. 2009; Pronin et al. 2003).

 https://www.doi.org/10.33910/2687-153X-2024-5-2-60-66

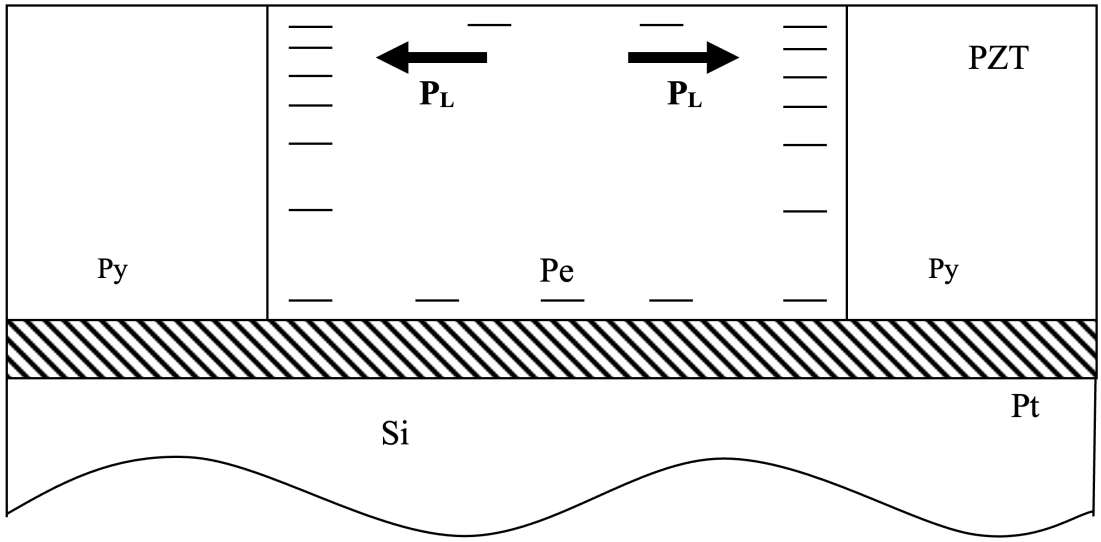

Fig. 2. Model radial section of the emergence of lateral polarization (P_L) in spherulitic perovskite (Pe) island (radial section) surrounded by low-temperature pyrochlore (Py) phase as a result of inhomogeneous space charge distribution

In our case, the difference in the mechanism for the appearance of radial-lateral polarization is, on the one hand, associated with the action of tensile radial stresses that orient ferroelectric dipoles in the plane of the thin film in directions as close as possible to the radial ones; on the other hand, it has to do with the action of the electric field formed by the localization of mobile charge carriers (electrons) on the loose (porous) perovskit–pyrochlore interface, Fig. 2. In this case, the lower interface (PZT/Pt) of the film is an equipotential surface, and the charges concentrated at the interface of the island with the pyrochlore phase are nonuniformly distributed throughout the thickness of the island, with the maximum potential near the free surface.

The results of studying the piezoelectric properties of continuous spherulitic films are presented in Figs. 3 and 4. To date, the data obtained on the vertical piezoresponse of thin films differing in the size of the spherulitic blocks (with varying target–substrate distance) have been systematized. Research on the lateral piezoelectric effect and surface potential and their analysis require significant additional efforts, and their results will be published later.

The first column of Fig. 3 reflects the PFM image (self-polarization) of the vertical signal; the second column is the distribution of the amplitude of the self-polarization signal over the scanning area; the third column is the PFM image of the vertical piezoresponse signal after polarization of the film with a voltage of +40 V and –40 V, respectively; and the fourth column is the distribution of the piezoresponse during repolarization films along horizontal sections.

Fig. 4 accumulates the study results presented in Fig. 3 when varying the target–substrate distance in the range d = 30–70 mm. The upper figure (Fig. 4a) shows the change in the self-polarization averaged over the scanning area. It can be seen that as d increases, the dependence passes through a minimum (at d = 40 mm), reaches a maximum and then decreases again. Similarly, a decrease in the value of residual polarization P_r (Fig. 4b) calculated as the average value under the positive and negative influence of a strong polarizing electric field is observed.

The passage of both dependencies through a minimum at d = 40 mm correlates with the ideas developed in some works (Kiselev et al. 2023; Pronin et al. 2023; Staritsyn et al. 2023a; 2023b), namely that an increase in the size of spherulitic blocks leads to an increase in lateral tensile mechanical stresses and, as a consequence, to an increase in the rotation gradient of the growth axis and the appearance of new open high-angle boundaries. It can be assumed that strong mechanical stresses can induce a phase transition in films associated with the rotation of oxygen octahedra (antiferrodistortion phase transition), which leads both to a decrease in the crystal lattice parameter of the perovskite structure and to the appearance of dielectric anomalies in the films of compositions corresponding to the region of the morphotropic phase boundary (Staritsyn et al. 2023a).

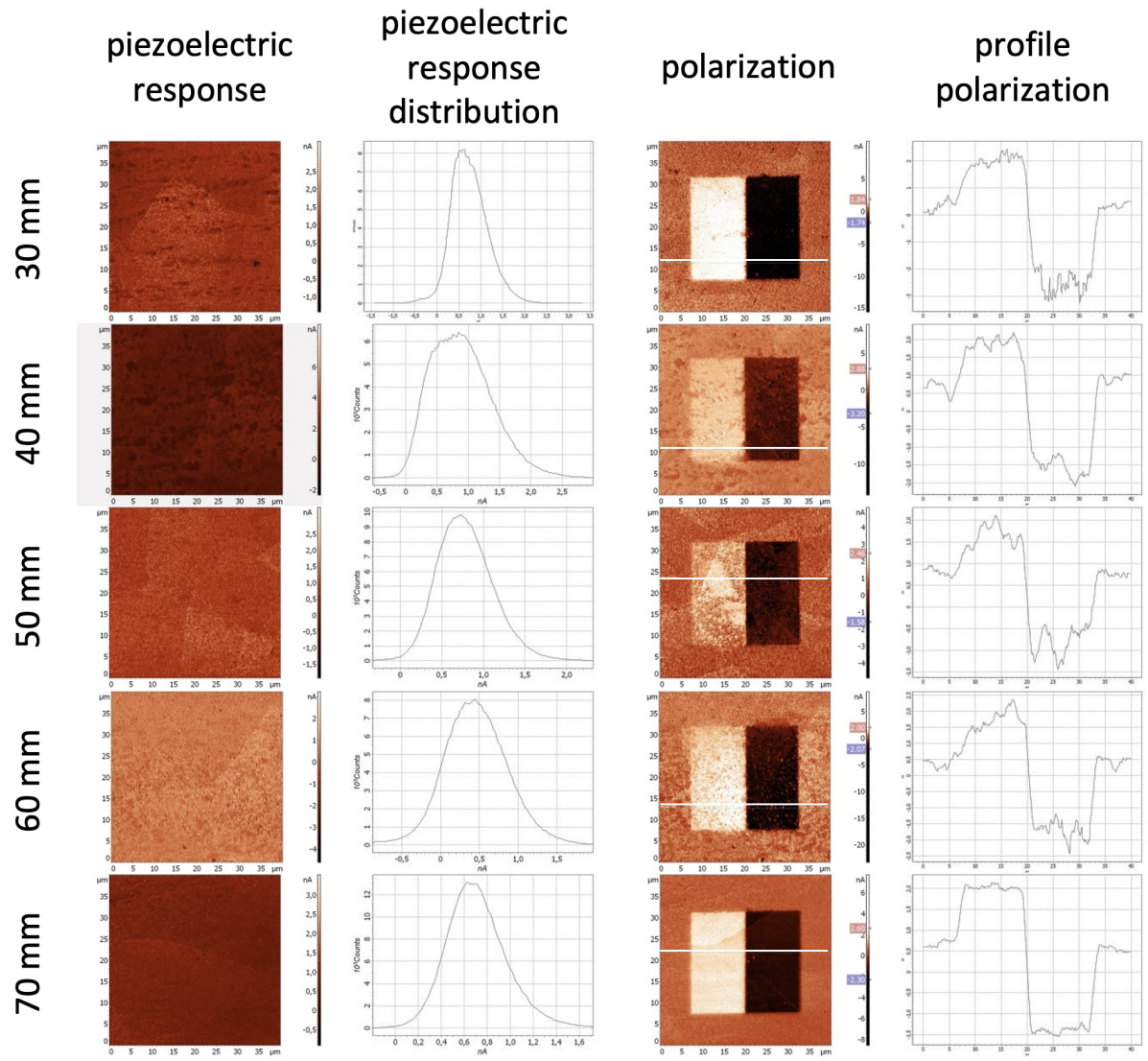

Fig. 3. Images of the piezoelectric response of PZT films (the first column — self-polarized films) with histograms of the distribution of the piezoelectric response over their area (the second column — self-polarization), piezoelectric response after polarization with positive +40 V (light areas) and negative –40 V (dark areas) voltage (the third column) with corresponding cross-section profiles (the fourth column)

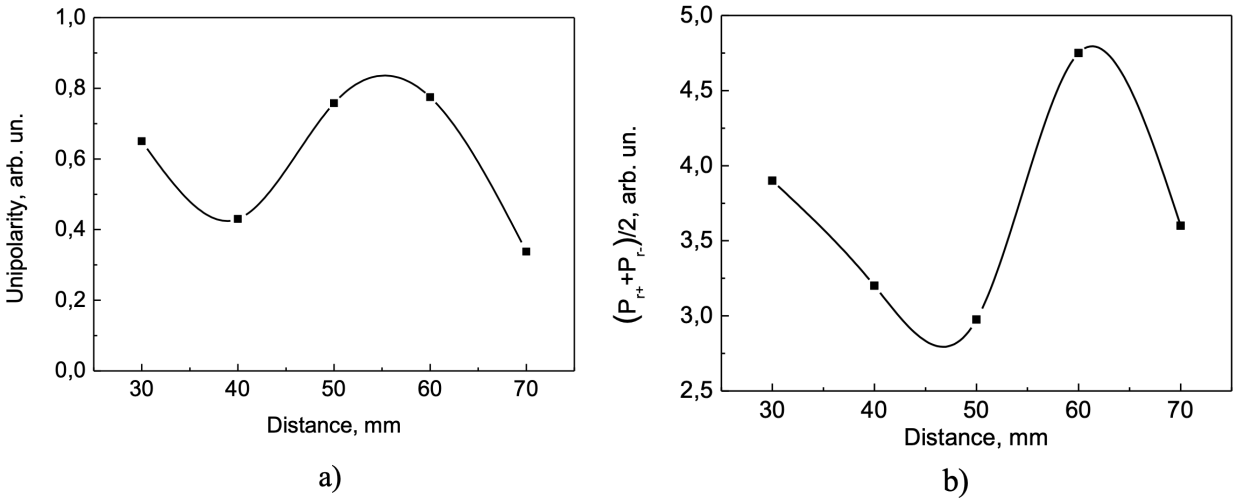

Fig. 4. Changes in self-polarization (a) and residual polarization (b) measured from the piezoelectric response of PZT versus target–substrate distance

https://www.doi.org/10.33910/2687-153X-2024-5-2-60-66

Conclusions

A study of the piezoelectric properties of island and continuous spherulitшc PZT films showed that:
— phase recrystallization leads to anomalous changes in the lateral polarization and surface potential of perovskite islands;
— a mechanism for the formation of radial-radiant polarization is proposed, associated with the polarizing effect of a negative bulk charge accumulated at the interface of the island with the pyrochlore phase;
— in continuous spherulitic films, a nonlinear change in self-polarization and residual polarization was revealed with an increasing size of spherulitic blocks;
— it is assumed that anomalous changes in the structure and physical properties of spherulitic films are associated with the induction of octahedra tilting of the perovskite lattice, caused by the action of strong lateral tensile stresses.

Conflict of Interest

The authors delare that there is no conflict of interest, either existing or potential.

Author Contributions

The authors have made an equal contribution to the preparation of this paper.

References

Alkoy, E. M, Alkoy, S., Shiosaki, T. (2007) The effect of crystallographic orientation and solution aging on the electrical properties of sol-gel derived $Pb(Zr_{0.45}Ti_{0.55})O_3$ thin films. Ceramics International, 33 (8), 1455–1462. https://doi.org/10.1016/j.ceramint.2006.06.010 (In English)

Balke, N., Bdikin, I., Kalinin, S. V., Kholkin, A. L. (2009) Electromechanical imaging and spectroscopy of ferroelectric and piezoelectric materials: State of the art and prospects for the future. Journal of the American Ceramic Society, 92 (8), 1629–1647. https://doi.org/10.1111/j.1551-2916.2009.03240.x (In English)

Cox, D. E., Noheda, B., Shirane, G. (2005) Low-temperature phases in $PbZr_{0.52}Ti_{0.48}O_3$: A neutron powder diffraction study. Physical Review B, 71 (13), article 134110. https://doi.org/10.1103/PhysRevB.71.134110 (In English)

Izyumskaya, N., Alivov, Y.-I., Cho, S.-J. et al. (2007) Processing, structure, properties, and applications of PZT thin films. Critical Reviews in Solid State and Materials Sciences, 32 (3–4), 111–202. https://doi.org/10.1080/10408430701707347 (In English)

Kiselev, D. A., Staritsyn, M. V., Senkevich, S. V. et al. (2023) Radially oriented lateral self-polarization in spherulitic lead zirconate titanate thin films. Technical Physics Letters, 49 (11), 45–47. (In English)

Kolosov, V. Yu., Thölén, A. R. (2000) Transmission electron microscopy studies of the specific structure of crystals formed by phase transition in iron oxide amorphous films. Acta Materialia, 48 (8), 1829–1840. https://doi.org/10.1016/S1359-6454(99)00471-1 (In English)

Kolosov, V. Yu., Veretennikov, L. M., Startseva, Yu. B., Schvamm, C. L. (2005) Electron microscopy study of a chalcogenide-based polycrystalline condensate microstructure: The effect of composition and thickness on internal lattice bending. Semiconductors, 39 (8), 955–959. https://doi.org/10.1134/1.2010692 (In English)

Kooi, B. J., De Hosson, J. Th. M. (2004) On the crystallization of thin films composed of $Sb_{3.6}Te$ with Ge for rewritable data storage. Journal of Applied Physics, 95 (9), 4714–4721. https://doi.org/10.1063/1.1690112 (In English)

Lutjes, N. R., Zhou, S., Antoja-Lleonart, J. et al. (2021) Spherulitic and rotational crystal growth of Quartz thin films. Scientific Reports, 11 (1), article 14888. https://doi.org/10.1038/s41598-021-94147-y (In English)

Musterman, E. J., Dierolf, V., Jain, H. (2022) Curved lattices of crystals formed in glass. International Journal of Applied Glass Science, 13 (3), 402–419. https://doi.org/10.1111/ijag.16574 (In English)

Pronin, I. P., Kaptelov, E. Yu., Gol'tsev, A. V., Afanasjev, V. P. (2003) The effect of stresses on self-polarization of thin ferroelectric films. Physics of the Solid State, 45 (9), 1768–1773. https://doi.org/10.1134/1.1611249 (In English)

Pronin, V. P., Dolgintsev, D. M., Osipov, V. V. et al. (2018) The change in the phase state of thin PZT layers in the region of the morphotropic phase boundary obtained by the RF magnetron sputtering with varying target-substrate distance. IOP Conference Series: Materials Science and Engineering, 387, article 012063. https://doi.org/10.1088/1757-899X/387/1/012063 (In English)

Pronin, V. P., Senkevich, S. V., Elshin, A. S. et al. (2023) Spherulitic microstructure of thin PZT films. Physics of Complex Systems, 4 (2), 81–87. https://doi.org/10.33910/2687-153X-2023-4-2-81-87 (In English)

Shtukenberg, A. G., Punin, Yu. O., Gujra,l A., Kahr, B. (2014) Growth actuated bending and twisting of single crystals. Angewandte Chemie International Edition, 53 (3), 672–699. https://doi.org/10.1002/anie.201301223 (In English)

Shtukenberg, A. G., Punin, Yu. O., Gunn, E., Kahr, B. (2012) Spherulites. Chemical Reviews, 112 (3), 1805–1838. https://doi.org/10.1021/cr200297f (In English)

Song, L., Glinsek, S., Defay, E. (2021) Toward low-temperature processing of lead zirconate titanate thin films: Advances, strategies, and applications. Applied Physics Reviews, 8 (4), article 041315. https://doi.org/10.1063/5.0054004 (In English)

Spierings, G. A. C. M., van Zon, J. B. A., Larsen, P. K., Klee, M. (1993) Influence of platinum-based electrodes on the microstructure of sol - gel and MOD prepared lead zirconate titanate films. Integrated Ferroelectrics, 3 (3), 283–292. https://doi.org/10.1080/10584589308216719 (In English)

Staritsyn, M. V., Fedoseev, M. L., Kiselev, D. A. et al. (2023a) Ferroelectric properties of lead zirconate titanate thin films obtained by RF magnetron sputtering near the morphotropic phase boundary. Physics of the Solid State, 65 (2), 290–295. https://doi.org/10.21883/PSS.2023.02.55414.531 (In English)

Staritsyn, M. V., Pronin, V. P., Khinich, I. I. et al. (2023b) Microstructure of spherulitic lead zirconate titanate thin films. Physics of the Solid State, 65 (8), 1312–1318. https://doi.org/10.61011/PSS.2023.08.56577.140 (In English)

Zhigalina, O. M., Khmelenin, D. N., Valieva, Yu. A. et al. (2018) Structural features of PLZT films. Crystallography Reports, 63 (4), 646–655. https://doi.org/10.1134/S1063774518040314 (In English)

Condensed Matter Physics.
Theory of condensed matter

UDC 53.01

EDN POCJRY
https://www.doi.org/10.33910/2687-153X-2024-5-2-67-73

Origin of temperature dependence of bacterial growth rate: Analogy with the viscosity of glass-forming liquids in inorganic materials

C. Pinto ✉[1], K. Shimakawa [2]

[1] East Timor National University, Av. Cidade de Lisboa, Díli, East Timor
[2] Gifu University, 1–1 Yanagido, Gifu 501–1193, Japan

Authors

Carlito Pinto, ORCID: 0000-0002-3086-5772, e-mail: carlito.pinto@untl.edu.tl

Koichi Shimakawa, ORCID: 0000-0002-3862-8579, e-mail: koichi@gifu-u.ac.jp

For citation: Pinto, C., Shimakawa, K. (2024) Origin of temperature dependence of bacterial growth rate: Analogy with the viscosity of glass-forming liquids in inorganic materials. *Physics of Complex Systems*, 5 (2), 67–73. https://www.doi.org/10.33910/2687-153X-2024-5-2-67-73 EDN POCJRY

Received 10 March 2024; reviewed 8 April 2024; accepted 8 April 2024.

Funding: The study did not receive any external funding.

Abstract. Based on a recent suggestion that the bacterial cytoplasm has a property similar to glass-forming liquids, we have proposed a new relation for the temperature dependence of the bacterial growth rate, $k = k_0 \exp[-E_a/k_B(T-T_c)]$ in the lower temperature range, where k_0 is a constant, E_a is the activation energy (eV), k_B is the Boltzmann constant, T is the absolute temperature (K), and T_c is the characteristic (frozen-in) temperature (K), resembling the temperature-dependent fluidity (inverse viscosity) observed in glass-forming liquids in inorganic materials. This monotonic behavior of bacterial growth breaks down at higher temperatures, that is, k decreases rapidly with T. This may be attributed to a rapid increase in the physiological cytoplasmic concentration above the critical temperature T_m. The finding on the temperature-dependent bacterial growth rate is analogous to that observed in glass-forming liquids in nonliving inorganic materials.

Keywords: bacterial growth rate, glass-forming liquid, glass transition, viscosity, free volume

Introduction

The bacterial cytoplasm is a liquid aqueous mixture crowded with macromolecules and organelles (Cossins et al. 2011; Golding, Cox 2006; Munder et al. 2016; Oyama et al. 2019; Perry et al. 2014; Trevors et al. 2013). In the bacterial cytoplasm, most metabolic activity occurs, as does small molecular diffusion. Diffusion within the bacterial cytoplasm is the dominant mechanism of molecular motion and is considered an integral part of bacterial life (Grimaldo et al. 2019; Munder et al. 2016; Perry et al. 2014; Smigiel et al. 2022). The bacterial cytoplasm has a glassy property similar to that of inorganic materials exhibiting glass transition (Lee et al. 2020; Nishizawa et al. 2017; Perry et al. 2014; Takatori, Mandadapu 2020). The study of intracellular glasses is of considerable interest as it can provide insight into the physical and chemical properties of the bacterial cytoplasm, which is a complex and dynamic environment that plays a vital role in cellular processes (Oyama et al. 2019). It is well known that a crucial environmental factor for a microorganism is temperature (Noll et al. 2020).

A recent study (Pinto, Shimakawa 2023) has investigated the temperature dependence of the dynamic bacterial growth rate to describe the bacterial growth rate at a glass transition temperature (low temperature) instead of the commonly used square-temperature-dependent law (Ratkowsky et al. 1983). However, the nonmonotonic behavior observed at high temperatures has not been discussed. In this paper, we propose a model that unifies the dynamics of the bacterial cytoplasm over the entire biokinetic temperature range. It is suggested that the free volume may dominate the overall features of temperature-dependent bacterial growth at low and high temperature.

Glass Dynamics in Bacterial Systems

Overview

Glass dynamics in the bacterial cytoplasm are related to temperature, viscosity, and molecular concentration (Lama et al. 2022; Lee et al. 2020; Nishizawa et al. 2017). The viscosity of the cytoplasm increases with the macromolecular concentration (Grimaldo et al. 2019; Nishizawa et al. 2017), leading to a decrease in the fluidity of metabolic activity at physiological concentrations. The diffusivity of molecules in the bacterial cytoplasm is also strongly related to intermolecular interactions, cell concentration, and free-volume availability (Cossins et al. 2011; Golding, Cox 2006; Oyama et al. 2019; Trevors et al. 2013). Moreover, at physiological concentrations, the diffusivity of molecules is limited owing to a decrease in free volume (Lee et al. 2020; Nishizawa et al. 2017; Ojovan 2008). The free volume of the bacterial cytoplasm decreases with temperature, which leads to vitrification (glass transition) (Pinto, Shimakawa 2023; Micoulaut 2021). The glass transition is a dynamical state change from a liquid to a glassy state that occurs via supercooling (Tanaka, Shimakawa 2021) or increasing the density (Ryabov et al. 2004) in nonliving inorganic materials. The concept of well-known inorganic materials has been applied to living bacteria (Balasubramanian et al. 2016; Berthier et al. 2019; Dauchot, Löwen 2019; Nishizawa et al. 2017; Pinto, Shimakawa 2023).

Recently, the present authors (Pinto, Shimakawa 2023) have proposed a model for the temperature dependence of the bacterial growth rate k (h^{-1}), which fits well at low temperatures:

$$k = k_0 \exp\left(-\frac{E_a}{K_B(T-T_c)}\right), \quad (1)$$

where k_0 is a constant, E_a is the activation energy (eV) for the temperature difference $(T - T_c)$ (Micoulaut 2021; Pinto, Shimakawa 2023), T_c is the characteristic temperature (frozen-in) or glass transition temperature (K), and T is the ambient temperature (K). Note here that E_a is therefore not the same as the so-called activation energy in the Arrehenius plot. Equation (1) is similar to inverse viscosity, which is widely used for inorganic materials (Elliott 1990; Tanaka, Shimakawa 2021; Zallen 1983). There is a similarity between the bacterial growth rate and the fluidity of glass-forming liquids (Dauchot, Löwen 2019; Janssen 2019; Nishizawa et al. 2017; Pinto, Shimakawa 2023). Note that the most popular model was the square-root temperature dependence in which the square root of the growth rate k is given as (Ratkowsky et al. 1982)

$$\sqrt{k} = b(T - T_0)\ , \quad (2)$$

where b is a constant and T_0 is the hypothetical temperature, respectively. The present authors (Pinto, Shimakawa 2023) have suggested that equation (1) has more scientific insight than the square-root model, (equation (2)).

However, bacterial growth decreases at higher temperatures (Ratkowsky et al. 1982; 1983), indicating that the monotonic increase in the growth rate is disrupted. Therefore, the utility of phenomenological models has been discussed (Heitezer et al. 1991), and the following extended square root model (Ratkowsky et al. 1983) has been empirically introduced for the bacterial growth rate over a wide temperature range (Noll et al. 2020):

$$\sqrt{k} = b(T - T_{\min})\{1 - \exp[c(T - T_{\max})]\}, \quad (3)$$

where $T_{\min}$ and $T_{\max}$ are the minimum and maximum temperatures, respectively, b is the regression coefficient of the square root model of the growth rate (mentioned above), and c is an additional parameter that allows the model to fit the data for temperatures above the optimum temperature.

 https://www.doi.org/10.33910/2687-153X-2024-5-2-67-73

Although the fitting of equation (3) to the experimental data for the entire biokinetic temperature range is reasonably good (Heitezer et al. 1991; Noll et al. 2020; Ratkowsky et al. 1983), the model does not provide any physical insight. In our opinion, any model should have scientific basis.

Proposed model

Bacterial growth is highly dependent on the cytoplasm. The cytoplasm of bacterial cells plays a critical role in the survival and growth of the organism (Nishizawa et al. 2017). As already mentioned, the cytoplasm itself depends on the temperature (equation (1)) and is frozen-in at a low temperature. This is called the glass transition of the bacterial cell (Pinto, Shimakawa 2023). Other unique features of the bacterial cytoplasm include crowdedness (Fernandez-de-Cossio-Diaz, Vazques 2018; Lama et al. 2022; Munder et al. 2016; Nishizawa et al. 2017; Perry et al. 2014), with a high concentration of macromolecules occupying a relatively small volume. This type of crowding should have significant effects on the properties of the macromolecules, such as the diffusion rates and interactions with other molecules (Cossins et al. 2011; Grimaldo et al. 2019; Munder et al. 2016). Therefore, an increase in metabolic activity can lead to a decrease in the fluidity of the bacterial cytoplasm and eventually lead to a decrease in the growth rate (Trevors et al. 2013). If a particle is confined by the surrounding molecules, its movement is impeded (Fernandez-de-Cossio-Diaz, Vazques 2018; Yu et al. 2016). A recent report on the concentration dependence of viscosity has shown that viscosity increases with concentration (Nishizawa et al. 2017), indicating that the free volume decreases at physiological concentrations.

Therefore, we suggest that there are two types of freezing-in transitions of the cytoplasm in the bacterial growth process: one is the direct temperature effect (temperature-induced glass transition) (Pinto, Shimakawa 2023), and the other is the concentration-induced phenomena (Nishizawa et al. 2017). Accordingly, the bacterial growth rate k can be expressed by the conditional probability of these two events:

$$k = p_1 p_2 \ , \tag{4}$$

where p_1 is the probability of the freezing-in transition (equation (1)), and p_2 is the probability of the concentration-related freezing-in transition, which should also depend on the temperature, as will be discussed below.

Based on the composition-dependent glassy behavior of the bacterial cytoplasm, which is based on the Doolittle equation (Doolittle 1951), the conditional probability p_2 is assumed to be given as

$$p_2 = exp\left(-\frac{Ac}{c^* - c}\right), \tag{5}$$

where A is a constant, and c and c^* are the concentration and critical concentration of the cytoplasm, respectively. It is assumed here that the number of c obeys the Boltzmann law (Ryabov et al. 2004):

$$c^* = c_0 \exp\left(-\frac{E_\mathrm{b}}{k_\mathrm{B} T_m}\right) \ , \tag{6}$$

$$c = c_0 \exp\left(-\frac{E_\mathrm{b}}{k_\mathrm{B} T}\right) \ , \tag{7}$$

where E_b is the activation energy (eV), and T_m is the critical temperature (K).

Finally, we obtained the following universal equation for the temperature dependence of the bacterial growth rate k over the entire biokinetic temperature range:

$$\ln k = \ln k_0 - \frac{E_a}{k_B (T - T_\mathrm{c})} - \frac{A}{exp\left[-\frac{E_\mathrm{b}}{k_\mathrm{B}}\left(\frac{1}{T_\mathrm{m}} - \frac{1}{T}\right)\right]} \ . \tag{8}$$

Equation (8) consists of two thermodynamic behaviors: at a characteristic temperature T_c at low temperatures, the cytoplasmic movement is frozen-in (glassy state), which can be attributed to a decrease in thermal expansion (loss of free volume). Above T_c, the cytoplasm is in a liquid state and hence has sufficient free volume; hence, the metabolic activity is high, leading to a higher concentration of the cytoplasm. At a critical temperature T_m at high temperatures, the bacterial cytoplasm becomes more

confined, and the molecular mobility slows, leading to a drastic reduction in mobility (or leading to cell death). This effect is not expected if the system has sufficient space. It is of interest to state in confined systems that a glass transition from the liquid state at high temperatures has been reported in nonliving inorganic materials (Ryabov et al. 2001; 2004; Tanaka, Shimakawa 2021; Zallen 1983).

Comparison with the experimental results

The solid circles in Fig. 1 show the experimental results of the logarithmic growth rate k (h^{-1}) against the reciprocal absolute temperature (K^{-1}) for four bacterial species: *Alteromonas* sp., *Aeromonas* sp., *Flavobacterium* sp., and *Moraxella* sp. (Ratkowsky et al. 1983) The solid line is given by equation (8). The logarithmic value of the bacterial growth rate k increases with the temperature up to a certain point, and this monotonic behavior breaks down (nonmonotonic) at higher temperatures. The fitting of equation (8) to the experimental data is good, with $R^2 > 0.9$; the physical parameters are presented in Table 1. The experimental results for other examples, namely, *Vibrio marinus*, *Thermus aquaticus*, *Escherichia coli,* and *Bacillus subtilis*, (Ratkowsky et al. 1983) are shown in Fig. 2. The fitting of equation (8) to the experimental data is also good, with $R^2 > 0.9$ (except for *E. coli* whose $R^2 = 0.689$). The physical parameters are listed in Table 2.

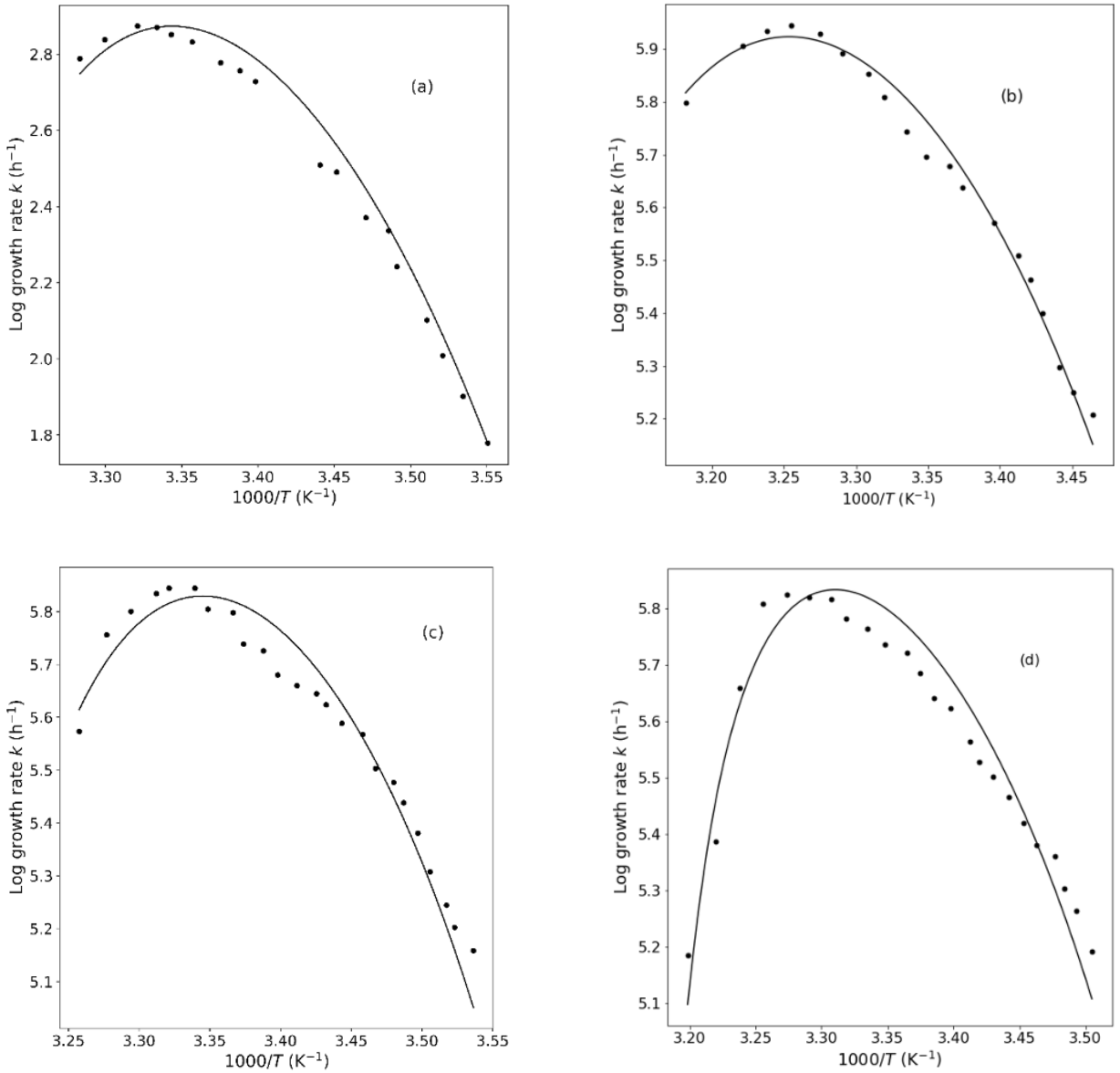

Fig. 1. Fitting of equation (8) to the experimental data (as indicated by the solid line) for a) *Alteromonas* sp., b) *Aeromonas* sp., c) *Flavobacterium* sp., and d) *Moraxella* sp. Experimental data were taken from (Ratkowsky et al. 1983)

 https://www.doi.org/10.33910/2687-153X-2024-5-2-67-73

Table 1. Fitting parameters for Fig. 1

Bacteria	T_c (K)	T_m (K)	E_a (eV)	E_b (eV)	R^2
Alteromonas sp.	240	334	0.025	0.08	0.978
Aeromonas sp.	250	353	0.015	0.079	0.983
Flavobacterium sp.	255	329	0.0086	0.004	0.946
Moraxella sp.	260	319	0.0057	0.0041	0.927

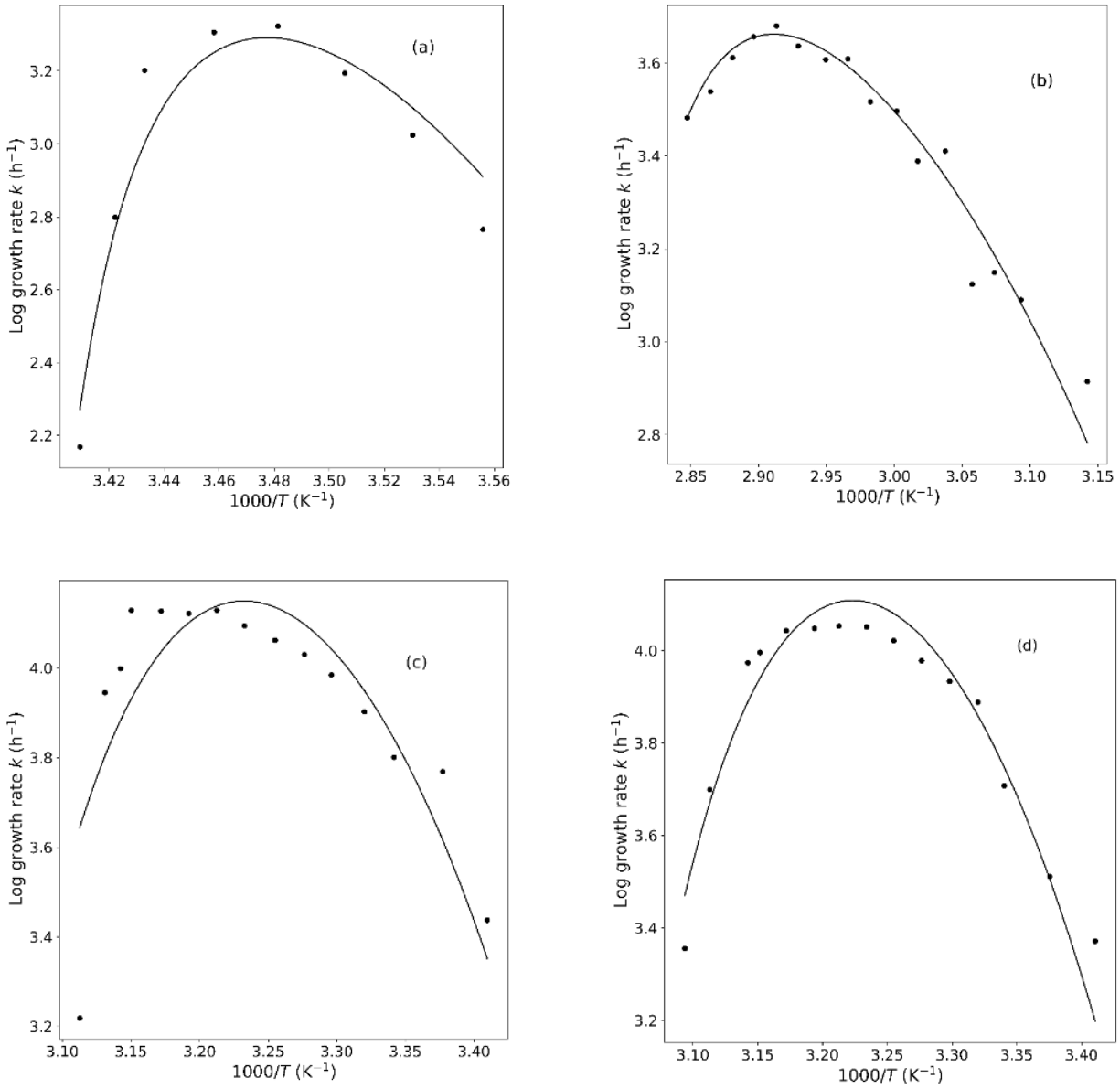

Fig. 2. Fitting of equation (8) to the experimental data (as indicated by the solid line) for a) *V. marinus*, b) *T. aquaticus*, c) *E. coli*, and d) *B. subtilis*. Experimental data were taken from (Ratkowsky et al. 1983)

Table 2. Fitting parameters for Fig. 2

Bacteria	T_c (K)	T_m (K)	E_a (eV)	E_b (eV)	R^2
Vibrio marinus	268	303	0.0048	0.081	0.921
Thermus aquaticus	244	393	0.053	0.05	0.941
Escherichia coli	248	352	0.022	0.056	0.689
Bacillus subtilis	252	351	0.022	0.055	0.919

This type of emergence of the glassy state in bacteria is of interest as bacteria characterized as glass-forming liquids can be vitrified at higher (T_m) and lower (T_c) temperatures. The metabolic activity of the cells ceases below T_c and above T_m (Arcus et al. 2016; Khonsari, Kollmann 2015; Lee et al. 2020). It is of interest to examine whether there is a correlation between T_c and T_m. Fig. 3 shows the correlation between T_c and T_m (Tables 1 and 2). There may be a weak correlation between T_m and T_c; T_m decreases linearly with T_c.

It should be noted that the energies E_a and E_b, as the fitting parameters, seem to be smaller than the inorganic glass-forming liquid. As already stated in the previous section (overview), the bacterial cytoplasm is in a low-temperature liquid state, and therefore thermal reaction-related energy is smaller than that of the popular inorganic glass-forming liquids. It should also be mentioned that the E_a itself is not the so-called activation energy (Micoulaut 2021; Pinto, Shimakawa 2023) (see section overview).

Conclusion

The glass transition can be defined as a state of reduced mobility ('frozen-in'), where the molecules can no longer move freely even in liquid states. We presented a new interpretation for the temperature dependence of the bacterial growth rate over the entire biokinetic temperature range: the bacterial cytoplasm exhibits two types of frozen-in transitions: at low (T_c) and high (T_m) temperatures. T_c is dominated by the free volume gained by thermal expansion, and T_m is dominated by the free volume corresponding to the physiological concentration in the cytoplasm. Below T_c and above T_m, the free volume collapses, inducing nonmonotonic temperature dependence of bacterial growth, which is phenomenologically analogous to that observed in glass-forming liquids in nonliving inorganic materials. It should be noted, however, that the loss of free volume above T_m in bacteria (lived matter) may lead to the death of the cytoplasm, but not in nonliving materials. Dynamics of the living system is very complex, and hence further careful discussion is required.

Conflict of Interest

The authors delare that there is no conflict of interest, either existing or potential.

Author Contributions

Data collection was performed by C. Pinto, and analysis was carried out by C. Pinto and K. Shimakawa. K. Shimakawa provided the information on the glass-forming liquid discussed in solid state physics (K. Shimakawa's field). The first draft of the manuscript was written by C. Pinto, and K. Shimakawa commented on the previous versions of the manuscript. Both authors read and approved the final manuscript.

Acknowledgments

We would like to thank Prof. T. Nakagawa from the Department of Life Sciences, Gifu University, for engaging in useful discussions on bacterial cells. We also thank the Japan International Cooperation Agency (JICA) for their technical and financial support.

References

Arcus, V. L., Prentice, E. J., Hobbs, J. K. et al. (2016) On the temperature dependence of enzyme-catalyze rates. *Biochemistry*, 55 (12), 1681–1688. https://doi.org/10.1021/acs.biochem.5b01094 (In English)

Balasubramanian, S., Devi, A., Singh, K. et al. (2016) Application of glass transition in food processing. *Critical Reviews in Food Science and Nutrition*, 56 (6), 919–936. https://doi.org/10.1080/10408398.2012.734343 (In English)

Berthier, L., Flenner, E., Szamel, G. (2019) Glassy dynamics in dense systems of active particles. *The Journal of Chemical Physics*, 150 (20), article 200901. https://doi.org/https://doi.org/10.1063/1.5093240 (In English)

Cossins, B., Jacobson, M. P., Guallar, V. (2011) A new view of the bacterial cytosol environment. *PLOS Computer Biology*, 7 (6), article e1002066. https://doi.org/10.1371/journal.pcbi.1002066 (In English)

Dauchot, O., Löwen, H. (2019) Chemical physics of active matter. *The Journal of Chemical Physics*, 151 (11), article 114901. https://doi.org/10.1063/1.5125902 (In English)

Fernandez-de-Cossio-Diaz, J. F., Vazquez, A. (2018) A physical model of cell metabolism. *Scientific Reports*, 8 (1), article 8349. https://doi.org/10.1038/s41598-018-26724-7 (In English)
Doolittle, A. K. (1951) Studies in Newtonian Flow. II. The dependence of the viscosity of liquids on free-space. *Journal of Applied Physics*, 22 (12), 1471–1475. https://doi.org/10.1063/1.1699894 (In English)
Elliott, S. R. (1990) *Physics of amorphous materials.* 2nd ed. New York: Wiley Publ., 481 p. (In English)
Golding, I., Cox, E. C. (2006) Physical nature of bacterial cytoplasm. *Physical Review Letters*, 96 (9), article 098102. https://doi.org/10.1103/PhysRevLett.96.098102 (In English)
Grimaldo, M., Lopez, H., Beck, C. et al. (2019) Protein short-time diffusion in a naturally crowded environment. *The Journal of Physical Chemistry Letters*, 10 (8), 1709–1715. https://doi.org/10.1021/acs.jpclett.9b00345 (In English)
Heitezer, H., Peter, H., Kohler, E., Hamer, G. (1991) Utility of phenomenological models for describing temperature dependence of bacterial growth. *Applied and Environmental Biology*, 57 (9), 2656–2665. https://doi.org/10.1128/aem.57.9.2656-2665.1991 (In English)
Janssen, L. M. C. (2019) Active glasses. *Journal of Physics: Condensed Matter*, 31, article 503002. https://doi.org/10.1088/1361-648X/ab3e90 (In English)
Khonsari, A. S., Kollmann, M. (2015) Perception and regulatory principles of microbial growth control. *PLoS ONE*, 10 (5), article e0126244. https://doi.org/10.1371/journal.pone.0126244 (In English)
Lama, H., Yamamoto, M. J., Furuta, Y. et al. (2022) *Emergence of bacterial glass*. [Online]. Available at: https://arxiv.org/abs/2205.10436 (accessed 09.11.2023). (In English)
Lee, K., Shoda, M., Kawai, K., Koseki, S. (2020) Relationship between glass transition temperature, and desiccation and heat tolerance in *Salmonella enterica*. *PLoS ONE*, 15 (5), article e0233638. https://doi.org/10.1371%2Fjournal.pone.0233638 (In English)
Micoulaut, M. (2021) *The world scientific reference of amorphous materials: Structure, properties, modeling and applications of amorphous chalcogenides*. New Jersey: World Scientific Publ., 1548 p. (In English)
Munder, M. C., Midtvedt, D., Franzmann, T. et al. (2016) A pH-driven transition of the cytoplasm from a fluid-to a solid-like state promotes entry into dormancy. *eLife*, 5, article e09347. https://doi.org/10.7554/eLife.09347 (In English)
Nishizawa, K., Fujiwara, K., Ikenaga, M., Nakajo, N. (2017) Universal glass-forming behavior of *in vitro* and *living* cytoplasm. *Scientific Report*, 7 (1), article 15143. https://doi.org/10.1038/s41598-017-14883-y (In English)
Noll, P., Lilge, L, Hausmann, R., Henkel, M. (2020) Modeling and exploiting microbial temperature response. *Processes*, 8 (1), article 121. https://doi.org/10.3390/pr8010121 (In English)
Ojovan, M. I. (2008) Viscosity and glass transition in amorphous oxides. *Advanced in Condensed Physics*, 2008, article 817829. https://doi.org/10.1155/2008/817829 (In English)
Oyama, N., Kawasaki, T., Mizuno, K., Ikeda, A. (2019) Glassy dynamics of a model of bacterial cytoplasm with metabolic activities. *Physical Review Research*, 1 (3), article 032038(R). https://doi.org/10.1103/PhysRevResearch.1.032038 (In English)
Perry, B. R., Surovtsev, I. V., Cabeen, M. T. et al. (2014) The bacterial cytoplasm has glass-like properties and is fluidized by metabolic activity. *Cell*, 156 (1–2), 183–194. https://doi.org/10.1016/j.cell.2013.11.028 (In English)
Pinto, C., Shimakawa, K. (2023) Glassy dynamics in bacterial growth rate temperature dependence. *AIP Advances*, 13 (2), article 025126. https://doi.org/10.1063/5.0139055 (In English)
Ratkowsky, D. A., Lowry, R. K., McMeekin, T. A. et al. (1983) Model for bacterial culture growth rate throughout the entire biokinetic temperature range. *Journal of Bacteriology*, 154 (3), 1222–1226. https://doi.org/10.1128/jb.154.3.1222-1226.1983 (In English)
Ratkowsky, D. A., Olley, J., McMeekin, T. A., Ball, A. (1982) Relationship between temperature and growth rate of bacterial cultures. *Journal of Bacteriology*, 149 (1), 1–5. https://doi.org/10.1128/jb.149.1.1-5.1982 (In English)
Ryabov, Ya. E., Gutina, A., Arkhipov, V., Feldman, Yu. (2001) Dielectric relaxation of water absorbed in porous glass. *The Journal of Physical Chemistry B*, 105 (9), 1845–1850. https://doi.org/10.1021/jp0033061 (In English)
Ryabov, Ya. E., Puzenko, A., Feldman, Yu. (2004) Nonmonotonic relaxation kinetics of confined systems. *Physical Review B*, 69 (1), article 014204. https://doi.org/10.1103/PhysRevB.69.014204 (In English)
Smigiel, W. M., Mantovanelli, L., Linnik, D. et al. (2022) Protein diffusion in *Escherichia coli* cytoplasm scales with the mass of the complexes and is location dependent. *Science Advances*, 8 (32), article eabo5387. https://doi.org/10.1126/sciadv.abo5387 (In English)
Takatori, S. C., Mandadapu, K. K. (2020) *Motility-induced buckling and glassy dynamics regulate 3D transitions of bacterial monolayers*. [Online]. Available at: https://arxiv.org/abs/2003.05618 (accessed 12.03.2024). (In English)
Tanaka, K., Shimakawa, K. (2021) *Amorphous Chalcogenide Semiconductors and Related Materials.* New York: Springer Publ., 300 p. (In English)
Trevors, J. T., van Elsas, D. J., Bej, A. K. (2013) The molecularly crowded cytoplasm of bacterial cells: Dividing cells contrasted with viable but non-culturable (VBNC) bacterial cells. *Current Issues in Molecular Biology*, 15, 1–6. https://doi.org/10.21775/cimb.015.001 (In English)
Yu, I., Mori, T., Ando, T. et al. (2016) Biomolecular interactions modulate macromolecular structure and dynamics in atomistic model of a bacterial cytoplasm. *eLife*, 5 (1), article 19274. https://doi.org/10.7554/eLife.19274 (In English)
Zallen, R. (1983) *The physics of amorphous solids*. New York: John Wiley and Sons Publ., 304 p. (In English)

Theoretical Physics.
Physics of atoms and molecules

UDC 539.1

EDN IWQVHR
https://www.doi.org/10.33910/2687-153X-2024-5-2-74-82

Probability currents in inelastic atomic collision studies

I. G. Stepanov [✉1], A. K. Belyaev [1]

[1] Herzen State Pedagogical University of Russia, 48 Moika Emb., Saint Petersburg 191186, Russia

Authors

Ilya G. Stepanov, ORCID: 0009-0008-4476-2548, e-mail: i.stepanov@herzen.edu.ru

Andrey K. Belyaev, ORCID: 0000-0001-8834-1456, e-mail: belyaev@herzen.spb.ru

For citation: Stepanov, I. G., Belyaev, A. K. (2024) Probability currents in inelastic atomic collision studies. *Physics of Complex Systems*, 5 (2), 74–82. https://www.doi.org/10.33910/2687-153X-2024-5-2-74-82 EDN IWQVHR

Received 2 April 2024; reviewed 19 April 2024; accepted 19 April 2024.

Funding: The authors gratefully acknowledge support from the Russian Science Foundation, Project No. 22-23-01181.

Abstract. The rigorous probability current method within the quantum collision theory is tested in detail on the Tully A and B models for a single traverse of nonadiabatic regions during atomic collisions. Calculations are performed in a diabatic representation by numerical integration of the coupled channel equations for nuclear radial wave functions. The results of precise quantum calculations are compared with those predicted by the Landau–Zener model for the same electronic structures. It is established that the probability current method is an efficient tool for investigations of inelastic atomic collision processes.

Keywords: atomic collisions, probability current, Tully models, transition probability, Landau–Zener model, diabatic representation

Introduction

Inelastic processes in low-energy atomic collisions are important for modelling plasma and gas medium, for example, stellar photospheres. Experimental studies are difficult to conduct in order to obtain the information needed, and therefore, theoretical calculations become the main source of data. For this reason, theoretical methods used should be reliable and efficient for practical implementation. The present study tests different theoretical approaches to investigations of inelastic transitions in atomic collisions, in particular the probability current method and the Landau–Zener model.

There are different theoretical methods for studying atomic collisions, for example, the approach based on the Faddeev equations (Faddeev 1961) and the hyperspherical adiabatic approach (Lin 1995), to mention a few. Nevertheless, the most widely used approach is the Born–Oppenheimer one (Born, Oppenheimer 1927), which implies the separation of electronic and nuclear motions. Electronic structure calculations provide molecular potentials and non-adiabatic couplings. This information enters the coupled channel equations for nuclear dynamics. The present paper deals with the nuclear dynamics part. It should be mentioned that in addition to strict quantum studies, model approaches are widely used as well, for example, the Landau–Zener model (Landau 1932; Zener 1932). In this paper we test the rigorous probability current method for different cases of non-adiabatic regions and compare its results to the Landau–Zener model ones.

Atomic units (a. u.) are used throughout the paper unless stated otherwise.

Collision theory in brief

The rigorous quantum atomic collision theory is usually based on the stationary Schrödinger equation for a molecular system of colliding atoms:

$$\left(\hat{H}_e + \hat{T}_n\right)\Psi^{tot} = \mathrm{E}\Psi^{tot}, \tag{1}$$

where $\hat{H}_e$ stands for the fixed-nuclei electronic Hamiltonian which consists of the electron kinetic energy operator and the operators of the following interactions: electron–nucleus, electron–electron and nucleus–nucleus. $\hat{T}_n$ is the kinetic energy operator for the nuclei. The total wave function of the system (quasi-molecule) is taken as a superposition of partial waves:

$$\Psi^{tot} = \sum_{J,M} \Psi_{J,M}\,, \tag{2}$$

where J is a quantum number of the total molecular angular momentum, and M is a quantum number of its projection. Each partial wave is a solution of equation (1). The first step of the Born–Oppenheimer approach consists of calculations of the eigenfunctions and eigenvalues of the fixed-nuclei electronic Hamiltonian. The non-adiabatic nuclear dynamics is treated during the second step by different methods, strict or model ones, based on the information obtained in the first step.

Strict quantum approach

In strict quantum approaches, accurate eigenfunctions and eigenvalues of the electronic Hamiltonian ϕ_j and $U_j(R)$ are usually calculated by means of *ab initio* methods for each partial wave providing adiabatic potential energies and a number of non-adiabatic couplings for a set of molecular states. Every total (electronic and nuclear) partial wave function is then expanded on the electronic wave functions ϕ_j as follows:

$$\Psi_{J,M}(\boldsymbol{r},\boldsymbol{R}) = \phi_j(\boldsymbol{r},\boldsymbol{R})Y_{J0}\frac{F_j(R)}{R}, \tag{3}$$

where j is an index that enumerates the electronic molecular state, $F_j(R)$ is a radial and Y_{j0}, an angular nuclear wave function. The sigma molecular states are treated here as an example. In the adiabatic representation, the radial wave functions obey the coupled channel equations:

$$\left(-\frac{1}{2\mu}\frac{d^2}{dR^2} + U_j^{eff}(R) - E^{tot}\right)F_j(R) = \frac{1}{\mu}\sum_{k,k\neq j}\left\langle\phi_j\left|\frac{\partial}{\partial R}\right|\phi_k\right\rangle\frac{dF_k}{dR} + \frac{1}{2\mu}\sum_{k,k\neq j}\left\langle\phi_j\left|\frac{\partial^2}{\partial R^2}\right|\phi_k\right\rangle\frac{dF_k}{dR}, \tag{4}$$

E^{tot} being the total collision energy, μ — the reduced mass of the quasi-molecule, U_j^{eff} — the effective potential energy of the channel j and $\left\langle\phi_i\left|\frac{\partial}{\partial R}\right|\phi_k\right\rangle$ — radial non-adiabatic couplings. It is worth noting that equations (4) and (5) are justified only for channels belonging to the same symmetry.

The set of coupled channel equations in a diabatic representation reads:

$$\left(-\frac{1}{2\mu}\frac{d^2}{dR^2} + V_{jj}^{eff}(R) - E^{tot}\right)F_j(R) = \sum_{k,k\neq j} V_{jk}F_k\,, \tag{5}$$

V being a matrix of the electronic Hamiltonian in a diabatic representation.

In order to solve the set of coupled equations, one needs to put boundary conditions. Generally, boundary conditions for nuclear dynamics are set at $R \to 0$:

$$\Psi_j \to 0. \tag{6}$$

In the asymptotic region, at $R \to \infty$:

$$\Psi_j = k_j^{-\frac{1}{2}}\left(a_j^- \exp\left(-ik_jR\right) + a_j^+ \exp\left(ik_jR\right)\right), \tag{7}$$

where k_j is a wave number of a corresponding state, and $a_j^{\pm}$ — the incoming and outgoing amplitudes. When the radial functions are computed, one needs to calculate transition probabilities. This can be done using the S-matrix method (Grosser et al. 1999) or the probability current method (Belyaev, Grosser 1996). Both methods are rigorous and based on the same wave functions, but the S-matrix method yields only inelastic state-to-state transition probabilities after a collision, while the probability current method provides probabilities during the collision for the whole interval of the internuclear distance treated.

To calculate the probability currents from the radial functions, one can use the following equations (Belyaev, Grosser 1996):

$$F_j^{\pm} = \sqrt{k_j}F_j \mp \frac{i}{\sqrt{k_j}}\frac{dF_j}{dR}, \tag{8}$$

$$\tau_j^{\pm} = \left|F_j^{\pm}\right|^2; \tag{9}$$

the $\tau_j^{\pm}$ physical implications are ambiguous in this case, but the difference $\tau_j^+ - \tau_j^-$ gives exactly the total current in the channel j

$$P_j = \tau_j^+ - \tau_j^-. \tag{10}$$

Approaches based on the Landau–Zener model

Let us assume that the electronic structure is computed and all data needed for studying nuclear dynamics are known. One can then estimate transition probabilities using the surface hopping or branching probability current models (Belyaev 2013).

In the asymptotic region, when the internuclear distance R goes to infinity, the probability currents are defined as follows:

$$\tau_j^{\pm} = \left|a_j^{\pm}\right|^2. \tag{11}$$

The currents are a function of the internuclear distance R. The incoming current $\tau^-(R)$ starts in the initial channel i $\left(\tau_j^- = \begin{cases}1, j = i\\ 0, j \neq i\end{cases}\right)$ and proceeds elastically till the nearest non-adiabatic region, where it can hop to another molecular state or splits into two parts according to the non-adiabatic transition probability. It keeps moving to the next non-adiabatic region and so on until it reaches a classical turning point. Then it changes the direction to the opposite and propagates as outgoing current $\tau_j^+(R)$ until it goes away into the asymptotic region. Current evolution can be approached deterministically or stochastically.

In either approaches the Landau–Zener transition probability determines the current in the non-adiabatic region. The Landau–Zener original formula is determined in the diabatic representation as follows:

$$P_{ij} = \exp\left(-\frac{2\pi V_{ij}^2}{\left|\frac{dV_{ii}}{dx} - \frac{dV_{jj}}{dx}\right|\dot{x}}\right), \tag{12}$$

$$\dot{x} = \sqrt{\frac{2(E^{tot} - V_{jj})}{\mu}}. \tag{12.1}$$

 https://www.doi.org/10.33910/2687-153X-2024-5-2-74-82

The Landau–Zener formula can be modified for the adiabatic representation (Belyaev, Lebedev 2011):

$$P_{ij} = \exp\left(-\frac{\xi_{\mathrm{LZ}}}{v}\right);\ \xi_{LZ} = \frac{\pi}{2}\sqrt{\frac{Z^3}{Z''}}\ (\text{at } R = R_c), \tag{13}$$

at the local minimum of the adiabatic splitting $Z = U_i - U_j$.

Branching probability currents

An initial current in a non-adiabatic region is split into two currents according to the Landau–Zener transition probability:

$$\tau_i \to \tau_j' + \tau_i', \tag{14.1}$$

$$\tau_j' = P_{ij}^{LZ}, \tau_i' = 1 - P_{ij}^{LZ}. \tag{14.2}$$

Every split current evolves in its molecular state until reaching the next non-adiabatic region and splits again. After all currents return to the asymptotic region, the sum of currents corresponding to the same channel results in the final transition probability.

Hopping probability currents

Another possible propagation of the probability current is treated by the hopping probability method. In this case the current reaches a non-adiabatic region, and a random number between zero and unity is generated. If the generated number is greater than the Landau–Zener transition probability, then the current remains in the initial molecular state, otherwise it hops into another state. A reasonable number (N) of initial currents populates the same channel. After the simulation, a certain number (N_f) of currents populates each of the studied channels. The resulting transition probability is determined as such:

$$P_{if} = \frac{N_f}{N}. \tag{15}$$

Models

In this paper we use the model problems proposed by Tully (Tully 1990) for testing the probability current method. The two aforementioned model problems defined by Tully in a diabatic representation (names and corresponding letters from (Tully 1990) were carried over as well to avoid confusion) are used in the present work:

Model A 'Simple avoided crossing':

$$\begin{cases} V_{11} = -V_{22} = \begin{matrix} A\,(1 - \exp(-Bx)), x > 0 \\ -A\,(1 - \exp(Bx)), x < 0 \end{matrix} \\ V_{12} = V_{21} = C\exp(-Dx^2)\,. \end{cases} \tag{16}$$

Model B 'Dual avoided crossing':

$$\begin{cases} V_{11} = 0 \\ V_{22} = -A\,exp(-Bx^2) + E_0 \\ V_{12} = V_{21} = C\exp(-Dx^2)\,. \end{cases} \tag{17}$$

Since there is no potential barrier like in real molecules, these models allow us to see how probabilities behave when passing the non-adiabatic region once. Thus, boundary conditions should be slightly adapted for this case $x \to \pm\infty$:

$$\Psi_j = k_j^{-\frac{1}{2}}\left(a_j^- \exp\left(-ik_j x\right) + a_j^+ \exp\left(ik_j x\right)\right). \tag{18}$$

Since the incoming current does not change the direction, only one of these terms, τ^+ and τ^-, in equation (8) is non-zero and completely defines the probability. Thus, one of the amplitudes a_j^+ or a_j^- is equal to zero, and the probability current is determined by the single term in equation (18).

Results

Model A. Simple avoided crossing

In the present work the following parameters were used for the model A: $A = 0.011$, $B = 1.6$, $C = 0.005$ and $D = 1.0$. The diabatic potential energies and off-diagonal matrix elements are depicted in Fig. 1 by solid lines and a dashed line, respectively. The blue solid line is the potential of the first diabatic channel which is the initial channel. The green solid line is the potential of the second diabatic channel. The crossing of the diabatic potentials is clearly seen. The examples of the calculated wave functions are shown in Fig. 2 for the collision energy equals 0.38 *eV* for the transition from state 1 to state 2. It is seen that the wave functions are highly oscillating functions with different amplitudes before and after a collision, which makes the transition mechanism obscure.

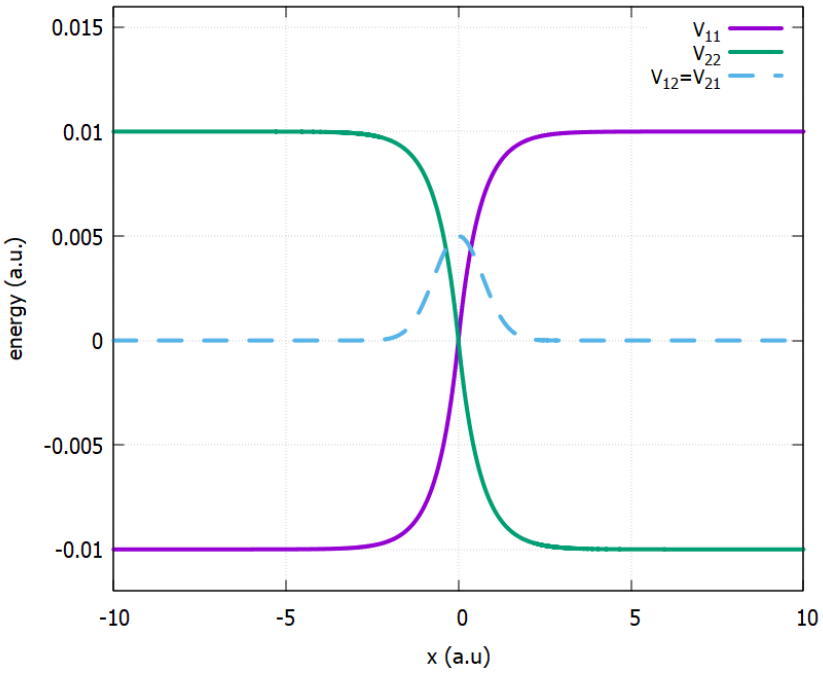

Fig. 1. Tully model 'A', parameter values: $A = 0.011$, $B = 1.6$, $C = 0.005$ and $D = 1.0$

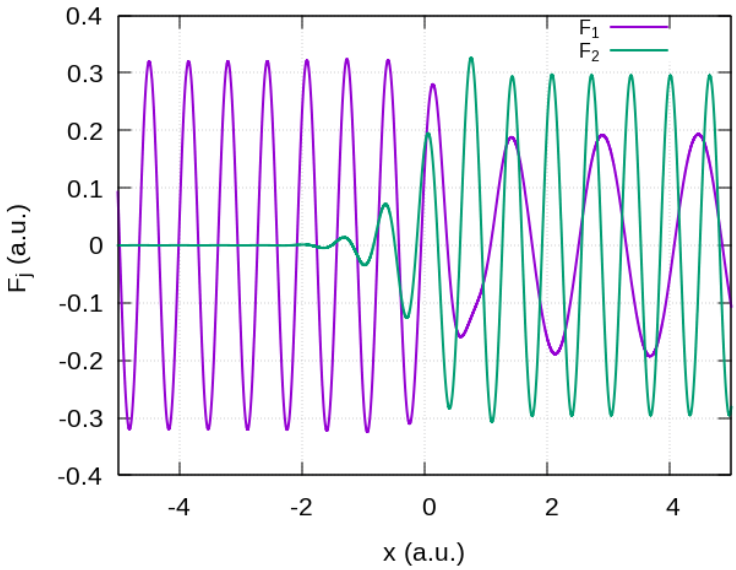

Fig. 2. Computed wave functions for potentials depicted in Fig. 1, total collision energy $E^{tot} = 0.014$ a.u.

https://www.doi.org/10.33910/2687-153X-2024-5-2-74-82

Fig. 3 shows the probability currents as a function of the position x measured from the center of the non-adiabatic region. It is clearly seen where the transition occurs and what the transition probability values are. Note that in a diabatic representation, the calculated probabilities correspond to the ones in the initial state, so the probabilities of a transit from one adiabatic molecular state into another state are presented by the differences $\boldsymbol{P_{if}^{ad} = 1 - P_{if}^{di}}$.

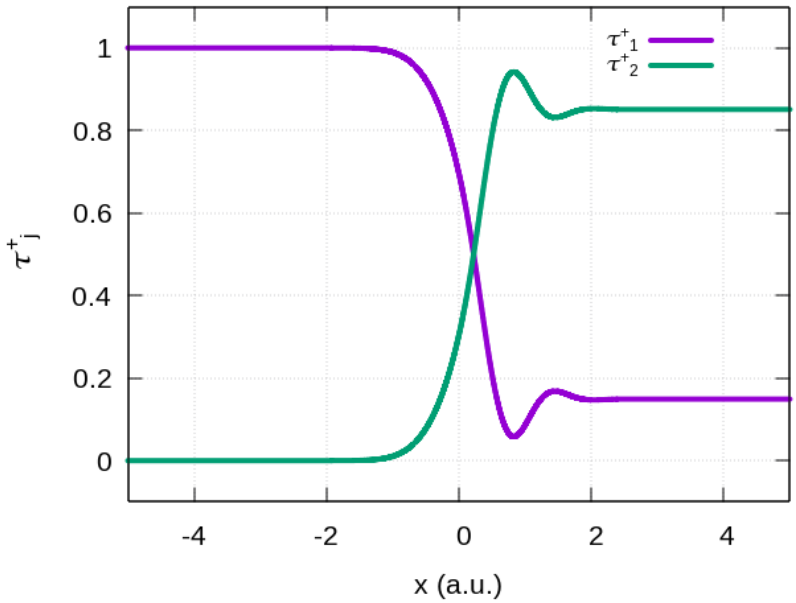

Fig. 3. Probability currents extracted from the wave functions depicted in Fig. 2

Model B. Dual avoided crossing

For the second model B, the following parameters are taken: A = 0.1, B = 0.28, C = 0.015, D = 0.06 and E_0 = 0.05. In this case the diabatic potentials and off-diagonal matrix elements have the form plotted in Fig. 4. The potential energy of the initial channel is again represented by a blue solid line in Fig. 4. This model presents the case of two overlapping non-adiabatic regions.

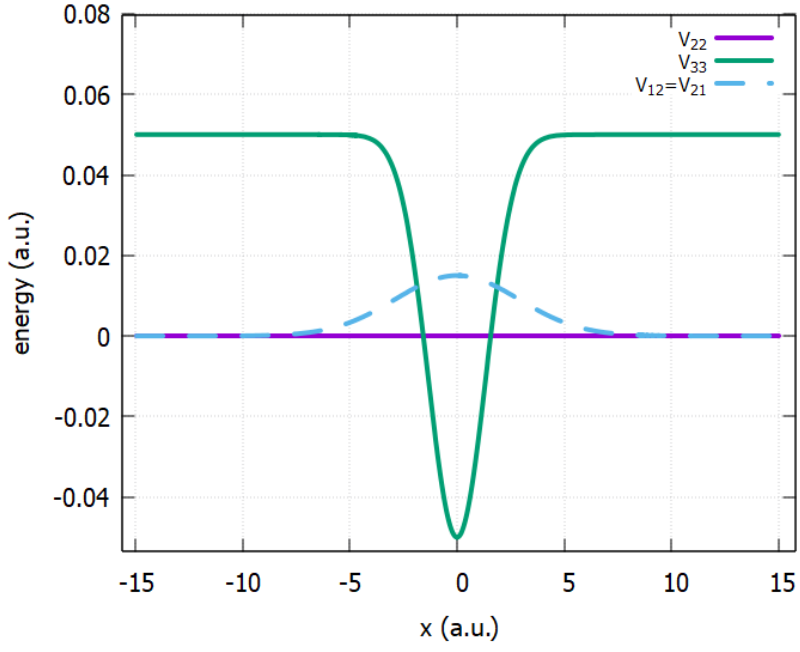

Fig. 4. Tully model 'B', parameter values: A = 0.1, B = 0.28, C = 0.015, D = 0.06 and E_0 = 0.05

Examples of the calculated wave functions are shown in Fig. 5. It shows that the wave functions are more complicated than for model A, and it is not quite clear how transitions occur in this case. The transition mechanism can be better understood if one calculates the probability currents, see Fig. 6. It is clear that the incoming probability current populates the upper molecular state; then the main part of the current transfers into another molecular state, and finally the current passes the second non-adiabatic region and splits between two molecular states exhibiting interference and convergence.

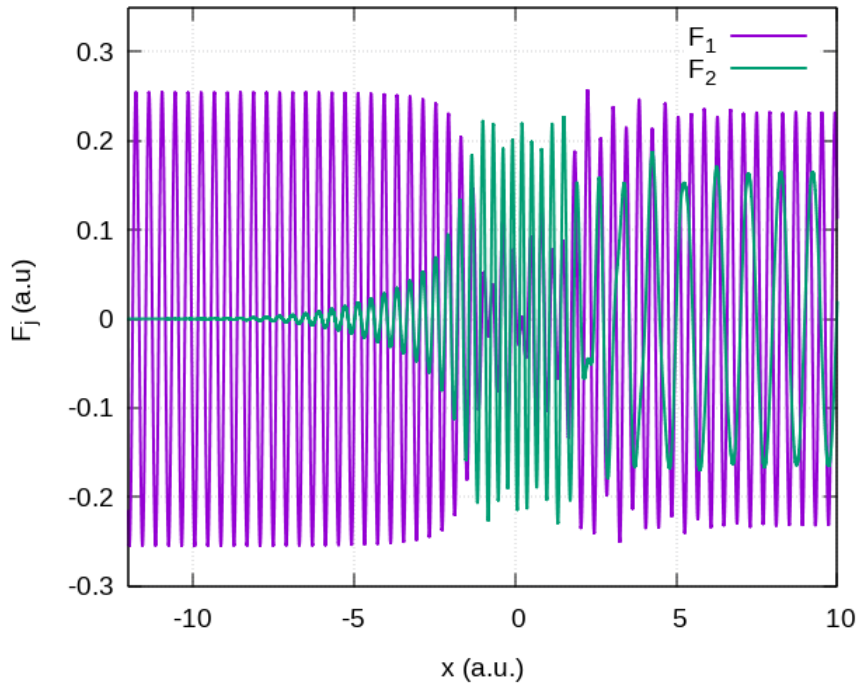

Fig. 5. Computed wave functions for potentials depicted in Fig. 4, total collision energy E^{tot} = 0.06 a.u.

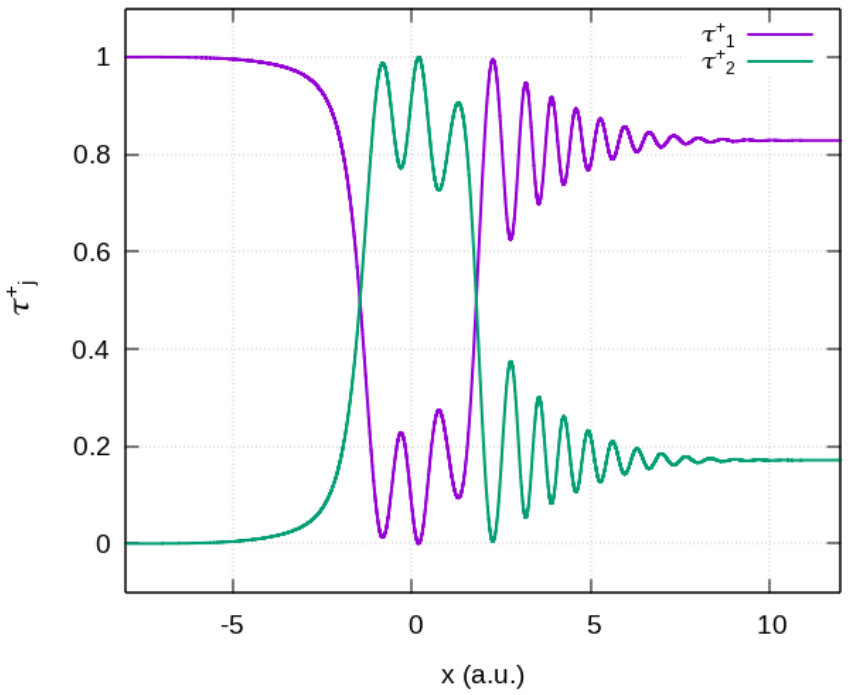

Fig. 6. Probability currents extracted from wave functions depicted in Fig. 5

https://www.doi.org/10.33910/2687-153X-2024-5-2-74-82

The results of calculating the probability currents can be compared with the Landau–Zener estimates. Equations (12) and (13) indicate that the usual Landau–Zener formulas do not include phases, while the currents take phases into account automatically, so the transition probability method provides more information than the Landau–Zener model. Fig. 7 shows the transition probabilities obtained by the two methods as a function of the total energy. It is seen that the Landau–Zener model does not reproduce oscillations, while the probability currents method does. It is seen that the Landau–Zener model provides transition probabilities in reasonable agreement with the results of the strict calculation by the transition current method.

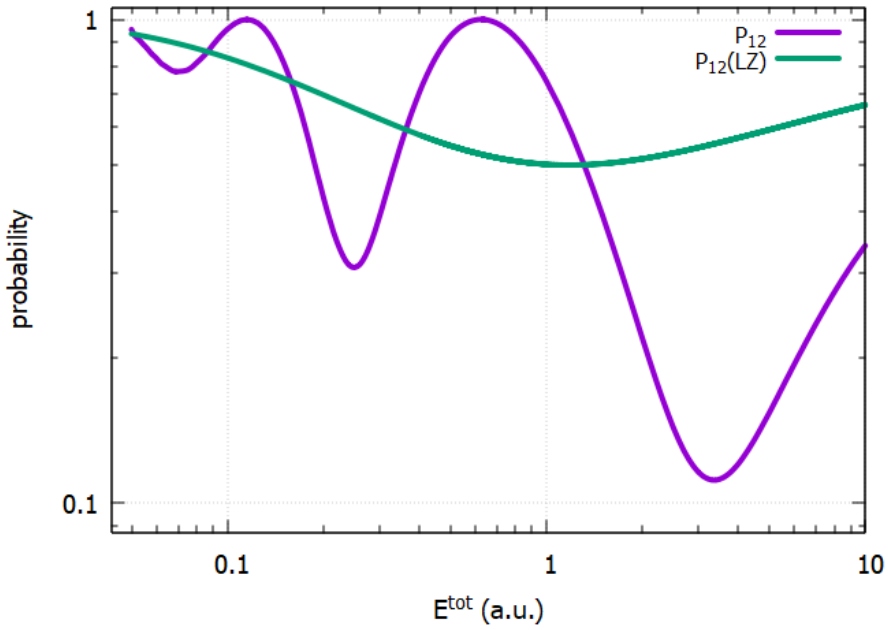

Fig. 7. Transition probability as a function of the total energy (Tully model B)

Conclusions

A computer program is derived in the present work in order to study inelastic atomic collisions using the probability current method based on accurate quantum coupled channel equation solutions. It is found that the probability current method allows one to calculate the transition probabilities with the same accuracy as the S-matrix method, but the former gives insight on the mechanism of the process, while the latter provides only final transition probabilities. Thus, the transition probability method is an effective tool in studying inelastic state-to-state transitions.

Conflict of Interest

The authors declare that there is no conflict of interest, either existing or potential.

Author Contributions

The authors have made an equal contribution to the paper.

Acknowledgements

The authors are grateful to Dr. Svetlana A. Yakovleva and Yaroslav V. Voronov for fruitful discussions.

References

Belyaev, A. K. (2013) Model approach for low-energy inelastic atomic collisions and application to Al+H and $Al^+ + H^-$. *Physical Review A*, 88 (5), article 052704. https://doi.org/10.1103/PhysRevA.88.052704 (In English)

Belyaev, A. K., Grosser, J. (1996) Theoretical treatment of inelastic thermal $He^+ + Hg$ collisions. *Journal of Physics B: Atomic, Molecular and Optical Physics*, 29 (23), article 5843. https://doi.org/10.1088/0953-4075/29/23/024 (In English)

Belyaev, A. K., Lebedev, O. V. (2011) Nonadiabatic nuclear dynamics of atomic collisions based on branching classical trajectories. *Physical Review A*, 84 (1), article 014701. https://doi.org/10.1103/PhysRevA.84.014701 (In English)

Born, M., Oppenheimer, R. (1927) Zur quantentheorie der molekeln [On the quantum theory of molecules]. *Annalen der Physik*, 389 (20), 216–246. https://doi.org/10.1002/andp.19273892002 (In German)

Faddeev, L. D. (1961) Scattering theory for a three-particle system. *Soviet Journal of Experimental and Theoretical Physics*, 12 (5), 1014–1019. (In English)

Grosser, J., Menzel, T., Belyaev, A. K. (1999) Approach to electron translation in low-energy atomic collisions. *Physical Review A*, 59 (2), article 1309. https://doi.org/10.1103/PhysRevA.59.1309 (In English)

Landau, L. (1932) Zur Theorie der Energieubertragung [On the theory of energy transfer]. *Physikalische Zeitschrift der Sowjetunion*, 1 (2), 46–51. (In German)

Lin, C. D. (1995) Hyperspherical coordinate approach to atomic and other Coulombic three-body systems. *Physics Reports*, 257 (1), 1–83. https://doi.org/10.1016/0370-1573(94)00094-J (In English)

Tully, J. C. (1990) Molecular dynamics with electronic transitions. *The Journal of Chemical Physics*, 93 (2), 1061–1071. https://doi.org/10.1063/1.459170 (In English)

Zener, C. (1932) Non-adiabatic crossing of energy levels. *Proceedings of the Royal Society A. Mathematical, Physical and Engineering Sciences*, 137 (833), 696–702. https://doi.org/10.1098/rspa.1932.0165 (In English)

Theoretical Physics. Cosmology

UDC 524.8

EDN HFGXJA
https://www.doi.org/10.33910/2687-153X-2024-5-2-83-90

Does a primary hair have an impact on the naked singularity formation in hairy Vaidya spacetime?

V. D. Vertogradov [✉1,2]

[1] Herzen State Pedagogical University of Russia, 48 Moika Emb., Saint Petersburg 191186, Russia
[2] SPb branch of SAO RAS, 65 Pulkovskoe Highway, Saint Petersburg 196140, Russia

Authors

Vitalii D. Vertogradov, ORCID: 0000-0002-5096-7696, e-mail: vdvertogradov@gmail.com

For citation: Vertogradov, V. D. (2024) Does a primary hair have an impact on the naked singularity formation in hairy Vaidya spacetime? *Physics of Complex Systems*, 5 (2), 83–90. https://www.doi.org/10.33910/2687-153X-2024-5-2-83-90 EDN HFGXJA

Received 8 April 2024; reviewed 22 April 2024; accepted 22 April 2024.

Funding: The study did not receive any external funding.

Abstract. We consider the gravitational collapse of Vaidya spacetime, which has been obtained using the gravitational decoupling method. In this paper, we are interested in whether a primary hair has any impact on the endstate of the gravitational collapse. We also prove that the coupling constant has an influence on the naked singularity formation. The strength of the central singularity has also been investigated, and we show that the naked singularity is gravitationally strong. However, this model does not violate the cosmic censorship conjecture because in the case of the naked singularity formation the weak energy condition is violated.

Keywords: black hole, naked singularity, gravitational collapse, gravitational decoupling, strength of singularity

Introduction

When a star exhausts all its fuel, it undergoes continuous gravitational collapse. Oppenheimer and Snyder (Oppenheimer, Snyder 1939) were one of the first who considered the model of homogeneous dust collapse leading to a black hole formation. According to the cosmic censorship conjecture [CCC], a singularity must be covered by the horizon. However, if one considers the gravitational collapse of inhomogeneous dust (Jhingan et al. 1996; Singh, Joshi 1996), then the result might be a singularity that is not covered by the apparent horizon — so-called naked singularity. Thorough investigation of different scenarios of the gravitational collapse showed that under physically relevant conditions, a naked singularity might form during this process (Dey et al. 2022; Goncalves, Jhingan 2001; Harko 2003; Joshi 2007; Joshi, Malafarina 2011; Mosani et al. 2022; Naidu al. 2020).

Papapetrou (Papapetrou 1985) showed that the Vaidya spacetime (Vaidya 1951) is an example of the CCC violation. The radiating Schwarzschild spacetime, or Vaidya metric, is widely used in many astrophysical applications with strong gravitational fields. The spacetime around a black hole should be dynamical due to the processes of emission and absorption, and the Vaidya spacetime is one of the simplest examples of a dynamical spacetime. It is used to describe the exterior geometry of radiating stars (Santos 1985). The backreaction of the accreting matter leads to the Vaidya spacetime in spherically-symmetric case (Babichev et al. 2012). The question about the dynamical shadow formation in Vaidya and charged Vaidya spacetimes is discussed in (Heydarzade, Vertogradov 2023; Koga et al. 2022; Solanki,

Perlick 2022). The horizon structure and entropy of this solution are investigated for an empty background in (Nielsen 2014; Nielsen, Yoon 2008; Vertogradov, Kudryavcev 2023), and for Vaidya surrounded by cosmological fields in (Heydarzade, Darabi 2018a; 2018b; 2018c). The Vaidya spacetime can be extended by including the null strings, leading to the generalized Vaidya one (Wang, Wu 1999). The gravitational collapse and naked singularity formation in this spacetime have been discussed in (Acquaviva et al. 2015; Dey, Joshi 2019; Mkenyeleye et al. 2014; Ray et al. 2022; Vertogradov 2016; 2018; 2022). The generalized Vaidya spacetime has an off-diagonal term, which may lead to negative energy states for a particle like in Kerr spacetime (Penrose, Floyd 1971). The absence of such particles has been proven in (Vertogradov 2020). However, there is a similar effect for the charged particles, and the generalized Penrose process may take place in static Reissner–Nordström (Denardo, Ruffini 1973) and dynamical charged Vaidya (Vertogradov 2023) cases.

The method of extended gravitational decoupling (Ovalle 2017) allows to obtain new solutions to the Einstein field equations with a more realistic energy–momentum tensor. A generalization of Schwarzschild, Kerr and Hayward black holes has been obtained in papers (Mahapatra, Banerjee 2023; Ovalle et al. 2021; Vertogradov, Misyura 2023). Radiating hairy Schwarzschild black holes have been obtained in (Vertogradov, Misyura 2022). The hairy Vaidya spacetime can be considered as a model of gravitational collapse with a new parameter of length dimension, which can be regarded as a primary hair. In this paper, we consider the model of the gravitational collapse of the hairy Vaidya solution in order to find out if a primary hair can affect the endstate of the gravitational collapse. We also consider the strength of the singularity.

This paper is organized as follows: in Section 2 we briefly describe the Vaidya spacetime obtained by the extended gravitational decoupling method. In Section 3 we consider the gravitational collapse model and find out if a primary hair can affect the endstate of such a process. In Section 4 we investigate the strength of the central singularity, and Section 5 is the conclusion.

Throughout this paper, we use the system of geometrized units, in which $G = 1 = c$. Also, we use the signature $-+++$.

Vaidya spacetime by gravitational decoupling

The famous no-hair theorem states that a black hole might have only three charges: mass M, angular momentum J, and electric charges Q (Ruffini, Wheeler 1971). However, it can be shown that black holes can have other charges, and there is so-called soft hair (Hawking et al. 2016). One of the possibilities of evading the no-hair theorem is to use the gravitational decoupling method (Contreras et al. 2021; Ovalle 2017; 2019).

It is well known that obtaining the analytical solution of Einstein equations is a difficult task in most cases. We know that we can obtain an analytical solution of the spherically symmetric spacetime in the case of the perfect fluid as the gravitational source. However, if we consider the more realistic case when the perfect fluid is coupled to another matter, it is nearly impossible to obtain the analytical solution. In papers (Contreras et al. 2021; Ovalle 2017; 2019;), it was shown using the Minimal Geometric Deformation (MGD) (Babichev, Charmousis 2014; Sotiriou, Faraoni 2012) method that we can decouple the gravitational sources; for example, one can write the energy–momentum tensor T_{ik} as:

$$T_{ik} = \tilde{T}_{ik} + \alpha\Theta_{ik} \quad , \tag{1}$$

where $\tilde{T}_{ik}$ is the energy–momentum tensor of the perfect fluid and α is the coupling constant to the energy–momentum tensor Θ_{ik}. It is possible to solve Einstein's field equations for a gravitational source whose energy–momentum tensor is expressed as (1) by solving Einstein's field equations for each component $\tilde{T}_{ik}$ and Θ_{ik} separately. Then, by a straightforward superposition of the two solutions, we obtain the complete solution corresponding to the source T_{ik}. Since Einstein's field equations are non-linear, the MGD decoupling represents a novel and useful method in the search for and analysis of solutions, especially when we face scenarios beyond trivial cases, such as the interior of stellar systems with gravitational sources being more realistic than the ideal perfect fluid, or even when we consider alternative theories, which usually introduce new features that are difficult to deal with.

Moreover, there is only the gravitational interaction between two sources, i. e.

$$T^{ik}_{;k} = 0 \rightarrow \tilde{T}^{ik}_{;k} = \alpha\Theta^{ik}_{;k} = 0 \quad . \tag{2}$$

 https://www.doi.org/10.33910/2687-153X-2024-5-2-83-90

This fact allows us to think about Θ_{ik} as dark matter. By applying the gravitational decoupling method, one can obtain well-known black hole solutions with hair (Heydarzade et al. 2023; Ovalle et al. 2018; 2021). By using this method, the Vaidya spacetime has been obtained (Vertogradov, Misyura 2022), which in Eddington–Finkelstein coordinates has the following form:

$$ds^2 = -\left(1 - \frac{2m(v)}{r} + \alpha e^{-\frac{r}{M(v)}}\right) dv^2 + 2dvdr + r^2 d\Omega^2 \quad , \tag{3}$$

where $M(v)$ is the mass function which corresponds to usual Vaidya spacetime with $\alpha \equiv 0$. A new mass function $m(v)$ is related to the Vaidya one by

$$m(v) = M(v) + \frac{\alpha l}{2} \quad , \tag{4}$$

where $\alpha > 0$ and $l > 0$ are primary hairs. The energy–momentum tensor supporting the solution (3) is

$$\begin{aligned}
\Theta_0^0 &= \Theta_1^1 = \frac{e^{-\frac{r}{M(v)}}(M(v)-r)}{M(v)r^2} \quad , \\
\Theta_2^2 &= \Theta_3^3 = \frac{e^{-\frac{r}{M(v)}}(-2M(v)+r)}{2rM(v)^2} \quad , \\
\Theta_0^1 &= -\frac{\dot{M}(v)e^{-\frac{r}{M(v)}}}{r^2M^2(v)} \quad , \\
\tilde{T}_0^1 &= \frac{2\dot{M}(v)}{r^2} \quad .
\end{aligned} \tag{5}$$

Note that we are interested in gravitational collapse, so we assume that $\dot{M} > 0$. The energy–momentum component of the usual Vaidya spacetime $\tilde{T}_0^1 > 0$ has positive value, i. e., positive energy flux. On the other hand, the component $\Theta_0^1 < 0$ which corresponds to the negative energy flux. The coupling constant α is supposed to be very small $\alpha << 1$. Thus, the negative energy flux of the extra matter field can be interpreted as the Hawking radiation (Hawking 1975).

Gravitational collapse model

Consider the vector field K^i tangent to a non-spacelike family of geodesics ($K^i = \frac{dx^i}{d\lambda}$, where λ is an affine parameter). The fact that K^i is tangent to the geodesic congruence and parallel-transported along them gives us the following equation:

$$K^i_{;j} K^j = 0 \quad , \tag{6}$$

and

$$g_{ij} K^i K^j = \delta \quad , \tag{7}$$

where $\delta = 0$ for null and $\delta = -1$ for timelike geodesics.

From geodesic equations for K^2 and K^3 one has

$$\begin{aligned}
K^2 &= \frac{L}{r^2 \sin\beta \cos\varphi} \quad , \\
K^3 &= \frac{L\cos\beta}{r^2 \sin^2\theta} \quad ,
\end{aligned} \tag{8}$$

where L and β are constants of integration, L is an impact parameter, and β is the isotropy parameter such that $\sin\phi\tan\beta = \cot\theta$.

Let us write K^0 as

$$K^0 = \frac{Q(v,r)}{r} \quad . \tag{9}$$

Here, Q is an arbitrary function of both v and r. By using the condition $g_{ik}K^iK^k = \delta$, one obtains

$$K^1 = \frac{Q}{2r}\left(1 - \frac{2m(v)}{r} + \alpha e^{-\frac{r}{M}}\right) - \frac{l^2}{2rQ} + \frac{\delta r}{2Q} \quad . \tag{10}$$

Combining (9) and (10), one gets

$$\frac{dK^0}{d\lambda} = \frac{d}{d\lambda}\left(\frac{Q}{r}\right) = \frac{1}{r}\frac{dQ}{d\lambda} - \frac{Q}{r^2}\frac{dr}{d\lambda} \quad . \tag{11}$$

The geodesic equation, together with (10), gives us the equation with respect to $\frac{dQ}{d\lambda}$:

$$\frac{dQ}{d\lambda} = \frac{Q^2}{2r^2}\left[1 - \frac{4m}{r} + \alpha\left(\frac{7}{2} - \frac{r}{2M}\right)e^{-\frac{r}{M}}\right] + \frac{l^2}{2r^2} + \frac{\delta}{2} \quad . \tag{12}$$

If we know the mass function $m(v)$ and initial conditions, then we can find the solution of this equation (Dwivedi, Joshi 1989).

A naked singularity can be the result of a continuous gravitational collapse if one can satisfy the following two conditions:

1. The time of the singularity formation is less than the time of the apparent horizon formation;
2. There is a family of non-spacelike future-directed geodesics that terminate in the central singularity in the past;

The apparent horizon equation in the case of metric (3) is given by (Vertogradov, Misyura 2022):

$$g_{00} = 0 \to 1 - \frac{2m(v)}{r} + \alpha e^{-\frac{r}{M(v)}} = 0 \quad . \tag{13}$$

The approximate location of the apparent horizon is

$$r_{ah} = 2M(v) - \alpha(l - 2M(v)e^{-2}) \quad . \tag{14}$$

To prove the existence of the outgoing geodesics that terminate in the past in the singularity, we consider the null radial geodesic equation, which, for the metric (3), has the following form:

$$\frac{dv}{dr} = \frac{2}{1 - \frac{2m(v)}{r} + e^{-\frac{r}{M(v)}}} \quad . \tag{15}$$

The condition for the naked singularity formation is $m(0) = 0$ (Joshi 2007; Mkenyeleye et al. 2014). Let us consider the following limits:

$$\begin{aligned} &\lim_{v\to 0\ ,r\to 0} \frac{v}{r} = X_0 \quad , \\ &\lim_{v\to 0} \frac{dm(v)}{dv} = \dot{M}_0 \quad . \end{aligned} \tag{16}$$

If $\frac{dv}{dr}$ is positive and finite at the singularity, then there exists a family of non-spacelike geodesics, and the result of the gravitational collapse will be a naked singularity. Note that we demand a finite value of $\frac{dv}{dr}$ in order to have

$$\lim_{v\to 0\ ,r\to 0} g_{00} \neq 0 \quad . \tag{17}$$

Applying the notations (16) in (15), one obtains

$$X_0 = \frac{2}{1 - 2\dot{m}_0 X_0 + \alpha} \quad . \tag{18}$$

From the metric expression (3) one can see that if $m(0) = 0$, then automatically, by applying (4), $M(0) = -\frac{\alpha l}{2} \neq 0$. So, if one finds the finite value of X_0 by demanding $\alpha \neq -1$, then one will find that at the time $v = 0$ of the singularity formation the apparent horizon is absent. So, let us solve an alge-

 https://www.doi.org/10.33910/2687-153X-2024-5-2-83-90

braic equation (18) to find out if the finite and positive values of X_0 are possible. The solution of this equation is:

$$X_0^{\pm} = \frac{1+\alpha \pm \sqrt{(1+\alpha)^2 - 16\dot{m}_0}}{4\dot{m}_0} \quad . \tag{19}$$

From (19) one can easily see that one should satisfy the following condition to have finite and positive values of X_0:

$$\dot{m}_0 \leq \frac{1+\alpha}{16} \quad . \tag{20}$$

If the condition (20) is satisfied, then the result of the gravitational collapse is a naked singularity formation. If we consider the linear mass function

$$m(v) = \mu v \quad , \mu > 0 \quad , \tag{21}$$

then from (20) one obtains the following conditions:

$$\mu \leq \frac{1+\alpha}{16} \quad . \tag{22}$$

The comparison with usual Vaidya spacetime ($\mu \leq \frac{1}{16}$) shows that if $\alpha > 0$, then additional matter field might lead to the naked singularity formation when in usual Vaidya one has a black hole formation. For example, if one considers $\mu = \frac{1}{16} + \frac{\alpha}{8} > \frac{1}{16}$, then in Vaidya spacetime the result of the gravitational collapse is a black hole, but in hairy Vaidya, it is a naked singularity. One has the opposite situation in the case of $\alpha < 0$.

The strength of the central singularity

If we follow Tipler definition (Tipler 1977) which was given in the paper (Nolan 1999), a singularity is termed to be gravitationally strong or simply strong if it destroys by stretching or crushing any object which falls into it. If it does not destroy any object this way, then the singularity is termed to be gravitationally weak. We will consider the radial null geodesic with tangent vector K^i that terminates in the central singularity in the past, i. e., $v = r = \lambda = 0$. Following Clarke and Krolack (Clarke, Królak 1985), a singularity would be strong if the condition

$$\lim_{\lambda \to 0} \lambda^2 R_{ik} K^i K^k > 0 \quad . \tag{23}$$

Here R_{ik} is the Ricci tensor, which for the metric (3) is given by:

$$\begin{aligned} R_{01} &= \frac{\alpha e^{-\frac{r}{M}}}{rM} - \frac{\alpha e^{-\frac{r}{M}}}{2M^2} \quad , \\ R_{00} &= -\left(1 - \frac{2M}{r} + \alpha e^{-\frac{r}{M}}\right) R_{01} + \frac{1}{r^2}\left(2\dot{M} + \frac{\alpha r^2 \dot{M}}{M^2} e^{-\frac{r}{M}}\right) \quad . \end{aligned} \tag{24}$$

The R_{00} component can be rewritten as

$$R_{00} = -2\frac{dr}{dv} r_{01} + \frac{1}{r^2}\left(2\dot{m} + \frac{\alpha r^2 \dot{m}}{M^2} e^{-\frac{r}{M}}\right) \quad . \tag{25}$$

By combining (24), (22) and (23), we obtain

$$\lim_{\lambda \to 0} \lambda^2 R_{ik} K^i K^k = 2\dot{m}_0 X_0^2 \quad . \tag{26}$$

If the condition for the naked singularity formation is satisfied, then $X_0 > 0$ is finite. So, for the singularity to be strong, one should demand $\dot{m}_0 \neq 0$. Also, one should see that the condition for the singularity to be strong, in the linear mass function case, does not depend upon a primary hair[1]. So for the

[1] In fact, as one can see from (4), the mass function m depends upon primary hairs α and l, but in order to satisfy the condition $m(0) = 0$ one should return to the usual Vaidya mass function by linear coordinate transformation.

linear mass function, the singularity is gravitationally strong. Also, the result of the paper (Vertogradov 2022a) is satisfied, i. e. if one considers the mass function in the form $m(v) = \mu v^{\xi}$, $\xi > 1$) then, as one can see, the condition (26) is not satisfied.

Conclusion

In this paper, the gravitational collapse of hairy Vaidya spacetime has been considered. The result of such a process can lead to the naked singularity formation. A coupling constant α has an impact on the endstate of the gravitational collapse. In usual Vaidya spacetime $\alpha = 0$ the result might be a black hole formation if in the case of the linear mass function $M(v) = \mu v$ the condition $\mu > \frac{1}{16}$ is held. However, α strengthens these conditions, and the endstate of the gravitational collapse might be the naked singularity while, in usual Vaidya, the same conditions would lead to a black hole formation. We also noted that a primary hair l does not have any impact on the endstate of the continuous gravitational collapse.

We have also considered the strength of the central singularity and proved that the singularity is gravitationally strong. It means that this model violates the CCC. However, we should also note that the extra field Θ_{ik} leads to the negative energy flux, which might be interpreted as a Hawking radiation. However, the combination

$$T_0^1 = \tilde{T}_0^1 + \alpha\Theta_0^1 \ , \tag{27}$$

might be positive for the black hole. This problem is analogous to the weak energy condition violation near the central singularity in charged Vaidya spacetime (Ori 1991). So the answer to the question in the title of this paper is the following: a primary hair l does not have any impact on the naked singularity formation, but the coupling constant α does. However, this model violates energy conditions and does not violate the cosmic censorship conjecture. The spacetime (3) should be used to describe the exterior geometry of radiating or accreting massive black holes when all energy conditions are satisfied.

Conflict of Interest

The author declares that there is no conflict of interest, either existing or potential.

References

Acquaviva, G., Goswami, R., Hamid, A. I. M., Maharaj, S. D. (2015) Thermodynamics of gravity favours Weak Censorship Conjecture. *arXiv*, 1508, article 00440. https://doi.org/10.48550/arXiv.1508.00440 (In English)

Babichev, E., Charmousis, C. (2014) Dressing a black hole with a time-dependent Galileon. *Journal of High Energy Physics*, 2014, article 106. https://doi.org/10.1007/JHEP08(2014)106 (In English)

Babichev, E., Dokuchaev, V., Eroshenko, Yu. (2012) Backreaction of accreting matter onto a black hole in the Eddington-Finkelstein coordinates. *Classical and Quantum Gravity*, 29, article 115002. https://doi.org/10.1088/0264-9381/29/11/115002 (In English)

Clarke, C. J. S., Królak, A. (1985) Conditions for the occurence of strong curvature singularities. *Journal of Geometry and Physics*, 2 (2), 127–143. https://doi.org/10.1016/0393-0440(85)90012-9 (In English)

Contreras, E., Ovalle, J., Casadio, R. (2021) Gravitational decoupling for axially symmetric systems and rotating black holes. *Physical Review D*, 103 (4), article 044020. https://doi.org/10.1103/PhysRevD.103.044020 (In English)

Denardo, G., Ruffini, R. (1973) On the energetics of Reissner Nordstrøm geometries. *Physical Letters B*, 45 (3), 259–262. https://doi.org/10.1016/0370-2693(73)90198-6 (In English)

Dey, D., Joshi, P. S. (2019) Gravitational collapse of baryonic and dark matter. *Arabian Journal of Mathematics*, 8 (1), 269–292. https://doi.org/10.1007/s40065-019-0252-x (In English)

Dey, D., Mosani, K., Joshi, P. S., Vertogradov, V. (2022) Causal structure of singularity in non-spherical gravitational collapse. *The European Physical Journal C*, 82 (5), article 431. https://doi.org/10.1140/epjc/s10052-022-10401-1 (In English)

Dwivedi, I. H., Joshi, P. S. (1989) On the nature of naked singularities in Vaidya spacetimes. *Classical and Quantum Gravity*, 6 (11), article 1599. https://doi.org/10.1088/0264-9381/6/11/013 (In English)

Goncalves, S. M. C. V., Jhingan, S. (2001) Singularities in gravitational collapse with radial pressure. *General Relativity and Gravitation*, 33, 2125–2149. https://doi.org/10.1023/A:1015285531320 (In English)

Harko, T. (2003) Gravitational collapse of a Hagedorn fluid in Vaidya geometry. *Physical Review D*, 68 (6), article 064005. https://doi.org/10.1103/PhysRevD.68.064005 (In English)

Hawking, S. W. (1975) Particle creation by black holes. *Communications in Mathematical Physics*, 43, 199–220. https://doi.org/10.1007/BF02345020 (In English)
Hawking, S. W., Perry, M. J., Strominger, A. (2016) Soft hair on black holes. *Physical Review Letters*, 116(23), article 231301. https://doi.org/10.1103/PhysRevLett.116.231301 (In English)
Heydarzade, Y., Darabi, F. (2018a) Surrounded Bonnor–Vaidya solution by cosmological fields. *European Physical Journal C*, 78 (12), article 1004. https://doi.org/10.1140/epjc/s10052-018-6041-4 (In English)
Heydarzade, Y., Darabi, F. (2018b) Surrounded Vaidya black holes: Apparent horizon properties. *The European Physical Journal C*, 78 (4), article 342. https://doi.org/10.1140/epjc/s10052-018-5842-9 (In English)
Heydarzade, Y., Darabi, F. (2018c) Surrounded Vaidya solution by cosmological fields. *The European Physical Journal C*, 78 (7), article 582. https://doi.org/10.1140/epjc/s10052-018-6041-4 (In English)
Heydarzade, Y., Misyura, M., Vertogradov, V. (2023) Hairy Kiselev black hole solutions. *Physical Review D*, 108 (4), article 044073. https://doi.org/10.1103/PhysRevD.108.044073 (In English)
Heydarzade, Y., Vertogradov, V. (2023) The influence of the charge on a dynamical photon sphere. *arXiv*, 2311, article 08930. https://doi.org/10.48550/arXiv.2311.08930 (In English)
Jhingan, S., Joshi, P. S., Singh, T. P. (1996) The final fate of spherical inhomogeneous dust collapse II: Initial data and causal structure of singularity. *Classical and Quantum Gravity*, 13 (11), 3057–3067. https://doi.org/10.1088/0264-9381/13/11/019 (In English)
Joshi, P. S. (2007) *Gravitational collapse and spacetime singularities*. Cambridge: Cambridge University Press, 273 p. https://doi.org/10.1017/CBO9780511536274 (In English)
Joshi, P. S., Malafarina, D. (2011) Recent development in gravitational collapse and spacetime singularitits. *International Journal of Modern Physics D*, 20 (14), 2641–2729. https://doi.org/10.1142/S0218271811020792 (In English)
Koga, Y., Asaka, N., Kimura, M., Okabayashi, K. (2022) Dynamical photon sphere and time evolving shadow around black holes with temporal accretion. *Physical Review D*, 105 (10), article 104040. https://doi.org/10.1103/PhysRevD.105.104040 (In English)
Mahapatra, S., Banerjee, I. (2023) Rotating hairy black holes and thermodynamics from gravitational decoupling. *Physics of the Dark Universe*, 39, article 101172. https://doi.org/10.1016/j.dark.2023.101172 (In English)
Mkenyeleye, M. D., Goswami, R., Maharaj, S. D. (2014) Gravitational collapse of generalized Vaidya spacetime. *Physical Review D*, 90 (6), article 064034. https://doi.org/10.1103/PhysRevD.90.064034 (In English)
Mosani, K., Dey, D., Joshi, P. S. (2022) Global visibility of a strong curvature singularity in non-marginally bound dust collapse. *Physical Review D*, 102 (4), article 044037. https://doi.org/10.1103/PhysRevD.102.044037 (In English)
Naidu, N. F., Bogadi, R. S., Kaisavelu, A., Govender, M. (2020) Stability and horizon formation during dissipative collapse. *General Relativity and Gravitation*, 52 (8), article 79. https://doi.org/10.1007/s10714-020-02728-5 (In English)
Nielsen, A. B. (2014) Revisiting Vaidya horizons. *Galaxies*, 2 (1), 62–71 https://doi.org/10.3390/galaxies2010062 (In English)
Nielsen, A. B., Yoon, J. H. (2008) Dynamical surface gravity. *Classical and Quantum Gravity*, 25 (8), article 085010. https://doi.org/10.1088/0264-9381/25/8/085010 (In English)
Nolan, B. C. (1999) Strengths of singularities in spherical symmetry. *Physical Review D*, 60 (2), article 024014. https://doi.org/10.1103/PhysRevD.60.024014 (In English)
Oppenheimer, J. R., Snyder, H. (1939) On continued gravitational contraction. *Physical Review*, 56 (5), 455–459. https://doi.org/10.1103/PhysRev.56.455 (In English)
Ori, A. (1991) Charged null fluid and the weak energy condition. *Classical and Quantum Gravity*, 8 (8), 1559–1575. https://doi.org/10.1088/0264-9381/8/8/019 (In English)
Ovalle, J. (2017) Decoupling gravitational sources in general relativity: From perfect to anisotropic fluids. *Physical Review D*, 95 (10), article 104019. https://doi.org/10.1103/PhysRevD.95.104019 (In English)
Ovalle, J. (2019) Decoupling gravitational sources in general relativity: The extended case. *Physics Letters B*, 788, 213–218. https://doi.org/10.1016/j.physletb.2018.11.029 (In English)
Ovalle, J., Casadio, R., Contreras, E., Sotomayor, A. (2021) Hairy black holes by gravitational decoupling. *Physics of the Dark Universe* 31, article 100744. https://doi.org/10.1016/j.dark.2020.100744 (In English)
Ovalle, J., Casadio, R., Rocha, R. D. et al. (2018) Black holes by gravitational decoupling. *European Physical Journal C*, 78 (11), article 960. https://doi.org/10.1140/epjc/s10052-018-6450-4 (In English)
Papapetrou, A. (1985) *A Random Walk in Relativity and Cosmology*. New York: John Wiley & Sons Publ., 184 p. (In English)
Penrose, R., Floyd, R. M. (1971) Extraction of rotational energy from a black hole. *Nature Physical Science*, 229 (6), 177–179. https://doi.org/10.1038/physci229177a0 (In English)
Ray, S., Panda, A., Majumder, B. et al. (2022) Collapsing scenario for the k-essence emergent generalised Vaidya spacetime in the context of massive gravity's rainbow. *Chinese Physics C*, 46 (12), article 125103. https://doi.org/10.1088/1674-1137/ac8868 (In English)
Ruffini, R., Wheeler, J. A. (1971) Introducing the black hole. *Physics Today*, 24 (1), 30–41. https://doi.org/10.1063/1.3022513 (In English)

Santos, N. O. (1985) Non-adiabatic radiating collapse. *Monthly Noices of the Royal Astronomical Society*, 216 (2), 403–410. https://doi.org/10.1093/mnras/216.2.403 (In English)
Singh, T. P., Joshi, P. S. (1996) The final fate of spherical inhomogeneous dust collapse. *Classical and Quantum Gravity*, 13 (3), 559–571. https://doi.org/10.1088/0264-9381/13/3/019 (In English)
Solanki, J., Perlick, V. (2022) Photon sphere and shadow of a time-dependent black hole described by a Vaidya metric. *Physical Review D*, 105 (6), article 064056. https://doi.org/10.1103/PhysRevD.105.064056 (In English)
Sotiriou, T. P., Faraoni, V. (2012) Black holes in scalar-tensor gravity. *Physical Review Letters*, 108 (8), article 081103. https://doi.org/10.1103/PhysRevLett.108.081103 (In English)
Tipler, F. J. (1977) Singularities in conformally flat spacetimes. *Physics Letters A*, 64 (1), 8–10. https://doi.org/10.1016/0375-9601(77)90508-4 (In English)
Vaidya, P. C. (1951) Nonstatic solutions of Einstein's field equations for spheres of fluids radiating energy. *Physical Review*, 83 (1), article 10. https://doi.org/10.1103/PhysRev.83.10 (In English)
Vertogradov, V. (2016) Naked singularity formation in generalized Vaidya space-time. *Gravitation and Cosmology*, 22 (2), 220–223. https://doi.org/10.1134/S020228931602016X (In English)
Vertogradov, V. (2018) The eternal naked singularity formation in the case of gravitational collapse of generalized Vaidya space-time. *International Journal of Modern Physics A*, 33 (17), article 1850102. https://doi.org/10.1142/S0217751X18501026 (In English)
Vertogradov, V. (2020) The negative energy in generalized Vaidya spacetime. *Universe*, 6 (9), article 155. https://doi.org/10.3390/universe6090155 (In English)
Vertogradov, V. (2022a) Non-linearity of Vaidya spacetime and forces in the central naked singularity. *Physics of Complex Systems*, 3 (2), 81–85. https://www.doi.org/10.33910/2687-153X-2022-3-2-81-85 (In English)
Vertogradov, V. (2023) Extraction energy from charged Vaidya black hole via the Penrose process. *Communications in Theoretical Physics*, 75 (4), article 045404. https://doi.org/10.1088/1572-9494/acc018 (In English)
Vertogradov, V., Kudryavcev, D. (2023) Generalized vaidya spacetime: horizons, conformal symmetries, surfacegravity and diagonalization. *Modern Physics Letters A*, 38 (24n25), article 2350119. https://doi.org/10.1142/S0217732323501195 (In English)
Vertogradov, V., Misyura, M. (2022) Vaidya and generalized Vaidya solutions by gravitational decoupling. *Universe*, 8 (11), article 567. https://doi.org/10.3390/universe8110567 (In English)
Vertogradov, V., Misyura, M. (2023) The regular black hole by gravitational decoupling. *Physical Sciences Forum*, 7 (1), article 27. https://doi.org/10.3390/ECU2023-14058 (In English)
Wang, A., Wu, Yu. (1999) Generalized Vaidya solutions. *General Relativity and Gravitation*, 31 (1), 107–114. https://doi.org/10.1023/A:1018819521971 (In English)

Physics of Semiconductors.
Electronic structure of solids

UDC 537.9

EDN VYWZTC
https://www.doi.org/10.33910/2687-153X-2024-5-2-91-103

As_4Se_4 crystal versus As_4Se_4 molecule: A plane wave DFT study of the geometric and electronic structure

A. A. Gavrikov [1] ✉, V. G. Kuznetsov [2], V. A. Trepakov [2]

[1] Herzen State Pedagogical University of Russia, 48 Moika Emb., Saint Petersburg 191186, Russia
[2] Ioffe Institute, 26 Polytekhnicheskaya Str., Saint Petersburg 194021, Russia

Authors

Anton A. Gavrikov, ORCID: 0000-0001-6121-2013, e-mail: agavrikov@herzen.spb.ru

Vladimir G. Kuznetsov, ORCID: 0000-0003-1996-0055, e-mail: vladimir.kuznetsov@mail.ioffe.ru

Vladimir A. Trepakov, e-mail: trevl@mail.ioffe.ru

For citation: Gavrikov, A. A., Kuznetsov, V. G., Trepakov, V. A. (2024) As_4Se_4 crystal versus As_4Se_4 molecule: A plane wave DFT study of the geometric and electronic structure. *Physics of Complex Systems*, 5 (2), 91–103. https://www.doi.org/10.33910/2687-153X-2024-5-2-91-103 EDN VYWZTC

Received 4 March 2024; reviewed 11 April 2024; accepted 11 April 2024.

Funding: This study was partly supported by the Ministry of Education of the Russian Federation as part of the state-commissioned assignment (project No. VRFY-2023-0005).

Abstract. Chalcogenide crystals reveal a wide range of changes in chemical and physical properties under band gap light illumination. A majority of these properties are determined by the electronic structure. However, to date there are only a few theoretical articles on the electronic structure of the As_4Se_4 molecule and only two on the As_4Se_4 crystal. We have studied, for the first time, the geometric and electronic structure of the As_4Se_4 crystal versus the As_4Se_4 molecule in the framework of a periodic model by the DFT method within the same approximations. Equilibrium bond lengths and bond angles were calculated together with charge density differences, Mulliken, Löwdin and Bader charges, and also Mulliken overlap populations, and were compared for the crystal and the molecule. A character of chemical bonding in the As_4Se_4 crystal versus the As_4Se_4 molecule was analyzed. The bandstructure DFT calculations were carried out and demonstrated that the As_4Se_4 crystal is an indirect-gap semiconductor.

Keywords: chalcogenides, geometric and electronic structure, chemical bonding, As_4Se_4, molecule, molecular crystal, DFT method

Introduction

Amorphous chalcogenide materials which represent alloys of S or Se with such metals as As, Ge etc. reveal a wide range of changes in chemical and physical properties under band gap light illumination (Elliott 1986; Kolobov 2003; Kolobov, Elliott 1995; Owen et al. 1985). These changes can be reversible or irreversible. While photoinduced structural changes in chalcogenide glasses have been studied intensively since 1980s (Shimakawa et al. 1998; Tanaka 2001; Yang et al. 1987), the electronic structure of molecular chalcogenide crystals together with the photoinduced transition mechanisms have remained deficiently explored. For example, in the As_4Se_4 molecular crystal transition from a crystalline to an amorphous phase can be induced by band gap light (Kolobov, Elliott 1995), and this transition may be reversible. In paper (Krecmer et al. 1997) the another reversible effect, namely so-called the optomechanical effect with the reversible optical-induced optical anisotropy (dichroism), was observed in amorphous $As_{50}Se_{50}$ thin films. Following the paper (Krecmer, Moulin, Stephenson et al. 1997) upon irradiation with polarized light, thin films of amorphous $As_{50}Se_{50}$, exhibit reversible nanocontraction parallel to the direction of the electric vector of the polarized light and nanodilatation along the axis orthogonal to the electric vector of the light.

As opposed to amorphous As_4Se_4 there are few studies regarding the crystalline structure of As_4Se_4. The first experimental studies of the As_4Se_4 molecular crystal geometry were performed in 1970s (Bastow, Whitfield 1973; Goldstein, Paton 1974; Renninger, Averbach 1973; Smail, Sheldrick 1974). Realgar-like molecular crystal As_4Se_4 with space group symmetry (P 1 21/c 1) belongs to the monoclinic crystal system and has a unit cell with parameters a = 9.63 Å; b = 13.8 Å; c = 6.73 Å; α = γ = 90°; β = 107.8° (Bastow, Whitfield 1973) consisting of 4 formula units As_4Se_4 as building blocks. As follows from X-ray diffraction studies (Goldstein, Paton 1974), As_4Se_4 is a molecular crystal in which individual As_4Se_4 molecules can be distinguished, having two intramolecular homopolar covalent As–As bonds with slightly different bond lengths of 2.571 Å and 2.560 Å respectively. For comparison, the As–As bond length in amorphous arsenic (a-As) is 2.49 Å (Elliott 1990). The As–As–Se angle, which has its vertex at one of the As atoms that are part of the As–As bonds (101.2° (Goldstein, Paton 1974)), is also significantly larger than the average bond angle of 98° in a–As (Elliott 1990).

The first attempts of theoretical study into the electronic structure of an As_4Se_4 molecular crystal with the unit cell containing four As_4Se_4 molecules used a simplified approach based on a study of the electronic structure of an individual As_4Se_4 molecule by different semi-empirical methods (Chen 1975; Salaneck et al. 1975; Tanaka et al. 1978). Based on the results of these molecular calculations, the photoemission spectra of the crystal were interpreted (Chen 1975; Salaneck et al. 1975). In the first paper (Salaneck et al. 1975) authors used a semi-empirical variant of the self-consistent field method, namely the so-called complete-neglect-of-differential-overlap (CNDO) method; in the second one (Tanaka et al. 1978) — an intermediate-neglect-of-differential-overlap (INDO) method; and in the third one (Chen 1975) — an extended Huckel or Wolfsberg–Helmholz method. Later the calculations of the electronic structure of an individual molecule were already performed using ab initio methods: self-consistent-field *Xα* scattered-wave method (Babić, Rabii 1988) and the density functional method (Babić et al. 1989).

A study of the electronic structure of an individual As_4Se_4 molecule instead of that of a molecular crystal As_4Se_4 is possibly a rough approximation. However, the direct calculation of an As_4Se_4 crystal has long been difficult, especially by ab initio methods, due to the large unit cell of the crystal containing 32 atoms. Therefore, as far as we know no first-principles electronic structure calculations were performed until 1976. The first nonempirical calculation of the electronic structure of pristine crystal As_4Se_4 was accomplished within the chemical pseudopotential approach (Anderson 1969) by the local orbital method (Bullett 1976a) proposed in (Bullett 1975; 1976b). In addition, we know only one more article with the electronic structure ab initio study of the As_4Se_4 crystal (Hasan et al. 2019). In this work the equilibrium geometry of the As_4Se_4 crystal was calculated using the DFT method within Generalized Gradient Approximation (GGA) with the exchange-correlation (XC) functional of PBE (Perdew et al. 1996) type with the help of the plane-wave pseudopotential code VASP. The results of the paper (Hasan et al. 2019) are unsatisfactory, in our opinion, since the parameters of the calculated equilibrium geometry differ significantly from the experimental ones, some by more than 10%. Unsatisfactory results of the unique article with the DFT study of the crystalline As_4Se_4 electronic structure (Hasan 2021; Hasan et al. 2019) were the motivation to accomplish new research.

Methods and computational details

A distinctive feature of molecular crystals is that their potential energy surface (PES) usually has a relatively flat landscape with relatively small local minima, which makes it difficult to optimize geometry and to find the equilibrium geometry (Beran 2016). This problem also occurs for the As_4Se_4 molecular crystal. In this regard, it is of interest to find the theoretical equilibrium geometry of a given crystal and to study a question to what extent the quality of the resulting geometry depends on the methods and approximations used in the calculations.

We studied the dependence of the theoretical equilibrium geometry of the As_4Se_4 crystal calculated by the DFT method against the type of XC functionals and pseudopotentials. To this end, we carried out a series of calculations to fully optimize the geometry of the As_4Se_4 crystal, including lattice parameters and atomic positions, using two plane-wave pseudopotential codes: CASTEP (Clark et al. 2005; Segall et al. 2002) and Quantum Espresso (QE) (Giannozzi et al. 2009; 2017) with GGA XC functionals in the forms of PBE (Perdew et al. 1996) and PBEsol (Perdew et al. 2008), taking into account the van der Waals (vdW) correction in the form of Grimme-D2 (Grimme 2006). To describe

 https://www.doi.org/10.33910/2687-153X-2024-5-2-91-103

electronic–ionic interactions, two types of pseudopotentials were used, namely the Projector Augmented–Wave (PAW) (Blöchl 1994; Kresse, Joubert 1999) potentials in QE code and the optimized norm-conserving Vanderbilt (ONCV) pseudopotentials (Hamman 2013) in CASTEP and QE codes. The PAW potentials were taken from the PAW data-set generated by Dal Corso (Dal Corso 2014); the ONCV scalar-relativistic pseudopotentials — from the Schlipf–Gygi pseudopotentials library (Schlipf, Gygi 2015) (issue 2020-02-06) for CASTEP code and from PseudoDojo pseudopotentials library (van Setten et al. 2018) for QE code.

The geometry optimization in both codes was performed using the Broyden–Fletcher–Goldfarb–Shanno (BFGS) (Eyert 1996; Pfrommer et al. 1997; Press et al. 1992; Shanno 1978) algorithm. The atomic positions and cell parameters were optimized until the energy difference, the Hellmann–Feynman forces on the atoms, and all the stress components did not exceed the values 1×10^{-7} eV atom^{-1}, 5×10^{-4} eV Å^{-1}, 1×10^{-3} GPa for CASTEP code and the values 1×10^{-8} Ry, 4×10^{-5} Ry bohr^{-1}, 1×10^{-2} kbar for QE code, respectively. It is worth noting here that in QE code it is accepted to use as the energy tolerances the extensive quantities, as opposed to CASTEP code. The convergence criteria of a self-consistent energy process were specified by the tolerance values 1×10^{-8} eV atom^{-1} for CASTEP code and 1×10^{-10} Ry for QE code.

The convergence of total energy with respect to the density of the Monkhorst–Pack k-mesh (Monkhorst, Pack 1976) in the irreducible Brillouin zone (IBZ) and to the plane-wave kinetic energy cutoff was studied. It was found that to achieve the convergence of total energy within a few meV the following values of the energy cutoff should be taken: 1200 eV for the ONCV pseudopotentials in code CASTEP and 98 Ry for ONCV pseudopotentials and PAW potentials in code QE. For given cutoff energies, convergence of the total energy with the required accuracy corresponds to $7 \times 5 \times 9$ k-point grid (96 k-points in IBZ) in both codes.

The results of the As_4Se_4 crystal geometry optimization with different XC functionals and pseudopotentials are presented in Table 1 (cell parameters) along with experimental data and the results of theoretical work (Hasan, Baral, Ching 2019; Hasan 2021), and in Table 2 (atomic positions).

Table 1. Theoretical equilibrium geometry of the As_4Se_4 crystal calculated in the present work by DFT method using CASTEP and Quantum Espresso codes with various XC functionals and pseudopotentials

Code	DFT	Pseudopotentials (type)	Valence electrons	a, b, c (Å)	α = γ; β (degrees)	Cell volume V_0(Å^3)	Density (g/cm^3)
CASTEP	PBE+D2 (Grimme)	ONCV	As: $4s^24p^3$ Se: $4s^24p^4$	9.612 13.811 6.732	90 106.460	857.034	4.770
QE	PBE+D2 (Grimme)	PAW	As: $4s^24p^3$ Se: $4s^24p^4$	9.617 13.794 6.738	90 106.413	857.396	4.768
QE	PBE+D2 (Grimme)	ONCV	As: $3d^{10}4s^24p^3$ Se: $3d^{10}4s^24p^4$	9.610 13.784 6.734	90 106.424	855.579	4.779
QE	PBEsol+D2 (Grimme)	ONCV	As: $3d^{10}4s^24p^3$ Se: $3d^{10}4s^24p^4$	9.113 13.380 6.518	90 107.173	759.289	5.385
QE	PBEsol	ONCV	As: $3d^{10}4s^24p^3$ Se: $3d^{10}4s^24p^4$	9.267 13.696 6.623	90 107.529	801.529	5.101
CASTEP	PBEsol	ONCV	As: $4s^24p^3$ Se: $4s^24p^4$	9.281 13.746 6.635	90 107.640	806.712	5.068
VASP (Hasan et al. 2019)	PBE	PAW	As: $4s^24p^3$ Se: $4s^24p^4$	7.189 14.746 10.580	90 114.840	1121.500	
Expt.				9.63 13.80 6.73	90 107.8	851.562	4.801

Table 2. Fractional coordinates of symmetry non-equivalent atoms in the As_4Se_4 crystal. Experimental data from (Bastow, Whitfield 1973)

	Experimental			PBE+D2 ONCV (CASTEP)			PBE+D2 ONCV (QE)		
	x/a	x/b	x/c	x/a	x/b	x/c	x/a	x/b	x/c
As1	0.1141	0.0182	–0.2452	0.1118	0.0215	–0.2427	0.1114	0.0218	–0.2426
As2	0.4271	–0.1405	–0.1367	0.4297	–0.1369	–0.1355	0.4295	–0.1363	–0.1378
As3	0.3256	–0.1312	0.1752	0.3258	–0.1298	0.1804	0.3258	–0.1301	0.1782
As4	0.0363	–0.1603	–0.2962	0.0366	–0.1604	–0.2993	0.0368	–0.1604	–0.3005
Se1	0.3485	0.0101	–0.3065	0.3466	0.0143	–0.3103	0.3461	0.0153	–0.3107
Se2	0.2132	0.0252	0.1245	0.2131	0.0283	0.1287	0.2127	0.0282	0.1284
Se3	0.2414	–0.2323	–0.3729	0.2449	–0.2324	–0.3731	0.2450	–0.2318	–0.3756
Se4	0.1018	–0.2178	0.0526	0.1016	–0.2189	0.0524	0.1022	–0.2196	0.0503

For the best theoretical equilibrium geometry (row 1 of Table 1), calculated using the CASTEP code with a generalized gradient XC functional in the form of PBE with a vdW correction in the form of Grimme-D2 (Grimme 2006), as well as with ONCV pseudopotentials proposed by Hamann (Hamann 2013) to describe electron–ion interactions, we calculated various electronic structure characteristics reflecting the nature of the chemical bond in As_4Se_4, namely the charge electron density difference (CDD) along with atomic and overlap populations.

In addition, within the framework of the same approach and approximations, we carried out a DFT study of the geometric and electronic structure of the As_4Se_4 crystal versus the As_4Se_4 molecule. Scientific literature contains various theoretical data on the geometry and chemical bonding both in As_4Se_4 molecules and in the As_4Se_4 crystal, but their comparative theoretical analysis in the same approximations is missing. In the present work the geometric structure of the As_4Se_4 molecule was calculated within the periodic model with a cubic box of size 10 × 10 × 10 Å by a plane-wave DFT method with PBE XC functional without vdW correction and with ONCV pseudopotentials.

Charge density difference

The electron density difference (Charge Density Difference, CDD) is defined as the difference in electron density in the structure under study (molecule and crystal) and the sum of isolated atoms. The calculated CDD allows to visualize covalent bonds (CBs) as an increase in electron density between atoms and the lone-pair (LP) electrons, which are associated also with an increased electron density.

Population analysis

Atomic charges in molecules and solids are ill-defined in the sense that they do not represent observable quantities. Therefore, their values should be considered only relative to prototypical systems. Nevertheless, a concept of atomic charge in molecules and crystals is a useful tool because it provides an intuitive way to analyze and interpret the electronic structure. To date, various methods of calculating the atomic and overlap populations have been developed in the quantum chemistry of molecules and solids. The most common and widely used are the Mulliken (Mulliken 1955), Löwdin (Löwdin 1950) and Bader (Bader 1990; Bader et al. 1979) charges. These population analysis schemes are used in the quantum chemistry of solids within both the linear combination of atomic orbitals (LCAO) codes and the plane wave (PW) codes. In the present paper we used the PW implementation of these population analysis schemes (Henkelman et al. 2006; Sanchez–Portal et al. 1995; Sanville et al. 2007; Segall et al. 1996; 2010; Tang et al. 2009).

Results and discussion

Geometric structure of the As_4Se_4 crystal versus the As_4Se_4 molecule

The As_4Se_4 molecule and As_4Se_4 crystal geometric structures are shown in Figs. 1 and 2 respectively. As can be seen from Tables 1 and 2, in the best calculations we performed (the first three rows of Table 1 — calculations with PBE+D2 XC-functionals), the discrepancy between the parameters of the calculated and experimental equilibrium geometry does not exceed 0.2%. In addition, it should be noted that (i) the quality of the equilibrium geometry strongly depends on whether van der Waals corrections are taken into account or not; (ii) in contrast to the PBE+D2, the PBEsol XC functionals, as with and without vdW

 https://www.doi.org/10.33910/2687-153X-2024-5-2-91-103

correction, do not reproduce well the experimental equilibrium geometry; (iii) the high accuracy of the equilibrium geometry calculated with both ONCV and PAW pseudopotentials indicates the high quality of the pseudopotentials used; and (iv) taking into account the d-electrons of arsenic and sulfur atoms does not affect the quality of the calculated equilibrium geometry.

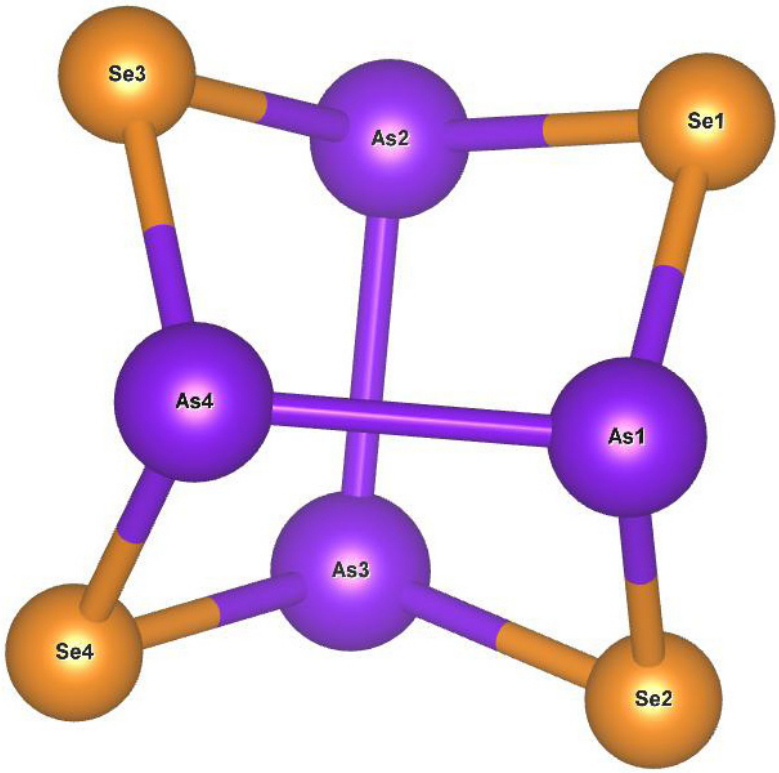

Fig. 1. Structure of the As_4Se_4 molecule. As atoms are shown in violet and Se atoms — in orange

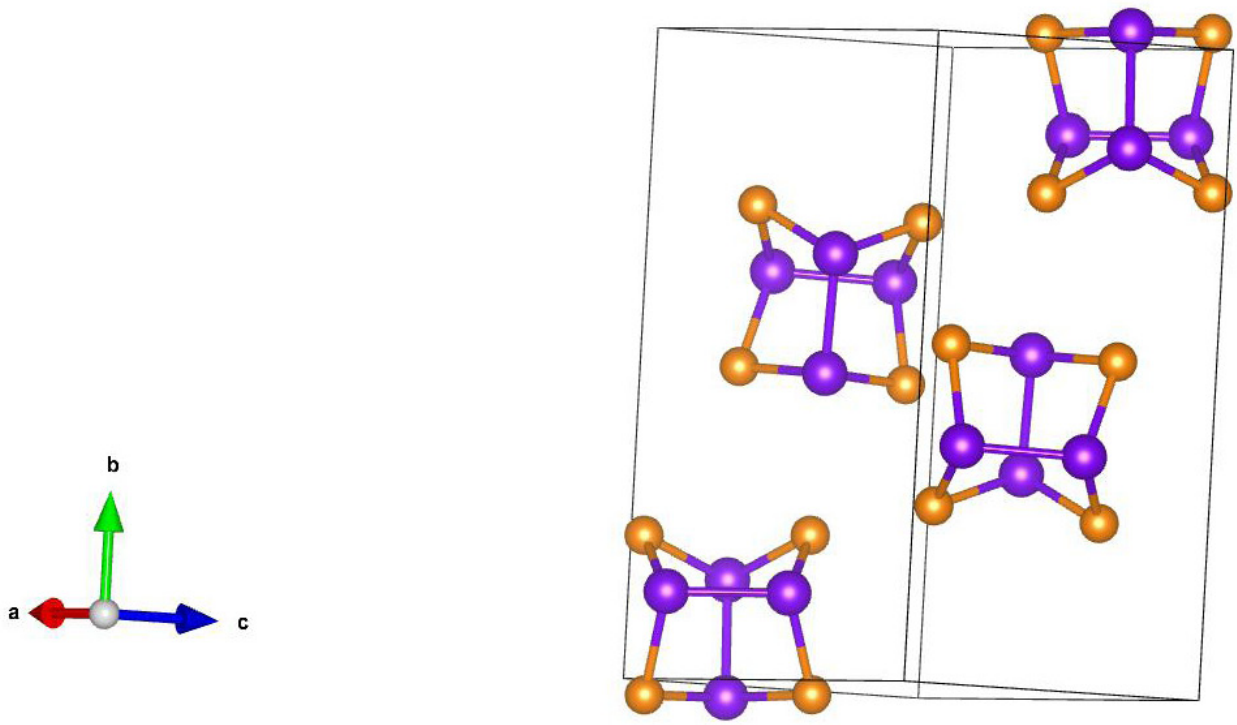

Fig. 2. Structure of the As_4Se_4 crystal. As atoms are shown in violet and Se atoms — in orange

Bond lengths and valence angles in the As_4Se_4 crystal for the best equilibrium geometry and in the As_4Se_4 molecule are presented in Table 3.

Table 3. Bond lengths and angles in the As_4Se_4 crystal versus the molecule calculated by CASTEP (PBE+D2 ONCV for the crystal and PBE ONCV for the molecule) along with experimental data for the As_4Se_4 crystal (Goldstein, Paton 1974)

Bond lengths, Å											
As – As				**As – Se**				**Se – Se**			
	Expt	**cryst**	**mol**		**Expt**	**cryst**	**mol**		**Expt**	**cryst**	**mol**
As2 – As3	2.560	2.595	2.630	As1 – Se1	2.393	2.428	2.392	Se1 ⋯ Se3	3.487	3.537	3.521
As1 – As4	2.571	2.612	2.630	As2 – Se1	2.385	2.419	2.392	Se3 ⋯ Se4	3.475	3.518	3.521
As2 ⋯ As4	3.591	3.638	3.625	As2 – Se3	2.384	2.417	2.392	Se4 ⋯ Se2	3.511	3.572	3.521
As4 ⋯ As3	3.591	3.639	3.627	As4 – Se3	2.376	2.411	2.392	Se2 ⋯ Se1	3.496	3.545	3.521
As3 ⋯ As1	3.610	3.659	3.627	As4 – Se4	2.378	2.410	2.392				
As1 ⋯ As2	3.610	3.660	3.627	As3 – Se4	2.386	2.418	2.392				
				As3 – Se2	2.387	2.419	2.392				
				As1 – Se2	2.381	2.414	2.392				

Angles, °											
As – Se – As				**Se – As – Se**				**As – As – Se**			
	Expt	**cryst**	**mol**		**Expt**	**cryst**	**mol**		**Expt**	**cryst**	**mol**
As1 – Se1 – As2	98.2	98.089	98.597	Se1 – As2 – Se3	94.0	94.103	94.776	As4 – As1 – Se2	101.2	101.674	100.719
As2 – Se3 – As4	97.9	97.807	98.541	Se3 – As4 – Se4	93.9	93.724	94.774	As4 – As1 – Se1	100.2	99.587	100.678
As4 – Se4 – As3	97.8	97.824	98.598	Se4 – As3 – Se2	94.7	95.204	94.803	As3 – As2 – Se1	101.9	102.436	100.761
As3 – Se2 – As1	98.4	98.416	98.636	Se2 – As1 – Se1	94.2	94.136	94.802	As3 – As2 – Se3	100.9	100.456	100.778
								As1 – As4 – Se3	102.0	102.438	100.777
								As1 – As4 – Se4	101.6	101.253	100.762
								As2 – As3 – Se4	101.3	101.537	100.677
								As2 – As3 – Se2	100.7	100.192	100.718

As can be seen from Table 3, the As–As bond lengths both in the molecule and the crystal are considerably longer than 2.42 Å, the covalent diameter of the As atom (Schomaker, Stevenson 1941), which qualitatively indicates the presence of effective repulsion between opposite As atoms (As_1–As_4, As_2–As_3). On the other hand, the values of the overlap populations As_1–As_4 and As_2–As_3 (see Table 4) indicate the absence of effective interaction between these atoms in the molecule and its antibonding character between the same atoms in the crystal. This contradicts the generally accepted qualitative ideas about the existence of chemical bonds between the opposite arsenic atoms both in the molecule and in the crystal, although an attempt to describe the complex nature of interactions by considering only pair interactions is very simplified.

Another attempt of this kind of simplified qualitative consideration was made in (Goldstein, Paton 1974). The authors explain the elongation of the As–As bond by a preference of the molecules for a bonding configuration having D_{2d} symmetry concomitant with a minimization of the intramolecular repulsions between non-bonded atoms. In their opinion, evidence of these repulsions is confirmed by the short intramolecular Se...Se separations in As_4Se_4 (see column Expt in Table 3), in contrast to the shortest intra-ring and intra-chain non-bonded Se...Se separations in α-Se (Cherin, Unger 1972) and in trigonal Se (Cherin, Unger 1967) which are equal to 3.72 Å and 3.716 Å respectively.

 https://www.doi.org/10.33910/2687-153X-2024-5-2-91-103

Table 4. Bond lengths and overlap populations in the As_4Se_4 crystal versus the molecule calculated by CASTEP (PBE+D2 ONCV for the crystal and PBE ONCV for the molecule) along with experimental data for the As_4Se_4 crystal (Goldstein, Paton 1974)

Bond	Bond lengths, Å		Mulliken overlap populations	
	mol	cryst	mol	cryst
As4 – Se4	2.392	2.410	0.24	–0.90
As4 – Se3	2.392	2.410	0.13	–0.41
As1 – Se2	2.392	2.414	0.24	–0.79
As2 – Se3	2.392	2.417	0.13	–0.09
As3 – Se4	2.392	2.418	0.26	–0.06
As2 – Se1	2.392	2.419	0.24	–0.52
As3 – Se2	2.392	2.419	0.24	–0.32
As1 – Se1	2.392	2.428	0.26	–0.15
As2 – As3	2.630	2.595	–0.03	–2.94
As1 – As4	2.630	2.612	–0.03	–2.28

The present DFT calculations demonstrate that the As–Se bond length in the As_4Se_4 molecule is 2.392 Å (see Table 3), which is slightly larger than the sum of the covalent radii of As and Se, 1.21 Å and 1.17 Å respectively (Schomaker, Stevenson 1941), while the average As–Se bond length in the As_4Se_4 crystal was found to be 2.417 Å, which is one percent more than in the molecule. The calculated As–Se bond lengths both for the molecule and the crystal correlate with the sum of the covalent radii of As and Se atoms.

Van der Waals radii of As and Se atoms are 1.85 Å and 1.90 Å respectively following (https://periodictable.com/Properties/A/VanDerWaalsRadius.v.html). The DFT calculated distances As–As and Se–Se for atoms belonging to the different molecules of the crystal As_4Se_4 were found to be in agreement with predicted double van der Waals radii of As and Se atoms respectively.

CDD and population analysis for the As_4Se_4 crystal versus the As_4Se_4 molecule

The visualized CDD of the As_4Se_4 molecule and the As_4Se_4 crystal are presented in Figs. 3 and 4 respectively. The CDD clouds reveal an increase in electron density and are marked by red color in the figures. It is generally accepted that CDD clouds indicate the presence of covalent bonds or lone electron pairs. In the case of As_4Se_4 we are talking about bonds As–Se, As–As and lone-pair electrons in regions near As and Se atoms both in the molecule and the crystal. Indeed, being three-fold coordinated, arsenic has a single s^2 lone pair according to valence shell $s^2p_xp_yp_z$ (single red CDD cloud near each As atom). Selenium is two-fold coordinated and has, in addition to a s^2 lone pair, a p_z^2 lone pair according to valence shell $s^2p_xp_yp_z^2$ (two red CDD clouds near each Se atom).

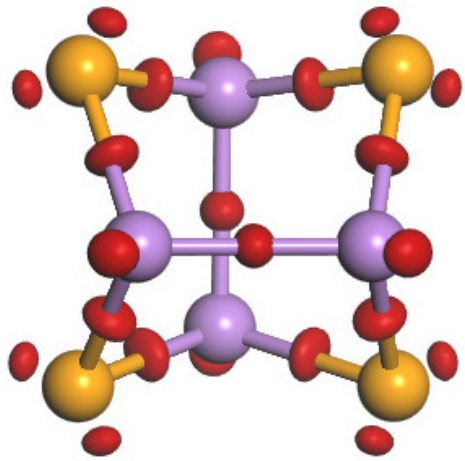

Fig. 3. As_4Se_4 molecule: CDD visualization of the electronic structure

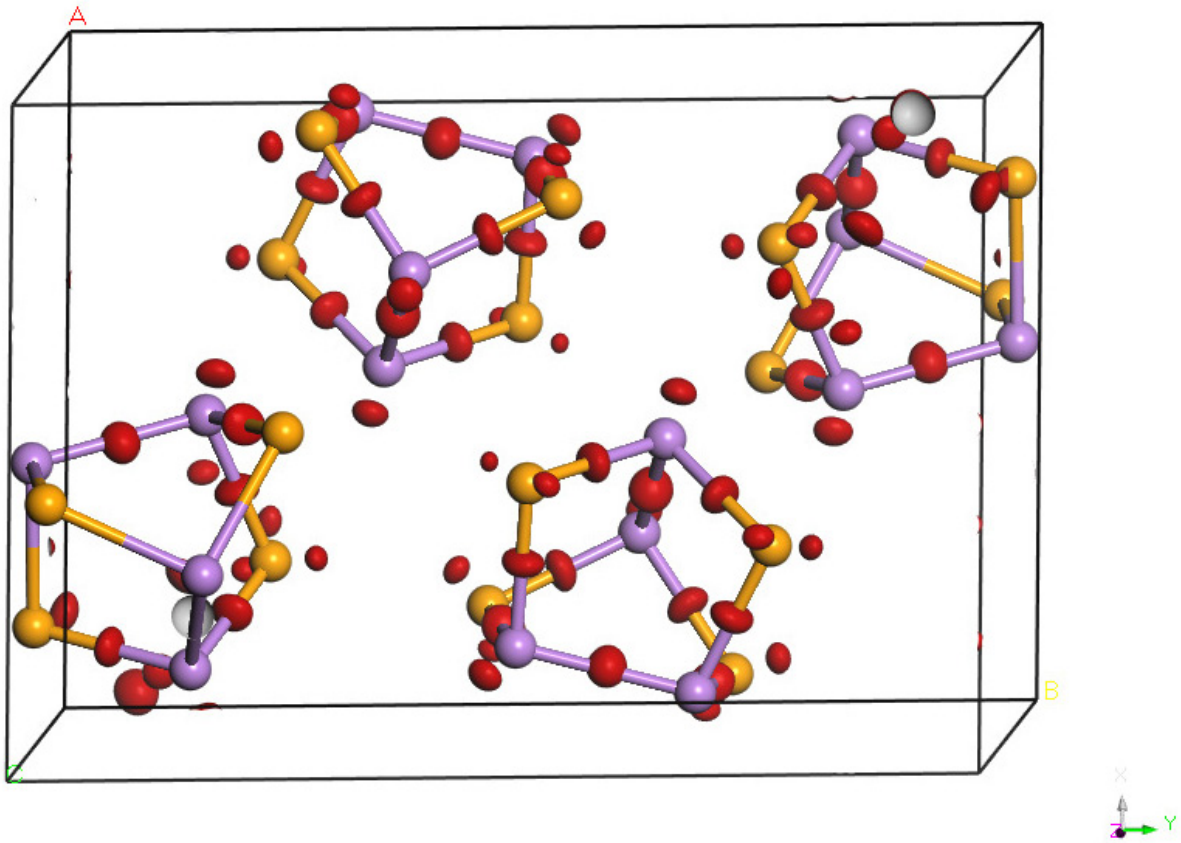

Fig. 4. As_4Se_4 crystal: CDD visualization of the electronic structure

The values of Mulliken, Löwdin and Bader charges in the As_4Se_4 crystal for the best equilibrium geometry along with those in the As_4Se_4 molecule are presented in Table 5. One can see that the absolute values of Mulliken charges for a crystal are on average 20 percent greater than those for a molecule. The values of Bader charges turn out to be almost 2 times greater than the values of the Mulliken and Löwdin charges, which in turn are only slightly different from each other. It is noteworthy that relative differences in the values of the Bader charges for a crystal and a molecule are on average significantly smaller than the corresponding differences for the values of the Mulliken and Löwdin charges, with the exception of atoms As3, As4 and Se2, for which the indicated differences are very significant for all three charge calculation schemes. These significant differences can only be due to intermolecular interactions in the crystal As_4Se_4, which lead to the electron density redistribution. The average Bader charge for As is +0.404 for crystal and +0.409 for molecule, whereas for Se, it is –0.404 and –0.409 respectively. The Bader charges are low, emphasizing only moderate ionic contribution (polar covalency) to the bonding. Overlap populations (Table 4) for the intramolecular As–As distances with lengths 2.595 Å and 2.612 Å are equal to –2.94 and –2.28 respectively. It means the antibonding character of effective interaction between the nearest intramolecular As atoms in the As_4Se_4 crystal. As opposed to the crystal, in the molecule the overlap populations for As–As distances with lengths 2.630 Å are equal to –0.03, which corresponds to the absence of effective interaction between these atoms.

Table 5. Mulliken, Löwdin and Bader charges of the As_4Se_4 crystal

	Mulliken charge		Löwdin charge		Bader charge	
	crystal	molecule	crystal	molecule	crystal	molecule
As1	0.230	0.192	0.195	0.186	0.414	0.410
As2	0.227	0.197	0.179	0.181	0.407	0.405
As3	0.216	0.191	0.198	0.186	0.429	0.411
As4	0.234	0.197	0.155	0.181	0.364	0.410
Se1	–0.207	–0.190	–0.097	–0.087	–0.410	–0.406

https://www.doi.org/10.33910/2687-153X-2024-5-2-91-103

Table 5. Completion

	Mulliken charge		Löwdin charge		Bader charge	
	crystal	molecule	crystal	molecule	crystal	molecule
Se2	–0.214	–0.193	–0.072	–0.084	–0.389	–0.405
Se3	–0.266	–0.203	–0.096	–0.087	–0.409	–0.411
Se4	–0.220	–0.190	–0.103	–0.087	–0.405	–0.415

As_4Se_4 crystal: band structure and DOS

The band structure of the As_4Se_4 crystal calculated by DFT method with PBE XC functional, Grimme-D2 vdW correction and ONCV pseudopotentials, as implemented in CASTEP code, is shown in Fig. 5. It was found that the As_4Se_4 crystal is an indirect gap semiconductor with an indirect gap ($E_g^{(i)}$ in Fig. 5) value of 0.979 eV whereas the direct gap value ($E_g^{(d)}$ in Fig. 5) is 1.42 eV. At the same time, it should be kept in mind that the semilocal XC-functionals usually underestimate the band gap by about 50% due to incomplete exclusion of the electron self-interaction (Perdew, Zunger 1981). The experimental value is expected to be larger, although its magnitude is unknown.

Inspection of the band structure of the As_4Se_4 crystal (Fig. 5) shows that the valence band maximum (VBM) lies in the interval between Γ and Z k-points, while the conduction band minimum (CBM) is in the interval between D and Z k-points, thus forming an indirect band gap. The coordinates of high-symmetry k-points D and Z in Brillouin zone are (-½, 0, ½) and (0, 0, ½) respectively.

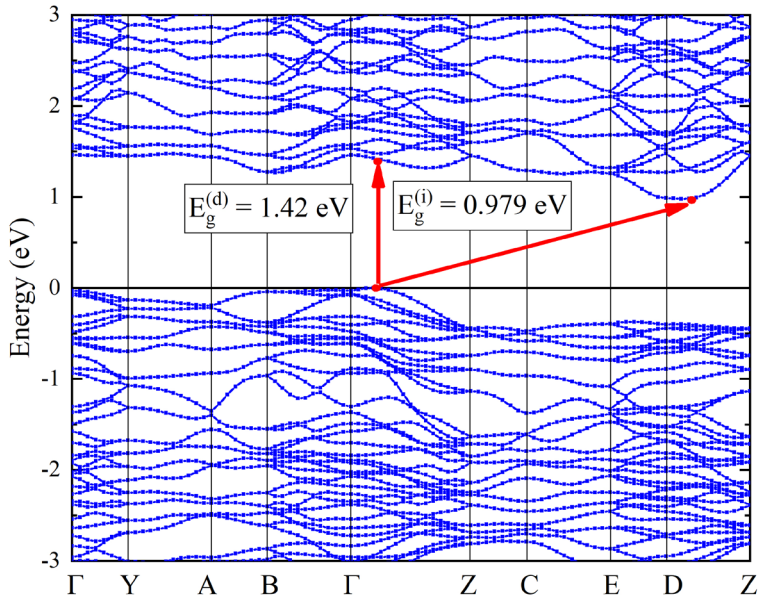

Fig. 5. Band structure of the As_4Se_4 crystal

In addition to the band structure, we carried out the DFT calculations of the partial densities of states (PDOS) of As and Se atoms in the molecule and the crystal, which are shown in Figs. 6 and 7. In both figures there are two distinct regions in the valence band. The lowest valence band between –15 eV and –8 eV is composed by the s^2 lone pair electron states of As and Se atoms (see also Figs. 3 and 4 for CDD). The highest valence band for the As_4Se_4 crystal lies between –5.5 eV and 0.0 eV (E_F) and exhibits three distinct peaks from p-states of both types of atoms. These three peaks presented in PDOS graphics both of the molecule and the crystal originate from the p_x, p_y and p_z states of As atom and p_x, p_y and p_z^2 states of Se atom. The p_z^2 lone pair of Se atom is clearly visible on the CDD visualization graphs of both the molecule and the crystal (see Figs. 3 and 4). The lone pair nature of p-states near VBM is consistent with widely accepted concepts about electronic structure of chalcogenide materials.

It is worth noting that PDOS structure of the As_4Se_4 crystal calculated in this study is very similar to DOS structure of glassy As_4Se_4 (g-As_4Se_4), calculated in the cluster approach by DFT method (Li, Drabold, Krishnaswami et al. 2002). Although the interpretations of the origin of PDOS three peaks in the

upper valence band of the crystalline and glassy As_4Se_4 differ significantly. So, in the article (Li, Drabold, Krishnaswami et al. 2002) devoted to the g-As_4Se_4, these three peaks are attributed to interactions between various structural elements of the g-As_4Se_4. However, such interpretation seems artificial since the As_4Se_4 crystal does not contain highlighted elements characteristic for g-As_4Se_4, while PDOS structures of the upper valence bands for crystalline and glassy As_4Se_4 consist of the same three peaks.

PDOS of As and Se atoms in the molecule and in the crystal are shown in Figs. 6 and 7. Similar to a crystal, in the case of a molecule, the lowest unoccupied molecular orbital (LUMO) states and the highest occupied molecular orbital (HOMO) states are composed mainly by p-states of As and Se atoms.

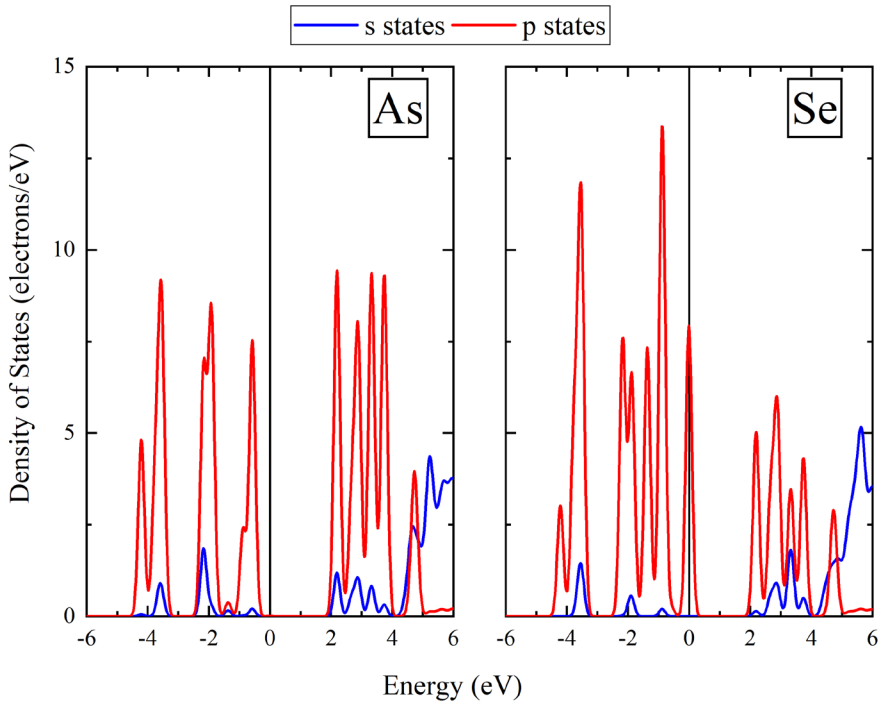

Fig. 6. PDOS for the As_4Se_4 molecule

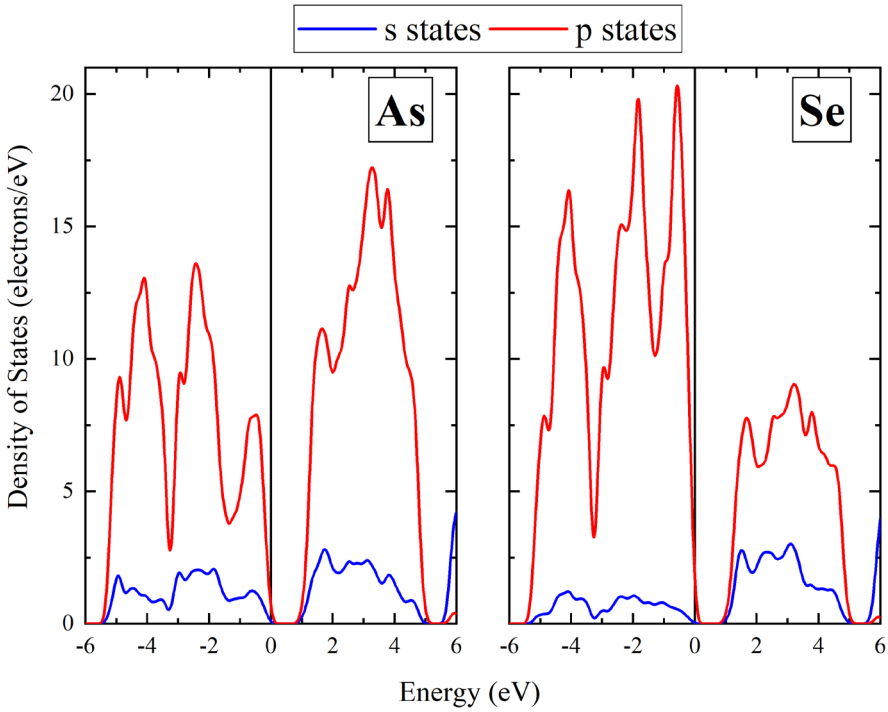

Fig. 7. PDOS for the As_4Se_4 crystal

https://www.doi.org/10.33910/2687-153X-2024-5-2-91-103

Conclusions

First, we studied the geometric and electronic structure of the As_4Se_4 crystal versus the As_4Se_4 molecule in the framework of a periodic model by a plane wave DFT method within the same approximations. Equilibrium bond lengths and bond angles were calculated together with charge density differences, Mulliken, Löwdin and Bader charges, and also Mulliken overlap populations, and were compared for the crystal and the molecule. The features of chemical bonding in the As_4Se_4 crystal versus the As_4Se_4 molecule were analyzed. The Bader charges of As and Se atoms turned out to be relatively small both in the molecule and in the crystal, which emphasizes only a moderate ionic contribution to the covalent bond (the so-called polar covalency). A comparative analysis of the overlap populations in the As_4Se_4 molecule and crystal demonstrated the antibonding character of effective interaction between the nearest intramolecular As atoms in the As_4Se_4 crystal and its absence in the molecule. The band structure DFT calculations were carried out and showed that the As_4Se_4 crystal is an indirect-gap semiconductor.

Conflict of Interest

The authors declare that there is no conflict of interest, either existing or potential.

Author Contributions

Conceptualization and methodology — V. G. Kuznetsov; formal analysis, investigation and data curation — V. G. Kuznetsov and A. A. Gavrikov; writing the original draft — A. A. Gavrikov and V. G. Kuznetsov; visualization — A. A. Gavrikov and V. G. Kuznetsov; supervision — V. G. Kuznetsov; discussion of current results and editing — A. A. Gavrikov, V. G. Kuznetsov and V. A. Trepakov.

Acknowledgements

V. G. Kuznetsov and A. A. Gavrikov are grateful to A. V. Kolobov and I. I. Tupitsyn for helpful discussions. Computational resources were provided by the supercomputer facility at Ioffe Institute.

References

Anderson, P. W. (1969) Localized orbitals for Molecular Quantum Theory. I. The Hückel Theory. *Physical Review*, 181 (1), 25–32. https://doi.org/10.1103/PhysRev.181.25 (In English)

Babić, D., Rabii, S. (1988) Self-consistent-field Xα scattered-wave calculation of the electronic structure of arsenic chalcogenide molecules. *Physical Review B*, 38 (15), 10490–10498. https://doi.org/10.1103/PhysRevB.38.10490 (In English)

Babić, D., Rabii, S., Bernholc, J. (1989) Structural and electronic properties of arsenic chalcogenide molecules. *Physical Review B*, 39 (15), 10831–10838. https://doi.org/10.1103/PhysRevB.39.10831 (In English)

Bader, R. F. W. (1990) *Atoms in molecules: A Quantum Theory*. Oxford: Oxford University Press, 438 p. (In English)

Bader, R. F. W., Anderson, S. G., Duke, A. J. (1979) Quantum topology of molecular charge distributions. 1. *Journal of the American Chemical Society*, 101 (6), 1389–1395. https://doi.org/10.1021/ja00500a006 (In English)

Bastow, T. J., Whitfield, H. J. (1973) Crystal structure of tetra-arsenic tetraselenide. *Journal of the Chemical Society, Dalton Transactions*, 17, 1739–1740. https://doi.org/10.1039/DT9730001739 (In English)

Beran, G. J. O. (2016) Modeling polymorphic molecular crystals with Electronic Structure Theory. *Chemical Reviews*, 116 (9), 5567–5613. https://doi.org/10.1021/acs.chemrev.5b00648 (In English)

Blöchl, P. E. (1994) Projector augmented-wave method. *Physical Review B*, 50 (24), 17953–17979. https://doi.org/10.1103/PhysRevB.50.17953 (In English)

Bullett, D. W. (1975) Electronic structures of layer and chain elements by a local orbital method. *The Philosophical Magazine: A Journal of Theoretical Experimental and Applied Physics. Series 8*, 32 (5), 1063–1074. https://doi.org/10.1080/14786437508221674 (In English)

Bullett, D. W. (1976a) Electronic structure of arsenic chalcogenides. *Physical Review B*, 14 (4), 1683–1692. https://doi.org/10.1103/PhysRevB.14.1683 (In English)

Bullett, D. W. (1976b) Density of states calculation for crystalline As and Sb. *Solid State Communications*, 17 (8), 965–967. https://doi.org/10.1016/0038-1098(75)90230-6 (In English)

Chen, I. (1975) Electronic structures of As_4Se_4 and Se_8. *Physical Review B*, 11 (10), 3976–3982. https://doi.org/10.1103/PhysRevB.11.3976 (In English)

Cherin, P., Unger, P. (1967) The crystal structure of trigonal selenium. *Inorganic Chemistry*, 6 (8), 1589–1591. https://doi.org/10.1021/ic50054a037 (In English)

Cherin, P., Unger, P. (1972) Refinement of the crystal structure of α-monoclinic Se. *Acta Cristallographica*, B28, 313–317. https://doi.org/10.1107/S0567740872002249 (In English)

Clark, S. J., Segall, M. D., Pickard, C. J. et al. (2005) First principles methods using CASTEP. *Zeitschrift für Kristallographie — Crystalline Materials*, 220 (5–6), 567–570. https://doi.org/10.1524/zkri.220.5.567.65075 (In English)

Dal Corso, A. (2014) Pseudopotentials periodic table: From H to Pu. *Computational Materials Science*, 95, 337–350. https://doi.org/10.1016/j.commatsci.2014.07.043 (In English)

Giannozzi, P., Andreussi, O., Brumme, T. et al. (2017) Advanced capabilities for materials modelling with Quantum ESPRESSO. *Journal of Physics: Condensed Matter*, 29 (46), article 465901. https://doi.org/10.1088/1361-648X/aa8f79 (In English)

Giannozzi, P., Baroni, S., Bonini, N. et al. (2009) QUANTUM ESPRESSO: A modular and open-source software project for quantum simulations of materials. *Journal of Physics: Condensed Matter*, 21 (39), article 395502. https://doi.org/10.1088/0953-8984/21/39/395502 (In English)

Goldstein, P., Paton, A. (1974) The crystal and molecular structure of tetrameric arsenic selenide, As_4Se_4. *Acta Cristallographica*, B30, 915–920. https://doi.org/10.1107/S0567740874004043 (In English)

Grimme, S. (2006) Semiempirical GGA-type density functional constructed with a long-range dispersion correction. *Journal of Computational Chemistry*, 27 (15), 1787–1799. https://doi.org/10.1002/jcc.20495 (In English)

Elliott, S. R. (1986) A unified model for reversible photostructural effects in chalcogenide glasses. *Journal of Non-Crystalline Solids*, 81 (1–2), 71–98. https://doi.org/10.1016/0022-3093(86)90260-7 (In English)

Elliott, S. R. (1990) *Physics of Amorphous Materials*. London; New York: Longman Publ., 387 p. (In English)

Eyert, V. (1996) Comparative study on methods for convergence acceleration of iterative vector sequences. *Journal of Computational Physics*, 124 (2), 271–285. https://doi.org/10.1006/jcph.1996.0059 (In English)

Hamann, D. R. (2013) Optimized norm-conserving Vanderbilt pseudopotentials. *Physical Review B*, 88 (8), article 085117. https://doi.org/10.1103/PhysRevB.88.085117 (In English)

Hasan, S. (2021) *First-principles study of the electronic structure, bonding, optical, mechanical, and thermoelectric properties of bulk chalcogenide crystals. PhD dissertation (Physics and Mathematics)*. Kansas, University of Missouri-Kansas City, 213 p. (In English)

Hasan, S., Baral, K., Ching, W.-Y. (2019) *Total bond order density as a quantum mechanical metric for materials design: Application to chalcogenide crystals. Preprints*, article 2019060199. [Online]. Available at: https://www.preprints.org/manuscript/201906.0199/v1 (accessed 20.03.2024). (In English)

Henkelman, G., Arnaldsson, A., Jónsson, H. (2006) A fast and robust algorithm for Bader decomposition of charge density. *Computational Materials Science*, 36 (3), 354–360. https://doi.org/10.1016/j.commatsci.2005.04.010 (In English).

Kolobov, A. V. (2003) *Photo-induced metastability in amorphous semiconductors*. Hoboken: Wiley Publ., 412 p. http://dx.doi.org/10.1002/9783527602544 (In English)

Kolobov, A. V., Elliott, S. R. (1995) Reversible photo-amorphization of crystalline films of $As_{50}Se_{50}$. *Journal of Non-Crystalline Solids*, 189 (3), 297–300. https://doi.org/10.1016/0022-3093(95)00245-6 (In English)

Krecmer, P., Moulin, A. M., Stephenson, R. J. et al. (1997) Reversible nanocontraction and dilatation in a solid induced by polarized light. *Science*, 277 (5333), 1799–1802. https://doi.org//10.1126/science.277.5333.1799 (In English)

Kresse, G., Joubert, D. (1999) From ultrasoft pseudopotentials to the projector augmented-wave method. *Physical Review B*, 59 (3), 1758–1775. https://doi.org/10.1103/PhysRevB.59.1758 (In English)

Li, J., Drabold, D. A., Krishnaswami, S. et al. (2002) Electronic Structure of Glassy Chalcogenides As_4Se_4 and As_2Se_3: A Joint Theoretical and Experimental Study. *Physical Review B*, 88 (4), article 046803 https://doi.org/10.1103/PhysRevLett.88.046803 (In English)

Löwdin, P.-O. (1950) On the non-orthogonality problem connected with the use of atomic wave functions in the theory of molecules and crystals. *The Journal of Chemical Physics*, 18 (3), 365–375. https://doi.org/10.1063/1.1747632 (In English)

Monkhorst, H. J., Pack, J. D. (1976) Special points for Brillouin-zone integrations. *Physical Review B*, 13 (12), 5188–5192. https://doi.org/10.1103/PhysRevB.13.5188 (In English)

Mulliken, R. S. (1955) Electronic Population Analysis on LCAO-MO molecular wave functions. I. *The Journal of Chemical Physics*, 23 (10), 1833–1840. https://doi.org/10.1063%2F1.1740588 (In English)

Owen, A. E., Firth, A. P., Ewen, P. J. S. (1985) Photo-induced structural and physico-chemical changes in amorphous chalcogenide semiconductors. *Philosophical Magazine Part B*, 52 (3), 347–362. https://doi.org/10.1080/13642818508240606 (In English)

Perdew, J. P., Burke, K., Ernzerhof, M. (1996) Generalized gradient approximation made simple. *Physical Review Letters*, 77 (18), 3865–3868. https://doi.org/10.1103/PhysRevLett.77.3865 (In English)

Perdew, J. P., Ruzsinszky, A., Csonka, G. I. et al. (2008) Restoring the density-gradient expansion for exchange in solids and surfaces. *Physical Review Letters*, 100 (13), article 136406. https://doi.org/10.1103/PhysRevLett.100.136406 (In English)

Perdew, J. P., Zunger, A. (1981) Self-interaction correction to density-functional approximations for many-electron systems. *Physical Review B*, 23 (10), 5048–5079. https://doi.org/10.1103/PhysRevB.23.5048 (In English).

Pfrommer, B. G., Côté, M., Louie, S. G., Cohen, M. L. (1997) Relaxation of crystals with the quasi-Newton method. *Journal of Computational Physics*, 131 (1), 233–240. https://doi.org/10.1006/jcph.1996.5612 (In English)

Press, W. H., Flannery, B. P., Teukolsky, S. A., Vetterling, W. T. (1992) *Numerical recipes in C: The art of scientific computing*. 2nd ed. Cambridge: Cambridge University Press, 994 p. (In English)

Renninger, A. L., Averbach, B. L. (1973) Atomic radial distribution functions of As-Se glasses. *Physical Review B*, 8 (4), 1507–1514. https://doi.org/10.1103/PhysRevB.8.1507 (In English)

Salaneck, W. R., Liang, K. S., Paton, A., Lipari, N. O. (1975) Electronic structure of molecular arsenic chalcogenides. *Physical Review B*, 12 (2), 725–730 https://doi.org/10.1103/PhysRevB.12.725 (In English)

Sanchez-Portal, D., Artacho, E., Soler, J. M. (1995) Projection of plane-wave calculations into atomic orbitals. *Solid State Communications*, 95 (10), 685–690. https://doi.org/10.1016/0038-1098%2895%2900341-X (In English)

Sanville, E., Kenny, S. D., Smith, R., Henkelman, G. (2007) An improved grid-based algorithm for Bader charge allocation. *Journal of Computational Chemistry*, 28 (5), 899–908. https://doi.org/10.1002/jcc.20575 (In English)

Schlipf, M., Gygi, F. (2015) Optimization algorithm for the generation of ONCV pseudopotentials. *Computer Physics Communications*, 196, 36–44. https://doi.org/10.1016/j.cpc.2015.05.011 (In English)

Schomaker, V., Stevenson, D. P. (1941) Some revisions of the covalent radii and the additivity rule for the lengths of partially ionic single covalent bonds. *Journal of American Chemical Society*, 63 (1), 37–40. https://doi.org/10.1021/ja01846a007 (In English)

Segall, M. D., Lindan, P. J. D., Probert, M. J. et al. (2002) First-principles simulation: Ideas, illustrations and the CASTEP code. *Journal of Physics: Condensed Matter*, 14 (11), 2717–2744. https://doi.org/10.1088/0953-8984/14/11/301 (In English)

Segall, M. D., Pickard, C. J., Shah, R., Payne, M. C. (2010) Population analysis in plane wave electronic structure calculations. *Molecular Physics: An International Journal at the Interface Between Chemistry and Physics*, 89 (2), 571–577. http://dx.doi.org/10.1080/002689796173912 (In English)

Segall, M. D., Shah, R., Pickard, C. J., Payne, M. C. (1996) Population analysis of plane-wave electronic structure calculations of bulk materials. *Physical Review B*, 54 (23), 16317–16320. https://doi.org/10.1103/PhysRevB.54.16317 (In English)

Shanno, D. F. (1978) Conjugate gradient methods with inexact searches. *Mathematics of Operations Research*, 3 (3), 244–256. https://doi.org/10.1287/moor.3.3.244 (In English)

Shimakawa, K., Yoshida, N., Ganjoo, A. et al. (1998) A model for the photostructural changes in amorphous chalcogenides. *Philosophical Magazine Letters*, 77 (3), 153–158. http://dx.doi.org/10.1080/095008398178598 (In English)

Smail, E. J., Sheldrick, G. M. (1974) Tetra-arsenic Tetraselenide. *Acta Cristallographica*, B29, 2014–2016. https://doi.org/10.1107/S0567740873005972 (In English)

Tanaka, K. (2001) Chalcogenide Glasses. In: *Encyclopedia of Materials: Science and Technology*. 2nd ed. Oxford: Elsevier Publ., pp. 1123–1131. https://doi.org/10.1016/B0-08-043152-6/00210-2 (In English)

Tanaka, K., Yamabe, T., Tachibana, A. et al. (1978) Electronic structures of tetrasulfur tetranitride, tetraarsenic tetrasulfide, and tetraarsenic tetraselenide, and their anionic species. *Journal of Physical Chemistry*, 82 (19), 2121–2126. https://doi.org/10.1021/j100508a013 (In English)

Tang, W., Sanville, E., Henkelman, G. (2009) A grid-based Bader analysis algorithm without lattice bias. *Journal of Physics: Condensed Matter*, 21 (8), article 084204. http://dx.doi.org/10.1088/0953-8984/21/8/084204 (In English)

Van Setten, M. J., Giantomassi, M., Bousquet, E. et al. (2018) The PseudoDojo: Training and grading a 85 element optimized norm-conserving pseudopotential table. *Computer Physics Communications*, 226, 39–54. https://doi.org/10.1016/j.cpc.2018.01.012 (In English)

Yang, C. Y., Paesler, M. A., Sayers, D. E. (1987) Measurement of local structural configurations associated with reversible photostructural changes in arsenic trisulfide films. *Physical Review B*, 36 (17), 9160–9167. https://doi.org/10.1103/PhysRevB.36.9160 (In English)

Book review. Theory of condensed matter

UDC 538.9

EDN XZMPIQ
https://www.doi.org/10.33910/2687-153X-2024-5-2-104-105

Book review on *Physics of Complex Systems: Discovery in the Age of Gödel* by Dragutin T. Mihailović, Darko Kapor, Siniša Crvenković and Anja Mihailović (Boca Raton; London; New York: CRC Press; Taylor & Francis Group Publ., 2023)

Z. M. Ivić ✉[1]

[1] Vinča Institute of Nuclear Sciences, University of Belgrade, National Institute of the Republic of Serbia, 12–14 Mike Petrovića Alasa Str., 11351 Vinča, Belgrade, Republic of Serbia

Author

Zoran M. Ivić, ORCID: 0000-0003-4031-6870, e-mail: zivic@vinca.rs

For citation: Ivić, Z. M. (2024) Book review on *Physics of Complex Systems: Discovery in the Age of Gödel* by Dragutin T. Mihailović, Darko Kapor, Siniša Crvenković and Anja Mihailović (Boca Raton; London; New York: CRC Press; Taylor & Francis Group Publ., 2023). *Physics of Complex Systems*, 5 (2), 104–105. https://www.doi.org/10.33910/2687-153X-2024-5-2-104-105 EDN XZMPIQ

Received 3 March 2024; reviewed 26 March 2024; accepted 26 March 2024.

Funding: The study did not receive any external funding.

This book is the result of the joint efforts of four Serbian scientists — recognized experts in theoretical physics, meteorology, and applied and pure mathematics. During the years of research, they were deeply involved in the study of complex systems in diverse contexts. The inspiration for the book was found in the problems that the authors encountered in teaching and research.

The main subject of the book is the physics of complex systems, which earned the status of a scientific field in its own right about thirty years ago. Since then, it has become a unifying approach to the study of phenomena in complex systems encountered in the frontier fields of physics, chemistry, technology, biology, ecology, and social sciences. Complex systems consist of many interacting components, e. g. building blocks including atoms, molecules, neurons, animals, or persons, which can exhibit emergent behavior that is not dictated exclusively by the classical laws of nature (physics, chemistry, biology). In complexity science, the focus is on understanding the emergent behavior of the system as a whole. A single neuron is not enough to explain consciousness, and the behavior of a single ant does not say much about the incredibly sophisticated organization of ant colonies. What makes consciousness and societies emerge are the interactions between the components, which are more than a collection of independent objects. The nature of these interactions can be physical, e. g. the interaction potential in a system of particles, or be defined by a set of rules that the components follow.

In this book, the authors insist that the understanding of phenomena in the real world surrounding us, consisting of complex systems characterized by nonlinear interactions, requires reasoning opposite to the usual approach stemming from reductionism. Based on the authors' research on these topics, this book puts forward the idea that the applications of information measures can provide new results in the study of complex systems. The authors particularly elaborate on this idea in the first five chapters out of ten, where they consider the philosophical and epistemological issues on which this idea relies. Thus, starting with the discussion on the generality of physics from the perspective to which extent it may

explain phenomena in complex systems, through the discussion of the philosophical and physical understanding of time, building of theories and models, authors gradually lead the reader toward the concept of information and information measures, and their applications in complex systems.

The usefulness of such an approach in the studies of real-world phenomena is illustrated in the last five chapters, where a collection of the authors' original contributions to the physics of complex systems in diverse scientific areas has been presented. Examples include the application of Kolmogorov and Aksentijevic–Gibson complexity in a search for patterns in the analysis of Bell's experiments, the identification of gravitational waves (LIGO experiment), and environmental fluid flows; separation of scales in complex systems as a reflection of Gödel's incompleteness theorems; and discussion of randomness in turbulent flows and its quantification via complexity by considering information measures suitable for its description. A particularly interesting example is the discussion of the role of the physics of complex systems in explaining an impression about a picture through the perception analyzed with change complexity and the recognition of order and disorder with entropy. Finally, the applications of the physics of complex systems to medical sciences are illustrated through models and approaches dealing with intercellular communication, autoimmune diseases, and brain disorders.

This is one of the most original texts on complex systems. The authors were inspired to write it by the work of Kurt Gödel, 'whose daring approach through reasoning opposite to accumulated experience and mainstream inspired many researchers to make breakthroughs.' As the authors emphasize, this book is not a textbook. It may not help by directing how to deal with specific problems. Nevertheless, it may be a reason why to study them.

About the authors

Dragutin T. Mihailović is a retired Professor in Meteorology, Environmental Fluid Mechanics, and Biophysics at the University of Novi Sad, Serbia. He has achieved outstanding results in subjects related to land–atmosphere processes, air pollution, chemical transport modeling, boundary layer meteorology, physics and modeling of phenomena on environmental interfaces, modeling of complex systems, nonlinear dynamics, and complexity.

Darko Kapor is a retired Professor of Theoretical and Mathematical Physics at the University of Novi Sad, Serbia. His main research interest is theoretical condensed matter physics, and he was the head of several research projects. Later, he developed an interest in theoretical meteorology and environmental surfaces.

Siniša Crvenković is a retired Professor of Mathematics at the University of Novi Sad, Serbia. His main research interests are algebra, mathematical logic, constructive mathematics, history, and philosophy of mathematics.

Anja Mihailović was the External Associate of the Center for Meteorology and Environmental Modelling at the University of Novi Sad, Serbia. Her scientific research is primarily focused on applied mathematics, including complexity, information measures, and their applications.

Conflict of Interest

The author declares that there is no conflict of interest, either existing or potential.

Summaries in Russian / Информация о статьях на русском языке

Физика конденсированного состояния

МОЛЕКУЛЯРНАЯ СТРУКТУРА И ДИНАМИКА ВОДНО-ЭТАНОЛЬНОГО РАСТВОРА ДОДЕЦИЛСУЛЬФАТА НАТРИЯ

Иван Владимирович Лунев, Артур Альбертович Галиуллин, Юрий Фёдорович Зуев

Аннотация. Изучены процессы диэлектрической релаксации растворов додецилсульфата натрия (ДСН) в диапазоне концентраций в бинарном водно-этанольном растворителе при различных концентрациях спирта. Показано, что этанол в концентрациях ниже 40% не препятствует мицеллообразованию ДСН, а при более высоком содержании этанола мицеллы ПАВ не образуются. Тем не менее данные ЯМР показывают наличие в растворах с высокой концентрацией спирта малых ассоциатов, скорее всего димеров ДСН, свойства и подвижность которых зависят от состава водно-этанольной среды. Обсуждены трансформации структуры и размеров комплексов при изменении содержания этанола в растворе.

Ключевые слова: бинарные растворы вода–этанол, поверхностно-активное вещество, ДСН, структурообразование, сольватация, мицеллы

Для цитирования: Lunev, I. V., Galiullin, A. A., Zuev, Yu. F. (2024) Molecular structure and dynamics of a water–ethanol solution of sodium dodecyl sulfate. *Physics of Complex Systems*, 5 (2), 49–59. https://www.doi.org/10.33910/2687-153X-2024-5-2-49-59 EDN AEKJUI

ПЬЕЗОЭЛЕКТРИЧЕСКИЕ СВОЙСТВА СФЕРОЛИТОВЫХ ТОНКИХ ПЛЕНОК ЦИРКОНАТА-ТИТАНАТА СВИНЦА

Станислав Викторович Сенкевич, Дмитрий Александрович Киселев, Михаил Владимирович Старицын, Евгений Юрьевич Каптелов, Игорь Петрович Пронин

Аннотация. Методом силовой микроскопии пьезоэлектрического отклика исследованы тонкие пленки цирконата-титаната свинца, отличающиеся сферолитовой радиально-лучистой микростуктурой, состав которых соответствует области морфотропной фазовой границы. Выявлены особенности вертикального и латерального пьезооткликов, а также потенциала поверхности (Кельвин-мода). Проводится сравнение свойств пьезоэлектрического отклика тонких пленок с особенностями радиально-лучистой микроструктуры и механических напряжений, образующихся в пленках в результате кристаллизации фазы перовскита из аморфной фазы.

Ключевые слова: силовая микроскопия пьезоэлектрического отклика, тонкие пленки цирконата-титаната свинца, радиально-лучистая сферолитовая микроструктура, механические напряжения, потенциал поверхности

Для цитирования: Senkevich, S. V., Kiselev, D. A., Staritsyn, M. V., Kaptelov, E. Yu., Pronin, I. P. (2024) Piezoelectric properties of spherulite thin films of lead zirconate titanate. *Physics of Complex Systems*, 5 (2), 60–66. https://www.doi.org/10.33910/2687-153X-2024-5-2-60-66 EDN GHTKLC

ПРИРОДА ЗАВИСИМОСТИ СКОРОСТИ РОСТА БАКТЕРИЙ ОТ ТЕМПЕРАТУРЫ: АНАЛОГИЯ С ВЯЗКОСТЬЮ СТЕКЛООБРАЗУЮЩИХ ЖИДКОСТЕЙ В НЕОРГАНИЧЕСКИХ МАТЕРИАЛАХ

Карлито Пинто, Коити Симакава

Аннотация. Исходя из недавнего предположения о том, что цитоплазма бактерий схожа по свойству со стеклообразующими жидкостями, нами предложено новое отношение зависимости скорости роста бактерий от температуры: $k = k_0 \exp[-E_a/k_B(T-T_c)]$ для диапазона низких температур, где k_0 — постоянная, E_a — энергия активации (eV), k_B — постоянная Больцмана, T — абсолютная температура (K), а T_c — характеристическая температура (замерзания) (K), по аналогии с зависящей от температуры текучестью (обратная вязкости величина), наблюдаемой в стеклообразующих жидкостях неорганических материалов. Данное монотонное поведение бактериального роста прерывается при более высоких температурах, т. е. k резко снижается вместе с T, что может быть связано с резким ростом физиологической концентрации цитоплаз-

мы при превышении критической температуры T_m. Наблюдение касательно температурной зависимости скорости бактериального роста аналогично наблюдению в отношении стеклообразующих жидкостей в неживых неорганических материалах.

Ключевые слова: скорость бактериального роста, стеклообразующая жидкость, переход в стеклообразное состояние, вязкость, свободный объем

Для цитирования: Pinto, C., Shimakawa, K. (2024) Origin of temperature dependence of bacterial growth rate: Analogy with the viscosity of glass-forming liquids in inorganic materials. *Physics of Complex Systems*, 5 (2), 67–73. https://www.doi.org/10.33910/2687-153X-2024-5-2-67-73 EDN POCJRY

Теоретическая физика

ТОКИ ВЕРОЯТНОСТИ В ИССЛЕДОВАНИЯХ НЕУПРУГИХ АТОМНЫХ СТОЛКНОВЕНИЙ

Илья Григорьевич Степанов, Андрей Константинович Беляев

Аннотация. Строгий метод токов вероятностей в рамках квантовой теории столкновений протестирован на примере моделей Талли для однократного прохождения областей неадиабатичности во время атомных столкновений. Расчеты проведены в диабатическом представлении путем численного интегрирования системы связанных уравнений для ядерных радиальных волновых функций. Результаты точных квантовых расчетов сравниваются с оценками модели Ландау–Зинера для тех же электронных структур. Показано, что метод токов вероятностей является эффективным средством исследования неупругих процессов в атомных столкновениях.

Ключевые слова: атомные столкновения, ток вероятности, модели Талли, вероятность неадиабатических переходов, модель Ландау–Зинера, диабатический базис

Для цитирования: Stepanov, I. G., Belyaev, A. K. (2024) Probability currents in inelastic atomic collision studies. *Physics of Complex Systems*, 5 (2), 74–82. https://www.doi.org/10.33910/2687-153X-2024-5-2-74-82 EDN IWQVHR

ВЛИЯЕТ ЛИ ПЕРВИЧНЫЙ ВОЛОС НА ФОРМИРОВАНИЕ ГОЛОЙ СИНГУЛЯРНОСТИ В МЕТРИКЕ ВАЙДЬЯ?

Виталий Дмитриевич Вертоградов

Аннотация. В статье рассматривается гравитационный коллапс в метрике Вайдья, полученной с помощью гравитационного расщепления. Мы исследуем вопрос о том, влияет ли первичный волос на конечный результат гравитационного коллапса. Мы доказали, что константа связи оказывает влияние на формирование голой сингулярности. Мы также исследовали вопрос о силе центральной сингулярности и доказали, что она является гравитационно-сильной. Тем не менее приведенная модель не нарушает космический принцип цензуры, поскольку при формировании голой сингулярности нарушаются слабые энергетические условия.

Ключевые слова: черная дыра, голая сингулярность, гравитационный коллапс, гравитационное расщепление, сила сингулярности

Для цитирования: Vertogradov, V. D. (2024) Does a primary hair have an impact on the naked singularity formation in hairy Vaidya spacetime? *Physics of Complex Systems*, 5 (2), 83–90. https://www.doi.org/10.33910/2687-153X-2024-5-2-83-90 EDN HFGXJA

Физика полупроводников

КРИСТАЛЛ As_4Se_4 В СРАВНЕНИИ С МОЛЕКУЛОЙ As_4Se_4: ИССЛЕДОВАНИЕ ГЕОМЕТРИИ И ЭЛЕКТРОННОЙ СТРУКТУРЫ С ПОМОЩЬЮ ПЛОСКОВОЛНОВОГО МЕТОДА DFT

Антон Андреевич Гавриков, Владимир Георгиевич Кузнецов, Владимир Андреевич Трепаков

Аннотация. Молекулярные кристаллы халькогенидов обнаруживают широкий спектр изменений химических и физических свойств под действием света с энергией, превышающей ширину запрещенной зоны. Большинство этих свойств определяются электронной структурой. Однако по электронной структуре As_4Se_4 имеется лишь несколько теоретических статей по молекуле и всего только две — по кристаллу As_4Se_4. В настоящей работе впервые были сопоставлены геометрическая и электронная структура кристалла As_4Se_4 и молекулы As_4Se_4, рассчитанные в рамках периодической модели методом DFT в одних и тех же приближениях. При этом были рассчитаны

равновесные длины связей и валентные углы вместе с разностными электронными плотностями, зарядами Малликена, Лёвдина и Бадера, а также Малликеновскими заселенностями перекрывания, и проведён сравнительный анализ характера химической связи в кристалле As_4Se_4 и молекуле As_4Se_4. Выполненные DFT расчеты зонной структуры показали, что кристалл As_4Se_4 является непрямозонным полупроводником.

Ключевые слова: халькогениды, геометрическая и электронная структура, химическая связь, As_4Se_4, молекула, молекулярный кристалл, метод функционала плотности

Для цитирования: Gavrikov, A. A., Kuznetsov, V. G., Trepakov, V. A. (2024) As_4Se_4 crystal versus As_4Se_4 molecule: A plane wave DFT study of the geometric and electronic structure. *Physics of Complex Systems*, 5 (2), 91–103. https://www.doi.org/10.33910/2687-153X-2024-5-2-91-103 EDN VYWZTC

Рецензии

РЕЦЕНЗИЯ НА КНИГУ Д. Т. МИХАЙЛОВИЧА, Д. КАПОРА, С. ЦРВЕНКОВИЧ И А. МИХАЙЛОВИЧ «ФИЗИКА СЛОЖНЫХ СИСТЕМ: ОТКРЫТИЯ В ЭПОХУ ГЁДЕЛЯ» (БОКА-РАТОН; ЛОНДОН; НЬЮ-ЙОРК: CRC PRESS; TAYLOR & FRANCIS GROUP PUBL., 2023)

Зоран Ивич

Для цитирования: Ivić, Z. M. (2024) Book review on *Physics of Complex Systems: Discovery in the Age of Gödel* by Dragutin T. Mihailović, Darko Kapor, Siniša Crvenković and Anja Mihailović (Boca Raton; London; New York: CRC Press; Taylor & Francis Group Publ., 2023). *Physics of Complex Systems*, 5 (2), 104–105. https://www.doi.org/10.33910/2687-153X-2024-5-2-104-105 EDN XZMPIQ